Numerical Models for Obliquely Incident Waves in Surf and Swash Zones

by

Entin A. Karjadi

and

Nobuhisa Kobayashi

RESEARCH REPORT NO. CACR-97-03

April, 1997

Center for Applied Coastal Research
Ocean Engineering Laboratory
University of Delaware
Newark, DE 19716

ACKNOWLEDGMENTS

This study was sponsored by the U.S. Army Research Office, University Research Initiative under Contract No. DAAL03-92-G-0116, by the NOAA Office Sea Grant, Department of Commerce, under Grant No. NA85AA-D-SG033 (Project SG95 R/OE18), and by the National Science Foundation under Grant No. CTS-9407827.

TABLE OF CONTENTS

LIST OF FIGURES

LIST OF TABLES

ABSTRACT

Time-dependent numerical models are developed to predict the temporal and cross-shore variations of the free surface elevation and the cross-shore and alongshore fluid velocities in the swash and surf zones under obliquely incident waves. The assumption of shallow water with small incident angles and slow alongshore variations are made to reduce computational efforts considerably and to eliminate difficulties associated with lateral boundary conditions. These assumptions enable the models to compute the cross-shore fluid motion separately from the alongshore motion. The numerical models allow gradual alongshore variations of the bathymetry and the incident regular or irregular waves specified at the seaward boundary.

Two numerical models are developed in this study. The first model is a two-dimensional (2D) model that neglects the vertical variations of the cross-shore and alongshore velocities. As a result, this model neglects the dispersion due to the vertical variations of the horizontal velocities and predicts only the depth-averaged cross-shore and alongshore velocities. The second model is a quasi three-dimensional (3D) model that assumes a cubic profile for the horizontal velocities and includes the dispersion terms due to the vertical variations of the horizontal velocities. Two additional equations for cross-shore and alongshore momentum flux corrections are derived.

These numerical models are compared with available laboratory and field data for planar beaches. To assess the importance of the dispersion terms, both models are compared with the same data. Both models are shown to be capable

of predicting the cross-shore variations of wave height, setup and runup for regular waves and root-mean-square wave height for irregular waves. The dispersion effects on wave height and setup are shown to be minor. The models predict large cross-shore and alongshore velocities near the shoreline for irregular waves. The causes of these large velocities are examined but can not be ascertained for lack of velocity data near the shoreline. For regular waves, the 2D model with the bottom friction factor calibrated previously for swash oscillations predicts the magnitude of longshore current but cannot reproduce the longshore current profile. For irregular waves, the longshore current is predicted fairly well by both models. The 3D model improves the prediction of the longshore current profile for regular waves significantly. This implies that the dispersion effects on the longshore current are significant for regular waves but secondary for irregular waves. The 3D model is also shown to predict the vertical shape of the longshore current inside the surf zone but not outside the surf zone. The vertical variation of the longshore current for irregular waves is shown to be small.

The 3D model is also compared with field data for a barred beach. The model underpredicts the root-mean-square wave height in the bar trough region. The field measurements of longshore currents generally indicate a broad peak in the bar trough region. Under the assumption of alongshore uniformity, the model cannot explain these broad peaks. The small alongshore variation of wave setup induced by a small alongshore variation of obliquely incident irregular waves is shown to significantly modify the driving force and longshore current profile in the bar trough region where the cross-shore gradient of the alongshore radiation stress is small. As a result, the longshore current profile in the bar trough region is sensitive to the alongshore variability. On the other hand, for planar beaches, the longshore current profile is shown to be insensitive to the alongshore variation of obliquely incident waves. This may explain why existing longshore current models based on

the assumption of alongshore uniformity were regarded to be adequate before their comparisons with the barred beach data.

Chapter 1

INTRODUCTION

Obliquely incident waves breaking on a beach generate longshore current that in turn drives longshore sediment transport. Knowledge of longshore sediment transport is important for the design of shoreline erosion mitigation measures such as sand bypassing and beach nourishment. Longshore sediment transport mostly takes place within the region where the waves deform after breaking and the region where a thin sheet of water rushes up and down the beach, known as the surf zone and swash zone, respectively. Therefore, a quantitative understanding of surf and swash hydrodynamics on beaches under obliquely incident waves is required for modeling of sediment transport in these regions.

Field and laboratory measurements on the distribution of longshore sediment transport across the surf zone indicated that the distribution was generally bimodal with peaks in the swash and breaker zones (*e.g.*, Bodge and Dean 1987; Kamphuis 1991). Bodge and Dean (1987) observed that the relative significance of the peaks shifted from the breaker zone peak to the swash zone peak as the surf varied from spilling to collapsing conditions. They found that longshore sediment transport in the swash zone might account for at least 5% to over 60% of the total drift.

There are two different approaches to study the surf zone hydrodynamics, namely, time-averaged and time dependent models. Time-averaged models split the fluid motion into a 'wave' part and a 'current' part where it is assumed that the wave motion is already known. On the other hand, time-dependent models account

for wave propagation and there is no need to differentiate between the wave and current parts of the motion. This is significant when dealing with the complicated wave motion in the surf and swash zones, although this type of model requires more computational effort.

Since the introduction of the concept of radiation stresses by Longuet-Higgins and Stewart (1960), time-averaged models have been applied widely to predict the cross-shore variations of the wave height, setup, longshore current and sediment transport rate in the surf and swash zones along a straight shoreline (*e.g.*, Battjes 1988). These models are relatively simple and useful for practical applications except in the swash zone. Contrary to the field and laboratory data, the models based on the time-averaged momentum and energy equations predict that the longshore current and sediment transport rate approach zero at the mean water shoreline. These models also underpredict the wave height and setup in the swash zone (Cox *et al.* 1994). Furthermore, swash measurements on natural beaches (*e.g.*, Guza and Thornton 1982; Holman and Sallenger 1985) show the dominance of low-frequency wave motions unless incident wind waves collapse or surge on foreshore slopes.

The main aim of this study is to develop time-dependent models in an attempt to predict the time-dependent and time-averaged hydrodynamics in the surf and swash zones as mentioned above.

1.1 A Brief Overview of Related Works

To explain a large volume of sediment transport in the swash zone, Thornton and Abdelrahman (1991) proposed an analytical model by including a specified standing wave of low-frequency interacting with an obliquely incident wave of a wind-wave frequency. As a result of the interaction between incident and low-frequency waves, a non-vanishing longshore current and sediment transport rate were found at the shoreline. This model indicates the importance of low-frequency standing waves in the swash zone that need to be estimated or predicted separately. To predict the

interaction between incident and low frequency waves in a more realistic manner, a time-dependent numerical model will be required although it will require more computational effort.

Ryrie (1983) developed a time-dependent numerical model for longshore fluid motion generated by obliquely incident monochromatic waves with a small angle of incidence along a straight shoreline with a plane slope. The model is based on the two-dimensional shallow water equations. The cross-shore and alongshore motions are decoupled using a new time variable, referred to as pseudo-time, which is a function of the phase speed and incident angle of the incident waves at the break point. The numerical model was not compared with any data. Recently, Brocchini and Peregrine (1996) examined the integral flow properties of the swash zone using the model of Ryrie (1983) and the standing wave solution of Carrier and Greenspan (1958).

Kobayashi *et al.* (1987, 1989) and Kobayashi and Wurjanto (1992) developed and evaluated a time-dependent, one-dimensional numerical model for normally incident waves using laboratory and field data on wave runup on steep and gentle slopes. This numerical model was shown by Cox *et al.* (1994) to agree fairly well (within about 20% errors) with the free surface measurements in the swash and inner surf zones using ten wave gages, partially buried in the sand, in a large wave flume. Similar results were also observed from the measurements by Raubenheimer *et al.* (1995) using a vertical stack of five runup wires supported parallel to a gently sloping natural beach. Karjadi and Kobayashi (1994) and Kobayashi and Karjadi (1994a) modified this model to predict solitary wave breaking, runup and reflection. The existing one-dimensional model is expanded herein to predict the cross-shore and temporal variations of the free surface elevation, the alongshore and cross-shore fluid velocities in the swash and surf zones under obliquely incident waves. The expanded numerical model is formulated unlike that of Ryrie (1983) such that it is

applicable to beaches of arbitrary geometry under obliquely incident random waves.

To reduce computational efforts considerably and to eliminate difficulties associated with lateral boundary conditions for general two-dimensional computations, the assumptions of small incident angles and slow alongshore variations are made. These assumptions enable the model to compute the alongshore velocity separately after the free surface elevation and the cross-shore velocity are computed using the one-dimensional model along at least three lines normal to the shoreline. On the other hand, because of these assumptions, the numerical model expanded herein cannot be used to predict edge waves (*e.g.*, Bowen and Guza 1978; Huntley *et al.* 1981), which appear to play an important role in the generation of rhythmic beach morphology (*e.g.*, Holman and Bowen 1982). Furthermore, rip currents (*e.g.*, Dalrymple 1978) and shear waves (Bowen and Holman 1989; Oltman-Shay *et al.* 1989) are beyond the capabilities of the expanded numerical model.

1.2 Outline of Report

In Chapter 2, the governing equations employed in the expanded numerical model are derived from the three-dimensional continuity and Reynolds equations (*e.g.*, Rodi 1980) in a manner similar to the derivation of Kobayashi and Wurjanto (1992) of the approximate one-dimensional equations from the two-dimensional continuity and Reynolds equations.

The approximate three-dimensional equations under the assumptions of shallow water waves on a relatively gentle impermeable slope with small angles of incidence are derived from the three-dimensional continuity and Reynolds equations. The approximate three-dimensional equations are then integrated over the water depth to obtain the depth-integrated continuity and horizontal momentum equations. In this study, two numerical models are developed. The first model is based on the approximate two-dimensional equations that neglect the dispersion terms due to the vertical variations of the horizontal velocities. This model is simply referred

to as the 2D model. The second model, based on a cubic profile of the horizontal velocities, includes the dispersion terms due to the vertical variations of the horizontal velocities. For brevity, this quasi-3D model is referred to as the 3D model.

The numerical procedures to solve the governing equations with appropriate initial and boundary conditions are explained in Chapter 3. For the 2D model, the governing equations for the cross-shore wave motion for small angles of incidence, which are the same as those of the one-dimensional model, are solved using the Lax-Wendroff method in the same way as the one-dimensional model developed by Kobayashi *et al.* (1987, 1989). For the longshore motion in the 2D model and for both the cross-shore and alongshore motions in the 3D model, the MacCormack (MacCormack 1969) finite difference method is selected because of its simplicity and success in the computation of unsteady open channel flows with hydraulic jumps (Chaudhry 1993).

In Chapter 4, the 2D numerical model is compared with laboratory data of Visser (1991) and field experiment conducted by Thornton and Guza (1986) at Leadbetter beach in 1980. The comparisons indicate that the 2D model predicts the maximum setup and runup fairly well although the model does not predict the transition zone of constant wave set-down. Also for regular waves the model cannot predict the longshore current profile since the model does not include the dispersion due to the vertical variation of the horizontal velocities. For irregular waves, the model predicts the root-mean-square wave height and longshore current fairly well. This implies that the effects of the dispersion on the longshore current under irregular waves are negligible as already concluded by Thornton and Guza (1986). The model predicts large cross-shore and alongshore velocities near the shoreline and very low-frequency oscillations of the depth-averaged alongshore velocity. The causes of these results are also examined in this chapter. The summaries of these comparisons were published by Kobayashi and Karjadi (1994b, 1996).

In Chapter 5, the 3D model is compared with the same regular and irregular wave data as the 2D model to assess the importance of the added dispersion terms. These limited comparisons indicate that the significant improvement due to the addition of the momentum flux corrections associated with the vertical variations of the horizontal velocities is essentially limited to the cross-shore profile of the longshore current induced by regular breaking waves. The effects of the dispersion terms on wave height, setup and runup are shown to be secondary. The 3D model is also shown to predict the vertical shape of the longshore current inside the surf zone but not outside the surf zone. The summary of Chapter 5 will be published by Kobayashi, Karjadi and Johnson (1997).

Chapter 6 discusses the application of the 3D model to a barred beach. The model is compared with the DELILAH field data of Smith *et al.* (1993). The measurements of longshore current on the barred beach during the DELILAH experiment generally indicated a broad peak in the bar trough region. The 3D model cannot explain this data under the assumption of alongshore uniformity. Low-frequency components and alongshore variations of incident irregular waves are examined to explain the broad peak of the longshore current. The longshore current profile on the barred beach is then shown to be sensitive to the alongshore variability unlike the longshore current profile on the plane beaches examined in Chapters 4 and 5. The summary of Chapter 6 will be published by Karjadi and Kobayashi (1996).

The summary and conclusions of this study is given in Chapter 7.

Chapter 2

MATHEMATICAL FORMULATION

The equations that govern the obliquely incident wave motions on an impermeable slope are derived and discussed in this chapter. The approximate governing equations under the assumptions of shallow water waves with small angles of incidence are derived from the three-dimensional continuity and Reynolds equations (*e.g.*, Rodi 1980). This derivation is similar to that of the one-dimensional equations from the two-dimensional continuity and momentum equations proposed by Kobayashi and Wurjanto (1992).

The notations used in the following analysis are depicted in Figure 2.1. The angle of wave incidence is θ_c and will be assumed small. The other symbols shown in this figure will be explained in the subsequent derivation. The model is formulated in such a way that it will be applicable for beaches with arbitrary geometry under obliquely incident regular or random waves.

2.1 Approximate Three-Dimensional Equations

The three-dimensional continuity and Reynolds equations are (*e.g.*, Rodi 1980)

$$\frac{\partial u_j'}{\partial x_j'} = 0 \tag{2.1}$$

$$\frac{\partial u_i'}{\partial t'} + u_j' \frac{\partial u_i'}{\partial x_j'} = -\frac{1}{\rho} \frac{\partial p'}{\partial x_i'} - g\delta_{i3} + \frac{1}{\rho} \frac{\partial \tau_{ij}'}{\partial x_j'} \tag{2.2}$$

where the prime indicates the physical variables and the summation convention is used with respect to repeated indexes. The symbols involved in (2.1) and (2.2) are depicted in Figure 2.1 and explained in the following:

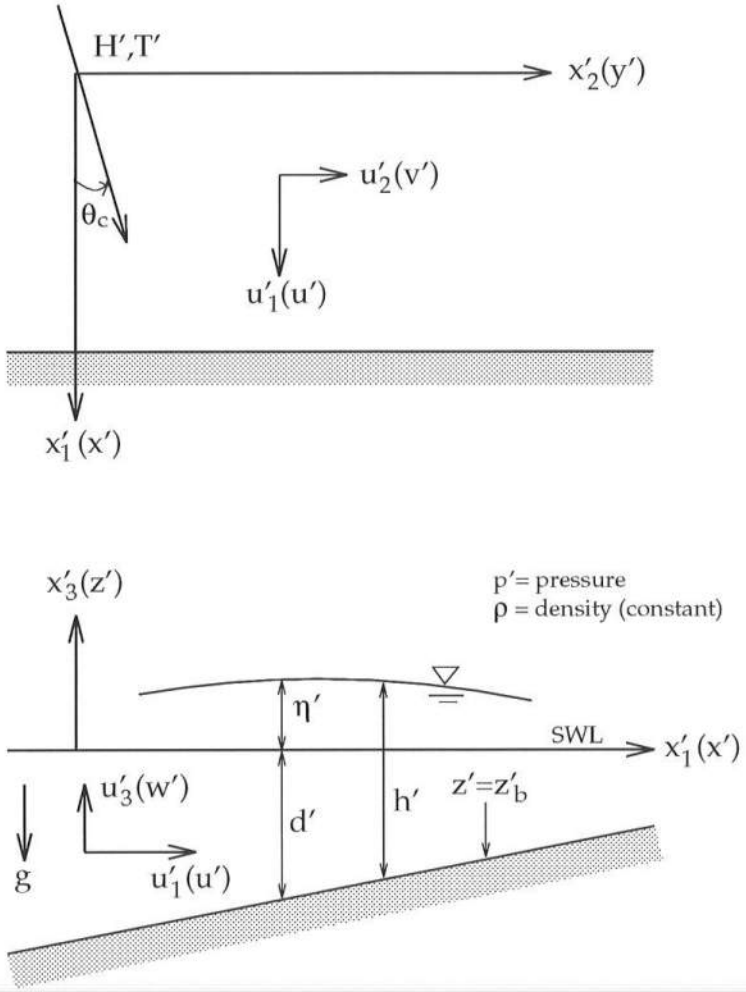

Figure 2.1: Definition sketch for obliquely incident wave motion on an impermeable slope.

t' = time

x_1' = horizontal coordinate normal to the overall shoreline orientation, taken to be positive landward

x_2' = horizontal coordinate normal to x_1'

x_3' = vertical coordinate taken to be positive upward with $x_3' = 0$ at the still water level (SWL)

u_1' = horizontal velocity in x_1' direction

u_2' = horizontal velocity in x_2' direction

u_3' = vertical velocity

ρ = fluid density, which is assumed constant

p' = pressure

g = gravitational acceleration

δ_{i3} = Kronecker delta

τ_{ij}' = sum of turbulent and viscous stresses

Assuming that the viscous stresses are negligible, τ_{ij}' may be expressed as (*e.g.*, Rodi 1980)

$$\tau_{ij}' = \rho \left[\nu_t' \left(\frac{\partial u_i'}{\partial x_j'} + \frac{\partial u_j'}{\partial x_i'} \right) - \frac{2}{3} k' \delta_{ij} \right] \tag{2.3}$$

where

ν_t' = turbulent eddy viscosity

k' = turbulent kinetic energy per unit mass

To simplify (2.1) and (2.2) together with (2.3) in shallow water, the dimensional variables may be normalized as

$$t = \frac{t'}{T'} \quad ; \quad x_1 = \frac{x_1'}{T'(gH')^{1/2}} \quad ; \quad x_2 = \frac{x_2'}{T'(gH')^{1/2}/\theta_c} \quad ; \quad x_3 = \frac{x_3'}{H'} \tag{2.4}$$

$$u_1 = \frac{u_1'}{(gH')^{1/2}} \quad ; \quad u_2 = \frac{u_2'}{\theta_c (gH')^{1/2}} \quad ; \quad u_3 = \frac{u_3'}{H'/T'} \quad ; \quad p = \frac{p'}{\rho g H'} \tag{2.5}$$

$$\nu_t = \frac{\nu_t'}{H'^2/T'} \quad ; \quad k = \frac{k'}{H'(gH')^{1/2}/T'} \quad ; \quad \sigma = \frac{T'(gH')^{1/2}}{H'} \tag{2.6}$$

where T', H' and θ_c are the characteristic wave period, height and incident angle in radian used for the normalization. The parameter σ defined in (2.6) is the ratio of the cross-shore length scale to the vertical length scale. The normalized variables in (2.4) and (2.5) are assumed to be on the order of unity in shallow water. The normalization of ν_t' and k' in (2.6) is based on the turbulence measurements in a wave flume by Cox *et al.* (1994), which have indicated that ν_t and k are on the order of unity or less inside and immediately outside the surf zone, respectively.

Substituting (2.4) and (2.5) into (2.1), the normalized continuity equation can be written as

$$\frac{\partial u_1}{\partial x_1} + (\theta_c)^2 \frac{\partial u_2}{\partial x_2} + \frac{\partial u_3}{\partial x_3} = 0 \tag{2.7}$$

Substituting (2.4), (2.5), and (2.6) into (2.2) and (2.3), the horizontal momentum equations are given by

$$\begin{aligned}\frac{\partial u_1}{\partial t} + u_1\frac{\partial u_1}{\partial x_1} + \theta_c^2 u_2\frac{\partial u_1}{\partial x_2} + u_3\frac{\partial u_1}{\partial x_3} = &-\frac{\partial p}{\partial x_1} + \frac{\partial}{\partial x_1}\left[\frac{1}{\sigma^2}\left(2\nu_t\frac{\partial u_1}{\partial x_1}\right) - \frac{2}{3}\frac{k}{\sigma}\right] \\ &+\frac{\theta_c^2}{\sigma^2}\frac{\partial}{\partial x_2}\left[\nu_t\left(\frac{\partial u_1}{\partial x_2} + \frac{\partial u_2}{\partial x_1}\right)\right] + \frac{\partial}{\partial x_3}\left[\nu_t\left(\frac{\partial u_1}{\partial x_3} + \frac{1}{\sigma^2}\frac{\partial u_3}{\partial x_1}\right)\right]\end{aligned} \tag{2.8}$$

and

$$\begin{aligned}\frac{\partial u_2}{\partial t} + u_1\frac{\partial u_2}{\partial x_1} + \theta_c^2 u_2\frac{\partial u_2}{\partial x_2} + u_3\frac{\partial u_2}{\partial x_3} = &-\frac{\partial p}{\partial x_2} + \frac{1}{\sigma^2}\frac{\partial}{\partial x_1}\left[\nu_t\left(\frac{\partial u_2}{\partial x_1} + \frac{\partial u_1}{\partial x_2}\right)\right] \\ &+\frac{\partial}{\partial x_2}\left[\frac{\theta_c^2}{\sigma^2}\left(2\nu_t\frac{\partial u_2}{\partial x_2}\right) - \frac{2}{3}\frac{k}{\sigma}\right] + \frac{\partial}{\partial x_3}\left[\nu_t\left(\frac{\partial u_2}{\partial x_3} + \frac{1}{\sigma^2}\frac{\partial u_3}{\partial x_2}\right)\right]\end{aligned} \tag{2.9}$$

whereas the vertical momentum equation is given by

$$\begin{aligned}\frac{1}{\sigma^2}\left(\frac{\partial u_3}{\partial t} + u_1\frac{\partial u_3}{\partial x_1} + \theta_c^2 u_2\frac{\partial u_3}{\partial x_2} + u_3\frac{\partial u_3}{\partial x_3}\right) = &-\frac{\partial}{\partial x_3}(p + x_3) \\ &+\frac{1}{\sigma^2}\frac{\partial}{\partial x_1}\left[\nu_t\left(\frac{1}{\sigma^2}\frac{\partial u_3}{\partial x_1} + \frac{\partial u_1}{\partial x_3}\right)\right] + \frac{\theta_c^2}{\sigma^2}\frac{\partial}{\partial x_2}\left[\nu_t\left(\frac{1}{\sigma^2}\frac{\partial u_3}{\partial x_2} + \frac{\partial u_2}{\partial x_3}\right)\right] \\ &+\frac{\partial}{\partial x_3}\left[\frac{1}{\sigma^2}\left(2\nu_t\frac{\partial u_3}{\partial x_3}\right) - \frac{2}{3}\frac{k}{\sigma}\right]\end{aligned} \tag{2.10}$$

Under the assumptions of $\sigma^2 \gg 1$ and $\theta_c^2 \ll 1$ for shallow water waves with small angles of incidence, the terms on the order of σ^{-2}, θ_c^2, and smaller in (2.7),

(2.8), (2.9), and (2.10) may be neglected. The normalized continuity equation (2.7) may thus be simplified as

$$\frac{\partial u_1}{\partial x_1} + \frac{\partial u_3}{\partial x_3} = 0 \tag{2.11}$$

The normalized horizontal momentum equations (2.8) and (2.9) with $i = 1$ and 2 may also be simplified as

$$\frac{\partial u_i}{\partial t} + u_1 \frac{\partial u_i}{\partial x_1} + u_3 \frac{\partial u_i}{\partial x_3} = -\frac{\partial}{\partial x_i}\left(p + \frac{2}{3}\,\frac{k}{\sigma}\right) + \frac{\partial \tau_i}{\partial x_3} \tag{2.12}$$

with

$$\tau_i = \nu_t \frac{\partial u_i}{\partial x_3} \tag{2.13}$$

and the normalized vertical momentum equation (2.10) is simplified as

$$0 = -\frac{\partial}{\partial x_3}\left(p + x_3 + \frac{2}{3}\,\frac{k}{\sigma}\right) \tag{2.14}$$

The symbols η' and d' in Figure 2.1 represent the free surface elevation above SWL and the water depth below SWL, respectively. Their normalized counterparts are given by

$$\eta = \frac{\eta'}{H'} \;\; ; \;\; d = \frac{d'}{H'} \tag{2.15}$$

where H' is the characteristic wave height used for the normalization.

To further simplify the governing equations, the approximate three-dimensional continuity and momentum equations derived above will be integrated over the water depth using the kinematic and dynamic boundary conditions at the free surface and bottom. The kinematic free surface and bottom boundary conditions require that the total derivative of any fixed or moving surface with respect to time is equal to zero on the surface (*e.g.*, Dean and Dalrymple 1984). The kinematic free surface boundary condition is expressed as

$$\frac{\partial \eta'}{\partial t'} + u_1' \frac{\partial \eta'}{\partial x_1'} + u_2' \frac{\partial \eta'}{\partial x_2'} - u_3' \;=\; 0 \qquad \text{at} \quad x_3' = \eta' \tag{2.16}$$

whereas the kinematic bottom boundary condition is

$$u_1' \frac{\partial d'}{\partial x_1'} + u_2' \frac{\partial d'}{\partial x_2'} + u_3' \;=\; 0 \qquad \text{at} \quad x_3' = -d' \tag{2.17}$$

Substitution of (2.4), (2.5) and (2.15) into (2.16) and (2.17) yields

$$\frac{\partial \eta}{\partial t} + u_1 \frac{\partial \eta}{\partial x_1} + \theta_c^2 u_2 \frac{\partial \eta}{\partial x_2} - u_3 = 0 \qquad \text{at} \quad x_3 = \eta \tag{2.18}$$

and

$$u_1 \frac{\partial d}{\partial x_1} + \theta_c^2 u_2 \frac{\partial d}{\partial x_2} + u_3 = 0 \qquad \text{at} \quad x_3 = -d \tag{2.19}$$

For $\theta_c^2 \ll 1$, these boundary conditions may be simplified as

$$\frac{\partial \eta}{\partial t} + u_1 \frac{\partial \eta}{\partial x_1} - u_3 = 0 \qquad \text{at} \quad x_3 = \eta \tag{2.20}$$

and

$$u_1 \frac{\partial d}{\partial x_1} + u_3 = 0 \qquad \text{at} \quad x_3 = -d \tag{2.21}$$

For the dynamic boundary conditions at the free surface $x_3 = \eta$, the tangential and normal stresses at the free surface are assumed to be zero, which can be shown to result in

$$\tau_i = 0 \quad \text{with} \quad i = 1, 2 \qquad \text{at} \quad x_3 = \eta \tag{2.22}$$

and

$$p + \frac{2k}{3\sigma} = 0 \qquad \text{at} \quad x_3 = \eta \tag{2.23}$$

as explained in the following.

Figure 2.2 shows the surface stresses acting on an infinitesimal fluid element with area ABC=dS, area OBC=dS_1, area OAC=dS_2, and area OAB=dS_3. The total stress on the surface dS is $\vec{\Sigma}' = (\Sigma_1', \Sigma_2', \Sigma_3')$ and the unit normal vector perpendicular to dS is $\vec{n}' = (n_1', n_2', n_3')$.

According to Gauss theorem (*e.g.*, Greenberg 1988):

$$\iiint_V \nabla . \vec{A}\, dV = \iint_S \vec{A} . \vec{n}'\, dS \qquad \text{for any } \vec{A} \tag{2.24}$$

With $\vec{A}$=constant, the equation becomes

$$\iint_S \vec{n}' dS = 0$$

where

S = sum of dS, dS_1, dS_2, and dS_3

$\vec{n'}$ = positive outward from dS, dS_1, dS_2, and dS_3

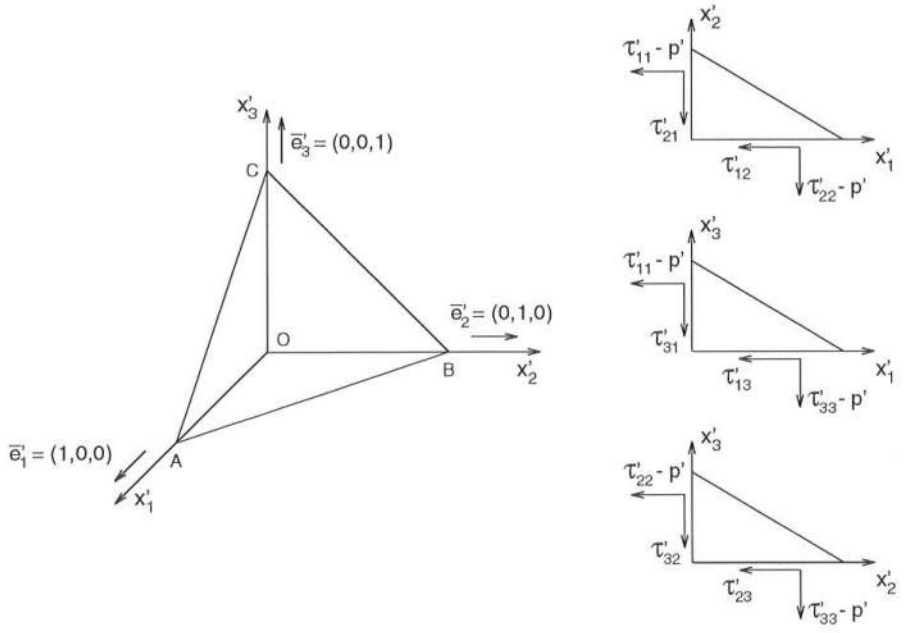

Figure 2.2: Surface stresses acting on fluid element.

Hence

$$\vec{n'}\, dS - \vec{e_1'}\, dS_1 - \vec{e_2'}\, dS_2 - \vec{e_3'}\, dS_3 = 0$$

from which $dS_1 = n_1'\, dS$, $dS_2 = n_2'\, dS$, and $dS_3 = n_3'\, dS$.

Using these relationships, the force balance on fluid element OABC is given by

$$x_1' - \text{direction}: \quad -(\tau_{11}' - p')dS_1 - \tau_{12}' dS_2 - \tau_{13}' dS_3 + \Sigma_1' dS = 0$$

$$x_2' - \text{direction}: \quad -\tau_{21}' dS_1 - (\tau_{22}' - p')dS_2 - \tau_{23}' dS_3 + \Sigma_2' dS = 0$$

$$x_3' - \text{direction}: \quad -\tau_{31}' dS_1 - \tau_{32}' dS_2 - (\tau_{33}' - p')dS_3 + \Sigma_3' dS = 0$$

which can be rewritten as

$$\Sigma_1' = (\tau_{11}' - p')n_1' + \tau_{12}'n_2' + \tau_{13}'n_3'$$
$$\Sigma_2' = \tau_{21}'n_1' + (\tau_{22}' - p')n_2' + \tau_{23}'n_3'$$
$$\Sigma_3' = \tau_{31}'n_1' + \tau_{32}'n_2' + (\tau_{33}' - p')n_3'$$

with $\vec{n}' = \dfrac{\nabla F'}{|\nabla F'|}$ for surface $F'(x_1', x_2', x_3', t') = 0$

For the free surface $F' = x_3' - \eta'(x_1', x_2', t') = 0$, the gradient of the free surface, $\nabla F'$, is given by

$$\nabla F' = (-\frac{\partial \eta'}{\partial x_1'}, -\frac{\partial \eta'}{\partial x_2'}, 1) = (-\frac{1}{\sigma}\frac{\partial \eta}{\partial x_1}, -\frac{\theta_c}{\sigma}\frac{\partial \eta}{\partial x_2}, 1)$$

and

$$|\nabla F'| = \sqrt{\left[\frac{1}{\sigma^2}\left(\frac{\partial \eta}{\partial x_1}\right)^2 + \frac{\theta_c^2}{\sigma^2}\left(\frac{\partial \eta}{\partial x_2}\right)^2 + 1\right]}$$

Hence, under the assumptions of $\sigma^2 \gg 1$ and $\theta_c^2 \ll 1$, the unit vector $\vec{n}'$ is given by

$$\vec{n}' = (n_1', n_2', n_3') = (-\frac{1}{\sigma}\frac{\partial \eta}{\partial x_1}, -\frac{\theta_c}{\sigma}\frac{\partial \eta}{\partial x_2}, 1)$$

The conditions of zero tangential and normal stresses at the free surface thus lead to

$$\begin{aligned}
0 &= \left(-\frac{1}{\sigma}\frac{\partial \eta}{\partial x_1}\right)(\tau_{11}' - p') + \left(-\frac{\theta_c}{\sigma}\frac{\partial \eta}{\partial x_2}\right)\tau_{12}' + \tau_{13}' \\
0 &= \left(-\frac{1}{\sigma}\frac{\partial \eta}{\partial x_1}\right)\tau_{21}' + \left(-\frac{\theta_c}{\sigma}\frac{\partial \eta}{\partial x_2}\right)(\tau_{22}' - p') + \tau_{23}' \\
0 &= \left(-\frac{1}{\sigma}\frac{\partial \eta}{\partial x_1}\right)\tau_{31}' + \left(-\frac{1}{\sigma}\frac{\partial \eta}{\partial x_2}\right)\tau_{32}' + (\tau_{33}' - p')
\end{aligned}$$

Normalization of the above equations using (2.3), (2.4), (2.5), (2.6) and (2.15) yields

$$\begin{aligned}
0 = \left(-\frac{1}{\sigma}\frac{\partial \eta}{\partial x_1}\right)\left[\frac{1}{\sigma}\left(2\nu_t\frac{\partial u_1}{\partial x_1}\right) - \frac{2}{3}k - \sigma p\right] + \left(-\frac{\theta_c}{\sigma}\frac{\partial \eta}{\partial x_2}\right)\frac{\theta_c}{\sigma}\nu_t\left(\frac{\partial u_1}{\partial x_2} + \frac{\partial u_2}{\partial x_1}\right) \\
+\nu_t\left(\frac{\partial u_1}{\partial x_3} + \frac{1}{\sigma^2}\frac{\partial u_3}{\partial x_1}\right) \qquad (2.25)
\end{aligned}$$

$$0 = \left(-\frac{1}{\sigma}\frac{\partial \eta}{\partial x_1}\right)\frac{\theta_c}{\sigma}\nu_t\left(\frac{\partial u_2}{\partial x_1}+\frac{\partial u_1}{\partial x_2}\right)+\left(-\frac{\theta_c}{\sigma}\frac{\partial \eta}{\partial x_2}\right)\left[\frac{\theta_c^2}{\sigma}\left(2\nu_t\frac{\partial u_2}{\partial x_2}\right)-\frac{2}{3}k-\sigma p\right]$$
$$+\theta_c\nu_t\left(\frac{\partial u_2}{\partial x_3}+\frac{1}{\sigma^2}\frac{\partial u_3}{\partial x_2}\right) \tag{2.26}$$

$$0 = \left(-\frac{1}{\sigma}\frac{\partial \eta}{\partial x_1}\right)\nu_t\left(\frac{1}{\sigma^2}\frac{\partial u_3}{\partial x_1}+\frac{\partial u_1}{\partial x_3}\right)+\left(-\frac{\theta_c}{\sigma}\frac{\partial \eta}{\partial x_2}\right)\theta_c\nu_t\left(\frac{1}{\sigma^2}\frac{\partial u_3}{\partial x_2}+\frac{\partial u_2}{\partial x_3}\right)$$
$$+\frac{1}{\sigma}\left(2\nu_t\frac{\partial u_3}{\partial x_3}\right)-\frac{2}{3}k-\sigma p \tag{2.27}$$

Neglecting terms of the order $(\sigma^{-2}), (\theta_c^2)$ and smaller, (2.25), (2.26), and (2.27) may be simplified as

$$0 = \left(-\frac{1}{\sigma}\frac{\partial \eta}{\partial x_1}\right)\left(-\frac{2}{3}k-\sigma p\right)+\nu_t\left(\frac{\partial u_1}{\partial x_3}\right) \tag{2.28}$$

$$0 = \left(-\frac{1}{\sigma}\frac{\partial \eta}{\partial x_2}\right)\left(-\frac{2}{3}k-\sigma p\right)+\nu_t\left(\frac{\partial u_2}{\partial x_3}\right) \tag{2.29}$$

$$0 = -\frac{2}{3}k-\sigma p \tag{2.30}$$

Equation (2.30) corresponds to (2.23), while substitution of (2.30) into (2.28) and (2.29) gives the normalized boundary conditions at the free surface $x_3 = \eta$ given by (2.22) with (2.13).

Integration of the vertical momentum equation (2.14) with respect to x_3 using (2.23) yields

$$p = \eta - x_3 - \frac{2k}{3\sigma} \tag{2.31}$$

which shows that the pressure is approximately hydrostatic below the free surface elevation η where k is on the order of unity or less and σ is relatively large to satisfy $\sigma^2 \gg 1$. Substituting (2.31) into (2.12), the horizontal momentum equations are rewritten as

$$\frac{\partial u_i}{\partial t}+u_1\frac{\partial u_i}{\partial x_1}+u_3\frac{\partial u_i}{\partial x_3} = -\frac{\partial \eta}{\partial x_i}+\frac{\partial \tau_i}{\partial x_3} \tag{2.32}$$

with $i = 1, 2$.

The approximate continuity equation (2.11) and the approximate momentum equations (2.32) are integrated vertically to further simplify the governing equations in the following.

2.2 Depth-Integrated Equations

To reduce computational efforts significantly, the approximate three-dimensional continuity and momentum equations are integrated over the water depth. The depth-integrated continuity equation is obtained by integrating (2.11) with respect to x_3 from the bottom, which is assumed to be fixed and impermeable, to the free surface. Applying Leibniz rule (*e.g.*, Greenberg 1988) and the boundary conditions given by (2.20) and (2.21), the depth-integrated continuity equation is

$$\frac{\partial}{\partial x_1}\int_{-d}^{\eta} u_1\,dx_3 - \underbrace{\left[\frac{\partial \eta}{\partial x_1}u_1 - u_3\right]_{x_3=\eta}}_{=-\frac{\partial \eta}{\partial t}\ (2.21)} - \underbrace{\left[\frac{\partial(-d)}{\partial x_1}u_1 + u_3\right]_{x_3=-d}}_{=0\ (2.20)} = 0$$

and can be rewritten as

$$\frac{\partial h}{\partial t} + \frac{\partial U_1 h}{\partial x_1} = 0 \tag{2.33}$$

with

$$h(t, x_1, x_2) = \eta(t, x_1, x_2) + d(x_1, x_2)$$

and

$$U_1 h = \int_{-d}^{\eta} u_1\,dx_3 \tag{2.34}$$

The depth-integrated horizontal momentum equations are derived in the following. By use of (2.11), the horizontal momentum equations (2.32) can be rewritten as

$$\frac{\partial u_1}{\partial t} + \frac{\partial u_1^2}{\partial x_1} + \frac{\partial u_1 u_3}{\partial x_3} = -\frac{\partial \eta}{\partial x_1} + \frac{\partial \tau_1}{\partial x_3}$$

and

$$\frac{\partial u_2}{\partial t} + \frac{\partial u_1 u_2}{\partial x_1} + \frac{\partial u_2 u_3}{\partial x_3} = -\frac{\partial \eta}{\partial x_2} + \frac{\partial \tau_2}{\partial x_3}$$

Integrating the above equations with respect to x_3 from the bottom to the free surface and applying Leibniz rule and the boundary conditions given by (2.20), (2.21), and (2.22), we obtain

$$\frac{\partial U_1 h}{\partial t} + \frac{\partial}{\partial x_1}\int_{-d}^{\eta} u_1^2\, dx_3 - \underbrace{\left[u_1\left(\frac{\partial \eta}{\partial t} + u_1\frac{\partial \eta}{\partial x_1} - u_3\right)\right]_{x_3=\eta}}_{=0\ [(2.21)]} - \underbrace{\left[u_1\left(u_1\frac{\partial d}{\partial x_1} - u_3\right)\right]_{x_3=-d}}_{=0\ [(2.20)]}$$

$$= -h\frac{\partial \eta}{\partial x_1} + \underbrace{\tau_{s1}}_{=0\ [(2.22)]} - \tau_{b1} \tag{2.35}$$

$$\frac{\partial U_2 h}{\partial t} + \frac{\partial}{\partial x_1}\int_{-d}^{\eta} u_1 u_2\, dx_3 - \underbrace{\left[u_2\left(\frac{\partial \eta}{\partial t} + u_2\frac{\partial \eta}{\partial x_1} - u_3\right)\right]_{x_3=\eta}}_{=0\ [(2.21)]} - \underbrace{\left[u_2\left(u_1\frac{\partial d}{\partial x_1} - u_3\right)\right]_{x_3=-d}}_{=0\ [(2.20)]}$$

$$= -h\frac{\partial \eta}{\partial x_2} + \underbrace{\tau_{s2}}_{=0\ [(2.22)]} - \tau_{b2} \tag{2.36}$$

Rearranging the second term on the left hand sides of (2.35) and (2.36), the depth-integrated horizontal momentum equations are given by

$$\frac{\partial U_1 h}{\partial t} + \frac{\partial}{\partial x_1}\left[hU_1^2 + \int_{-d}^{\eta}(u_1 - U_1)^2\, dx_3\right] = -h\frac{\partial \eta}{\partial x_1} - \tau_{b1} \tag{2.37}$$

$$\frac{\partial U_2 h}{\partial t} + \frac{\partial}{\partial x_1}\left[hU_1U_2 + \int_{-d}^{\eta}(u_1 - U_1)(u_2 - U_2)\, dx_3\right] = -h\frac{\partial \eta}{\partial x_2} - \tau_{b2} \tag{2.38}$$

with

$$U_1 = \frac{1}{h}\int_{-d}^{\eta} u_1\, dx_3 = \text{depth-averaged value of } u_1 \tag{2.39}$$

$$U_2 = \frac{1}{h}\int_{-d}^{\eta} u_2\, dx_3 = \text{depth-averaged value of } u_2 \tag{2.40}$$

In the following, the depth-integrated continuity equation (2.33) and the horizontal momentum equations (2.37) and (2.38) are rewritten using the conventional notations of $x = x_1, y = x_2, u = u_1, v = u_2, U = U_1, V = U_2, \tau_{bx} = \tau_{b1}$, and $\tau_{by} = \tau_{b2}$:

$$\frac{\partial h}{\partial t} + \frac{\partial}{\partial x}(hU) = 0 \tag{2.41}$$

$$\frac{\partial}{\partial t}(hU) + \frac{\partial}{\partial x}(hU^2 + m) = -h\frac{\partial \eta}{\partial x} - \tau_{bx} \quad (2.42)$$

$$\frac{\partial}{\partial t}(hV) + \frac{\partial}{\partial x}(hUV + n) = -h\frac{\partial \eta}{\partial y} - \tau_{by} \quad (2.43)$$

with

$$m = \int_{-d}^{\eta}(u - U)^2 dz \quad (2.44)$$

$$n = \int_{-d}^{\eta}(u - U)(v - V)dz \quad (2.45)$$

The dispersion terms m and n defined in (2.44) and (2.45) express the cross-shore and alongshore momentum flux corrections due to the vertical variations of u and v, respectively. The dispersion terms result from the vertical integration of the horizontal momentum equations (*e.g.,* Rodi 1980). It is noted that (2.41) and (2.42) with $m = 0$ are the same with those used previously for predicting the setup and runup of normally incident waves (*e.g.,* Kobayashi and Wurjanto 1992).

For the case of small angles of incidence, $\theta_c^2 \ll 1$, the dominant cross-shore fluid motion computed using (2.41) and (2.42) is not affected by the secondary longshore fluid motion varying more slowly in the longshore direction. Furthermore, the variations in the y-direction appear only in the term $\partial\eta/\partial y$ in (2.43) and along the seaward boundary of the computation domain. The alongshore momentum equation (2.43) is more sensitive to the gradual alongshore variability. In short, the assumption of $\theta_c^2 \ll 1$ reduces computational efforts considerably and eliminates difficulties associated with lateral boundary conditions for general two-dimensional computations.

In this study, the numerical model is developed in two stages. First, the dispersion terms due to the vertical variations of the horizontal velocities u and v are neglected by setting $m = 0$ and $n = 0$. This 2D model is the extension of the previous one-dimensional model where the predicted horizontal velocities are the depth-averaged velocities only. In the second model, the dispersion terms m and n are included. The vertical profile of u and v is assumed to be cubic on the analogy

between turbulent bores and hydraulic jumps. For brevity, this quasi-3D model is referred to as the '3D model'.

2.3 2D Horizontal Time-Dependent Model

As mentioned before, (2.47) and (2.48) with $m = 0$ are the same as the equations used previously for the one dimensional model of Kobayashi and Wurjanto (1992). They stated that the approximation of $m = 0$ might result in an error on the order of 10%. Their numerical model is extended herein to two horizontal dimensions using the approximation $n = 0$. This is equivalent to neglecting the dispersion terms arising from the unknown vertical variations of the horizontal velocities. The depth-averaged alongshore velocity V is computed using (2.43) for the known values of U and h computed using (2.41) and (2.42).

For the 2D model, the physical bottom shear stresses τ'_{bx} and τ'_{by} are assumed to be expressed as

$$\tau'_{bx} = \frac{1}{2}\rho f'_b \sqrt{(U')^2 + (V')^2}\ U' \tag{2.46}$$

$$\tau'_{by} = \frac{1}{2}\rho f'_b \sqrt{(U')^2 + (V')^2}\ V' \tag{2.47}$$

where f'_b is the bottom friction factor based on the depth-averaged velocities (*e.g.*, Kobayashi *et al.* 1987, 1989). The value of f'_b specified as input is allowed to vary spatially to accommodate the spatial variation of bottom roughness (Kobayashi and Raichle 1994). Normalization of the bottom shear stresses according to (2.5) and (2.6) with (2.13) yields

$$\tau_{bx} = \frac{1}{2}\sigma f'_b \sqrt{U^2 + \theta_c^2 V^2}\ U \tag{2.48}$$

$$\tau_{by} = \frac{1}{2}\sigma f'_b \sqrt{U^2 + \theta_c^2 V^2}\ V \tag{2.49}$$

For $\theta_c^2 \ll 1$, the normalized bottom shear stresses are simplified as

$$\tau_{bx} = f_b|U|U \quad ; \quad \tau_{by} = f_b|U|V \tag{2.50}$$

with

$$f_b = \frac{1}{2}\sigma f_b' \tag{2.51}$$

2.4 Quasi-3D Time-Dependent Model

In this quasi-3D model, the dispersion terms m and n are included to account for the dispersion effects due to the vertical variation of the horizontal velocities u and v. Two new equations for m and n are derived from the corresponding three-dimensional shallow-water momentum equations (2.32) using the algebraic procedure based on the method of moments.

In this model, the bottom boundary layer is not analyzed explicitly and the normalized bottom stresses for $\theta_c^2 \ll 1$ are expressed as

$$\tau_{bx} = f_b|u_b|u_b \quad ; \quad \tau_{by} = f_b|u_b|v_b \quad ; \quad f_b = \frac{1}{2}\sigma f_b' \tag{2.52}$$

in which u_b and v_b are the normalized cross-shore and alongshore velocities immediately outside the bottom boundary layer, respectively, and f_b' is the bottom friction factor based on the near-bottom velocities u_b and v_b and is not exactly the same as the bottom friction factor f_b' used in (2.46) and (2.47), although the same notation is used for simplicity. For normally incident waves, the quadratic friction equation in the forms of (2.50) and (2.52) was shown to relate the bottom shear stress and near-bottom velocity measured inside the surf zone within a factor of two (Cox *et al.* 1996). The bottom friction factors based on the depth-averaged velocity and the near-bottom velocity were also found to be approximately the same within the accuracy of the measurements (Cox *et al.* 1996).

To derive the equation for m, the three-dimensional momentum equation (2.32) with $i = 1$ multiplied by u is integrated from the bottom $z = -d$ to the free surface $z = \eta$. Applying the kinematic boundary conditions (2.20) and (2.21) at the bottom and the free surface, respectively, yields

$$\frac{\partial}{\partial t}\int_{-d}^{\eta} \frac{u^2}{2}\,dz + \frac{\partial}{\partial x}\int_{-d}^{\eta} \frac{u^3}{2}\,dz = hU\frac{\partial \eta}{\partial x} + \int_{-d}^{\eta} u\frac{\partial \tau_x}{\partial z}\,dz \tag{2.53}$$

The integrated equation (2.53) is then simplified using (2.41) multiplied by η to obtain the depth-integrated instantaneous wave energy equation derived by Kobayashi and Wurjanto (1992)

$$\frac{\partial E}{\partial t} + \frac{\partial}{\partial x}(E_F) = -D \tag{2.54}$$

The specific energy E defined as the sum of kinetic and potential energy per unit horizontal area is given by

$$\begin{aligned} E &= \frac{1}{2}\left(\eta^2 + hU^2 + m\right) \qquad \text{for} \quad d > 0 \\ E &= \frac{1}{2}\left(\eta^2 - d^2 + hU^2 + m\right) \qquad \text{for} \quad d < 0 \end{aligned} \tag{2.55}$$

in which the potential energy is taken to be relative to the potential energy in the absence of wave action with SWL at $z = 0$. The energy flux E_F per unit width is expressed as

$$E_F = \eta hU + \frac{1}{2}(hU^3 + 3mU + m_3) \tag{2.56}$$

with m_3 = kinetic energy flux correction due to the third moment of the velocity deviation $(u - U)$ over the depth given by

$$m_3 = \int_{z_b}^{\eta} (u - U)^3 \, dz \tag{2.57}$$

The energy dissipation rate D per unit horizontal area in (2.54) is given by

$$D = \int_{-d}^{\eta} \tau_x \frac{\partial u}{\partial z} \, dz \tag{2.58}$$

where use is made of $\tau_x = 0$ at $z = \eta$ and no-slip condition $u = 0$ at $z = -d$. With the assumption that there is no interaction between the bottom boundary layer and the region above it, the energy dissipation rate D is separated into D_f and D_B (Kobayashi and Wurjanto 1992) where D_f is the energy dissipation rate inside the bottom boundary layer and D_B is the energy dissipation rate outside the bottom boundary layer due to wave breaking.

$$D = D_f + D_B = \int_{-d}^{-d+\delta_b} \tau_x \frac{\partial u}{\partial z} \, dz + \int_{-d+\delta_b}^{\eta} \tau_x \frac{\partial u}{\partial z} \, dz \tag{2.59}$$

The thickness of bottom boundary layer, δ_b, is assumed to be much smaller than the water depth $h = (\eta + d)$.

It has been mentioned before that in this model the bottom boundary layer is not analyzed explicitly. The energy dissipation rate D_f inside the bottom boundary layer may be approximated by (Jonsson and Carlsen 1976)

$$D_f = \tau_{bx} u_b \tag{2.60}$$

By use of (2.13), the energy dissipation rate outside the bottom boundary layer due to wave breaking D_B is rewritten as

$$D_B = \int_{-d}^{\eta} \nu_t \left(\frac{\partial u}{\partial z} \right)^2 dz \tag{2.61}$$

where the lower limit $z = -d$ of the integration should be interpreted at the elevation immediately outside the bottom boundary layer.

Rearranging the instantaneous wave energy equation (2.54) with (2.55), (2.56), (2.59) and (2.60), and by use of the depth-integrated continuity equation (2.41) and the depth-integrated momentum equation (2.42), the equation for the cross-shore momentum flux correction m is derived as (Kobayashi and Johnson 1995)

$$\frac{\partial m}{\partial t} + \frac{\partial}{\partial x}(3mU + m_3) = 2\left(U \frac{\partial m}{\partial x} - \tau_{bx} \tilde{u}_b - D_B \right) \tag{2.62}$$

with

$$\tilde{u}_b = u_b - U \tag{2.63}$$

in which $\tilde{u}_b$ = near bottom cross-shore horizontal velocity correction due to the vertical variation of the cross-shore horizontal velocity u outside the bottom boundary layer.

To derive the equation for n, (2.32) with $i = 1$ multiplied by v and (2.32) with $i = 2$ multiplied by u are added and integrated from $z = -d$ to $z = \eta$. Applying the kinematic and dynamic boundary conditions at the free surface given by (2.20) and

(2.22), respectively, and the kinematic condition (2.21) and the no-slip condition at the bottom yields

$$\frac{\partial}{\partial t}\int_{-d}^{\eta} uv\,dz + \frac{\partial}{\partial x}\int_{-d}^{\eta} u^2 v\,dz = -hV\frac{\partial \eta}{\partial x} - hU\frac{\partial \eta}{\partial y} - \int_{-d}^{\eta}\left(\tau_x\frac{\partial v}{\partial z} + \tau_y\frac{\partial u}{\partial z}\right)dz \quad (2.64)$$

which can be rewritten as

$$\frac{\partial}{\partial t}(hUV + n) + \frac{\partial}{\partial x}(hU^2V + 2Un + Vm + n_3) = -hV\frac{\partial \eta}{\partial x} - hU\frac{\partial \eta}{\partial y} - \int_{-d}^{\eta}\left(\tau_x\frac{\partial v}{\partial z} + \tau_y\frac{\partial u}{\partial z}\right)dz \quad (2.65)$$

with

$$n_3 = \int_{-d}^{\eta}(u-U)^2(v-V)\,dz \quad (2.66)$$

where m and n are defined by (2.44) and (2.45), respectively.

On the other hand, the addition of (2.42) multiplied by V, (2.43) multiplied by U, and (2.41) multiplied by (-UV) yields

$$\frac{\partial}{\partial t}(hUV) + \frac{\partial}{\partial x}(hU^2V) + V\frac{\partial m}{\partial x} + U\frac{\partial n}{\partial x} = -hV\frac{\partial \eta}{\partial x} - hU\frac{\partial \eta}{\partial y} - V\tau_{bx} - U\tau_{by} \quad (2.67)$$

Subtracting (2.67) from (2.65), the equation for the alongshore momentum flux correction n is obtained as

$$\frac{\partial n}{\partial t} + \frac{\partial}{\partial x}(2Un + Vm + n_3) - V\frac{\partial m}{\partial x} - U\frac{\partial n}{\partial x} = V\tau_{bx} + U\tau_{by} - \int_{-d}^{\eta}\left(\tau_x\frac{\partial v}{\partial z} + \tau_y\frac{\partial u}{\partial z}\right)dz \quad (2.68)$$

Similar to (2.59) and with the assumption of a thin boundary layer, the last term on the right hand side of (2.68) may be approximated as

$$\int_{-d}^{\eta}\left(\tau_x\frac{\partial v}{\partial z} + \tau_y\frac{\partial u}{\partial z}\right)dz \simeq \underbrace{\tau_{bx}v_b + \tau_{by}u_b}_{\substack{\text{inside thin bottom}\\ \text{boundary layer}}} + \underbrace{\int_{-d}^{\eta}\left(\tau_x\frac{\partial v}{\partial z} + \tau_y\frac{\partial u}{\partial z}\right)dz}_{\substack{\text{outside bottom}\\ \text{boundary layer}}} \quad (2.69)$$

By use of (2.13), (2.63) and (2.69), (2.68) can be rewritten as

$$\frac{\partial n}{\partial t} + \frac{\partial}{\partial x}(nU + mV + n_3) = V\frac{\partial m}{\partial x} - n\frac{\partial U}{\partial x} - \tilde{v}_b\tau_{bx} - \tilde{u}_b\tau_{by} - 2D_n \quad (2.70)$$

with

$$\tilde{v}_b = v_b - V \tag{2.71}$$

$$D_n = \int_{-d}^{\eta} \nu_t \frac{\partial u}{\partial z}\frac{\partial v}{\partial z}\, dz \tag{2.72}$$

in which $\tilde{v}_b$ = alongshore horizontal velocity correction due to the vertical variation of the alongshore horizontal velocity v immediately outside the bottom boundary layer.

Since the thickness of the bottom boundary layer is assumed to be much smaller than the water depth $h = (\eta + d)$, the lower limit $z = -d$ of the integration in (2.61) and (2.72) should be interpreted at the elevation immediately outside the bottom boundary layer. The contributions of the boundary layer flow, which must satisfy $u = 0$ and $v = 0$ at the bed, to the second moments m and n given by (2.44) and (2.45) and the third moments m_3 and n_3 defined by (2.57) and (2.66), respectively, are assumed to be negligible.

To obtain h, U, V, m and n using (2.41) – (2.43), (2.62) and (2.70), the variables u_b, v_b, m_3, n_3, D_B and D_n need to be expressed in terms of these five unknown variables. As a first attempt to deal with this closure problem, the instantaneous horizontal velocities u and v outside the bottom boundary layer are assumed to be expressed as

$$u(t, x, y, z) = U(t, x, y) + \tilde{u}_b(t, x, y)F(\zeta) \tag{2.73}$$

and

$$v(t, x, y, z) = V(t, x, y) + \tilde{v}_b(t, x, y)F(\zeta) \tag{2.74}$$

with

$$\zeta = \frac{z + d(x, y)}{h(t, x, y)} \tag{2.75}$$

in which F is assumed to be a function of ζ only, with $\zeta = 0$ at $z = -d$ and $\zeta = 1$ at $z = \eta$. The definitions of $\tilde{u}_b$ and $\tilde{v}_b$ in (2.63) and (2.71) require $F = 1$ at the

bottom $\zeta = 0$. Furthermore, the dimensional turbulent eddy viscosity ν_t' outside the bottom boundary layer is assumed to be given by

$$\nu_t' = (C_\ell h')^2 \left| \frac{\partial u'}{\partial z'} \right| \tag{2.76}$$

in which C_ℓ = mixing length parameter. The turbulence measurements inside the surf zone by Cox *et al.* (1994) indicate that the mixing length parameter C_ℓ is on the order of 0.1. Accordingly, the eddy viscosity ν_t normalized in (2.6) may be expressed as

$$\nu_t = \sigma C_\ell^2 h^2 \left| \frac{\partial u}{\partial z} \right| \tag{2.77}$$

Substitution of (2.73), (2.74), and (2.77) into (2.44), (2.45), (2.57), (2.61), (2.66) and (2.72) yields

$$m = C_2 h \tilde{u}_b^2 \quad ; \quad n = C_2 h \tilde{u}_b \tilde{v}_b \quad ; \quad C_2 = \int_0^1 F^2 \, d\zeta \tag{2.78}$$

$$m_3 = C_3 h \tilde{u}_b^3 \quad ; \quad n_3 = C_3 h \tilde{u}_b^2 \tilde{v}_b \quad ; \quad C_3 = \int_0^1 F^3 \, d\zeta \tag{2.79}$$

$$D_B = C_B \sigma C_\ell^2 |\tilde{u}_b|^3 \; ; \; D_n = C_B \sigma C_\ell^2 \, | \, \tilde{u}_b | \tilde{u}_b \tilde{v}_b \; ; \; C_B = \int_0^1 \left| \frac{dF}{d\zeta} \right|^3 d\zeta \tag{2.80}$$

in which the constants C_2, C_3 and C_B can be found for the specified shape function F. To find $\tilde{u}_b$ using (2.78) for the computed $h \geq 0$ and $m \geq 0$, it is assumed that

$$\begin{aligned} \tilde{u}_b &= -\left(\frac{m}{C_2 h} \right)^{\frac{1}{2}} \qquad \text{for} \quad U \geq 0 \\ \tilde{u}_b &= \left(\frac{m}{C_2 h} \right)^{\frac{1}{2}} \qquad \text{for} \quad U < 0 \end{aligned} \tag{2.81}$$

to ensure that $|u_b| \leq |U|$ where $u_b = (U + \tilde{u}_b)$ is the near-bottom cross-shore velocity used in (2.52). After $\tilde{u}_b$ is obtained, then $\tilde{v}_b = n/(C_2 h \tilde{u}_b)$, $v_b = (V + \tilde{v}_b)$, and (2.79) and (2.80) yield m_3, n_3, D_B and D_n.

Finally, the shape function F needs to be specified. Svendsen and Madsen (1984) assumed a cubic velocity profile for their analysis of a single turbulent bore

on a beach. For regular and irregular breaking waves on beaches, the following cubic profile is tentatively assumed:

$$F = 1 - (3 + 0.75a)\,\zeta^2 + a\zeta^3 \qquad \text{for} \quad 0 \le \zeta \le 1 \tag{2.82}$$

in which a = cubic velocity profile parameter. Equations (2.73) and (2.74) require that $F = 1$ at $\zeta = 0$ and the depth-averaged value of F equals zero. Substitution of (2.73) – (2.75) and (2.77) into (2.13) yields the shear stresses τ_x and τ_y. Equation (2.82) predicts zero shear stresses immediately outside the bottom boundary layer in contradiction with the turbulence measurements inside the surf zone by Cox *et al.* (1994). Moreover, the shear stresses at the surface are zero only if $a = 4$. Consequently, (2.82) with the single parameter a may not predict the shear stresses accurately in the vicinity of the free surface and bottom. Comparison of (2.82) and the cubic profile assumed by Svendsen and Madsen (1984) suggests that a is about 3.

Substitution of (2.82) into (2.78) – (2.80) yields the explicit expressions of C_2, C_3 and C_B in terms of a (Kobayashi and Johnson 1995).

$$C_2 = 1 + \frac{2b}{3} + \frac{a}{2} + \frac{b^2}{5} + \frac{ab}{3} + \frac{a^2}{7} \tag{2.83}$$

$$C_3 = 1 + b + \frac{3a}{4} + \frac{3b^2}{5} + ab + \frac{3a^2 + b^3}{7} + \frac{3ab^2}{8} + \frac{a^2 b}{3} + \frac{a^3}{10} \tag{2.84}$$

$$C_B = -\left(2b^3 + \frac{36ab^2}{5} + 9a^2 b + \frac{27a^3}{7}\right) \tag{2.85}$$

where $$b = -(3 + 0.75a) \tag{2.86}$$

For the range of $a = 3 - 4$, the assumed cubic profile F is not very sensitive to the parameter a. Furthermore, $C_2 = 0.49 - 0.55$, $C_3 = -0.07 - 0.00$, and $C_B = 12.3 - 15.2$ for $a = 3 - 4$. The computed results using $C_\ell = 0.1 - 0.2$ in (2.80) and $a = 3 - 4$ in (2.83)–(2.85) are found to be very similar (Johnson *et al.* 1996). The typical values of $C_\ell = 0.1$ and $a = 3$ are hence employed for the 3D computed results presented in Chapters 5 and 6.

2.5 Time-Averaged Continuity and Momentum Equations

The time-dependent models based on the depth-integrated continuity equation (2.41), the depth-integrated cross-shore momentum equation (2.42), and the depth-integrated alongshore momentum equation (2.43) allow us to compute the oscillatory and mean components of the water depth h, depth-averaged cross-shore velocity U, and depth-averaged alongshore velocity V. The time-averaged quantity denoted by an overbar is defined as

$$\overline{M} = \frac{1}{t_{\text{end}} - t_{\text{begin}}} \int_{t_{\text{begin}}}^{t_{\text{end}}} M(t)\, dt \tag{2.87}$$

where

$$\begin{aligned} M &= \text{computed time-varying quantity at given location} \\ t_{\text{begin}} &= \text{normalized time when the time averaging begins} \\ t_{\text{end}} &= \text{normalized time when the time averaging ends} \end{aligned}$$

The time-averaged continuity equation derived from (2.41) is given by

$$\overline{hU} = 0 \tag{2.88}$$

which satisfies the condition of no flux into the impermeable beach. The time-averaged cross-shore momentum equation derived from (2.42) with the assumption that $m = 0$ and $f_b = 0$ is similar to the conventional equation used to predict wave setup (Kobayashi *et al.* 1989). The time-averaged alongshore momentum equation corresponding to (2.43) can be written as

$$\frac{\partial}{\partial x} S_{xy} = -\frac{\partial \overline{n}}{\partial x} - \overline{\tau}_{by} - \overline{h} \frac{\partial \overline{\eta}}{\partial y} - \frac{1}{2} \frac{\partial}{\partial y} \overline{(\eta - \overline{\eta})^2} \tag{2.89}$$

with

$$S_{xy} = \overline{hUV} \tag{2.90}$$

If the mean and variance of the free surface elevation η above SWL do not vary in the alongshore direction, (2.89) is similar to the conventional alongshore momentum

equation in which $\overline{U} \simeq 0$ is assumed and the dispersion term $\overline{n}$ is expressed in the form of lateral mixing (*e.g.*, Longuet-Higgins 1970). In this study, $n = 0$ for the 2D model and n is explicitly computed using (2.70) for the 3D model. The term S_{xy} given by (2.90) may be regarded as the alongshore radiation stress (*e.g.*, Thornton and Guza 1986) where $S_{xy} \simeq \overline{h(U-\overline{U})(V-\overline{V})}$ for $\overline{U} \simeq 0$ and $\overline{hU} = 0$.

2.6 Time-Averaged Energy Equation

The time-averaged cross-shore energy equation corresponding to (2.54) and (2.59) is given by

$$\Delta E + \frac{d}{dx}(\overline{E_F}) = -\overline{D_f} - \overline{D_B} \tag{2.91}$$

with

$$\Delta E = \frac{E(t = t_{\text{end}}) - E(t = t_{\text{begin}})}{t_{\text{end}} - t_{\text{begin}}} \tag{2.92}$$

For regular waves, ΔE defined by (2.92) is zero because of periodicity, whereas for irregular waves, t_{begin} and t_{end} are chosen such that ΔE is negligible to obtain the time-averaged energy equation for a stationary sea state. As a result, ΔE can be deleted from (2.91) but is included for completeness.

In the previous one-dimensional model and the present 2D model, $\overline{D_B}$ is calculated using (2.91) because these models do not include any physical dissipation mechanism associated with wave breaking. For the 3D model, the values of E, E_F, D_f and D_B are computed using (2.55), (2.56), (2.60) and (2.80), respectively. The time-averaged energy equation (2.91) will be used to check the degree of numerical dissipation in Chapters 5 and 6.

Equations (2.61) and (2.62) give $D_B = 0$ if u is independent of z so that $u = U, \tilde{u}_b = 0, m = 0$, and $m_3 = 0$. This proves that the energy dissipation due to wave breaking in the previous one-dimensional model and the present 2D model based on the assumptions of $\tilde{u}_b = 0, m = 0$, and $m_3 = 0$ is solely numerical (Kobayashi and Wurjanto 1992). The normalized energy dissipation rate D_B due

to the vertical variations of τ_x and u outside the boundary layer as given by (2.61) is the same as the dissipation rate due to breaking of normally incident waves used by Svendsen and Madsen (1984).

In addition to the nonlinear shallow water equations used in this study, the motion of waves in the nearshore region is also modeled using the Boussinesq equations. To include energy dissipation due to wave breaking in the Boussinesq equations, Zelt (1991) added a term corresponding to the term m in (2.42) and expressed this term in the form of horizontal momentum diffusion with an artificial viscosity that was calibrated empirically for breaking solitary waves. Schäffer *et al.* (1992) expressed the additional momentum fluxes similar to the terms m and n in (2.42) and (2.43) using a simple surface roller model in which an empirical geometric method was used to estimate the shape and location of the surface roller. However, Zelt (1991) and Schäffer *et al.*992) did not check whether their computed results satisfied the wave energy equation. Consequently, the degree of numerical dissipation in their computed results was not certain.

Chapter 3

NUMERICAL MODELS

The governing equations for the 2D and 3D models are solved numerically using two different numerical methods. The unknown variables for the cross-shore motion in the 2D model are computed using the dissipative Lax-Wendroff method in the same way as the one-dimensional model explained by Kobayashi *et al.* (1987, 1989) since the governing equations for the cross-shore motion for the 2D model are the same as those of the one-dimensional model. The alongshore motion in the 2D model as well as the cross-shore and alongshore motions in the 3D model are solved using the MacCormack method (MacCormack 1969). This method is a simplified variation of the two-step Lax-Wendroff method (*e.g.,* Anderson *et al.* 1984) and has been applied successfully for the computation of unsteady open channel flows with hydraulic jumps (*e.g.,* Fennema and Chaudhry 1986; Gharangik and Chaudhry 1991).

The two models use the same coordinate system, boundary and initial conditions as well as the specified incident wave train at the seaward boundary, although the 3D model requires the additional conditions for the momentum flux correction terms m and n. Figure 3.1 shows the finite difference grid of constant grid sizes Δx and Δy used to solve the governing equations (2.41), (2.42) and (2.43) numerically. The cross-shore coordinate x is taken to be positive landward. The alongshore coordinate y is positive in the downwave direction with $y = 0$ at the upwave boundary. The cross-shore lines in Figure 3.1 are located at $y = (i-1)\Delta y$ with $i = 1, 2, \ldots, I$

where I is the number of the cross-shore lines. The seaward boundary of the computation domain is located at $x = 0$ along the y-axis. Along each cross-shore line, the nodes are located at $x = (j-1)\Delta x$ with $j = 1, 2, \ldots, J$ where J is the number of the cross-shore nodes. The computational shoreline is defined as the location where the normalized instantaneous water depth h equals a small value δ as in the previous one-dimensional model . The initial time $t = 0$ for the computation marching forward in time is taken to be the time when the incident wave train arrives at $x = 0$ and there is no wave action in the region $x \geq 0$ and $y \geq 0$.

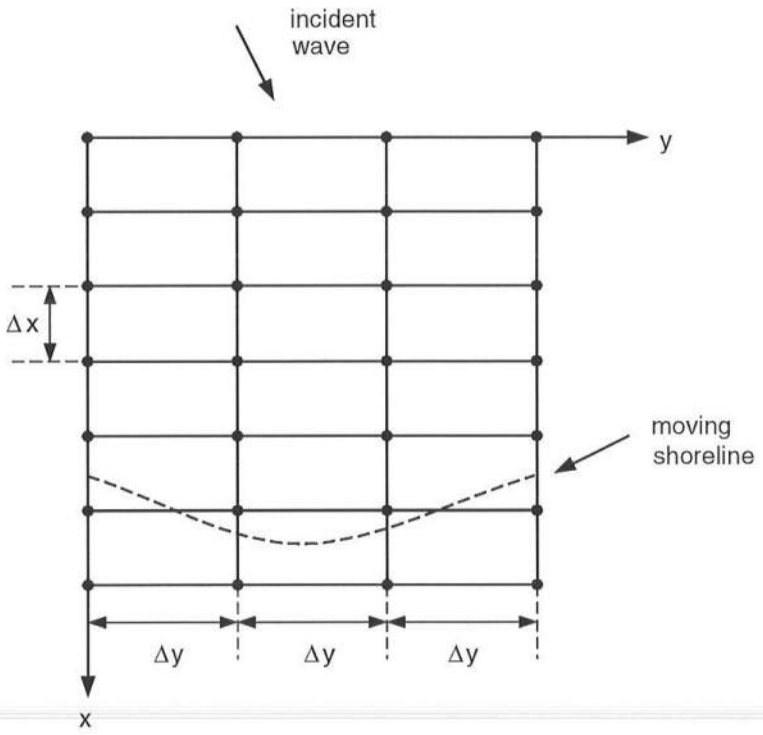

Figure 3.1: Finite difference grid for the numerical models.

The incident wave free surface elevation, $\eta_i(t, y)$, at $x = 0$ and $y = (i-1)\Delta y$ with $i = 1, 2, \ldots, I$ needs to be specified as input to the numerical model. The bottom profile along each of the I cross-shore lines needs to be specified as well unless the bottom profile is assumed to be uniform in the alongshore direction. The value of $d = (h - \eta)$ is the normalized depth below SWL and is known for the specified bottom profile.

In Chapters 4, 5 and 6, the 2D and 3D numerical models will be compared with available data whose beach profile and incident wave conditions may be assumed to be uniform in the alongshore direction. For this case, it is sufficient to compute the unknown variables in the cross-shore direction along three lines at $y = 0$, Δy and $2\Delta y$ with $I = 3$ in Figure 3.1, and then compute the unknown variables involved in the alongshore wave motion along the center line at $y = \Delta y$. The computed η along the three lines are used to ensure the alongshore uniformity of the mean and variance of η appearing in the time-averaged alongshore momentum equation (2.89).

It is also noted that even if the beach profile and incident wave conditions vary gradually alongshore, the developed numerical models should be applicable for the computation of the gradual longshore variations of the wave motion by choosing a larger value of I, provided that lateral boundary conditions do not affect the wave motion in the computation domain. However, computations for this more general case have not been made yet and beyond the scope of this study.

3.1 2D Numerical Model

3.1.1 Summary of Equations

The equations used for the 2D model are summarized in the following. The depth-integrated continuity equation (2.41) and the horizontal momentum equations

(2.42) with $m = 0$ and (2.43) with $n = 0$ are rewritten as

$$\frac{\partial h}{\partial t} + \frac{\partial}{\partial x}(hU) = 0 \tag{3.1}$$

$$\frac{\partial}{\partial t}(hU) + \frac{\partial}{\partial x}(hU^2) = -h\frac{\partial \eta}{\partial x} - \tau_{bx} \tag{3.2}$$

$$\frac{\partial}{\partial t}(hV) + \frac{\partial}{\partial x}(hUV) = -h\frac{\partial \eta}{\partial y} - \tau_{by} \tag{3.3}$$

with

$$\tau_{bx} = f_b|U|U \quad ; \quad \tau_{by} = f_b|U|V \quad ; \quad f_b = \frac{1}{2}\sigma f_b' \tag{3.4}$$

The time-averaged alongshore momentum equation (2.89) with $n = 0$ is given by

$$\frac{\partial}{\partial x}S_{xy} = -\overline{\tau}_{by} - \overline{h}\frac{\partial \overline{\eta}}{\partial y} - \frac{1}{2}\frac{\partial}{\partial y}\overline{(\eta - \overline{\eta})^2} \tag{3.5}$$

with

$$S_{xy} = \overline{hUV} \tag{3.6}$$

where overbar denotes time-averaged quantities defined in (2.87).

The time-averaged cross-shore energy equation (2.91) is given by

$$\Delta E + \frac{d}{dx}(\overline{E_F}) = -\overline{D_f} - \overline{D_B} \tag{3.7}$$

with

$$E = \frac{1}{2}\left(\eta^2 + hU^2\right) \qquad \text{for} \quad d > 0$$

$$E = \frac{1}{2}\left(\eta^2 - d^2 + hU^2\right) \qquad \text{for} \quad d < 0 \tag{3.8}$$

$$\Delta E = \frac{E(t = t_{\text{end}}) - E(t = t_{\text{begin}})}{t_{\text{end}} - t_{\text{begin}}} \tag{3.9}$$

$$E_F = \eta hU + \frac{1}{2}(hU^3) \tag{3.10}$$

$$D_f = \tau_{bx}\, U \tag{3.11}$$

$\overline{D_B}$ is calculated using (3.7).

3.1.2 Numerical Method for Cross-Shore Wave Motion

For the known values of h, η, U and V at the time level t and at all the nodes used in the computation, the values of these variables at the next time level $t^* = (t + \Delta t)$, which is denoted by the superscript asterisk, are computed in sequence. The time step size Δt is allowed to vary in a manner similar to the existing one-dimensional model where Δt is reduced in a semi-automated way whenever numerical difficulties occur at the moving shoreline.

Since the governing equations of the 2D model for the cross-shore wave motion with small angles of wave incidence are the same as those of the one-dimensional model along each of the cross-shore lines, the values of h_j^* and U_j^* at the node j with $j = 1, 2, \ldots, s^*$ are computed from (3.1) and (3.2) using the dissipative Lax-Wendroff method in the same way as the one-dimensional model explained by Kobayashi *et al.* (1987, 1989). The integer s^* indicates the wet node next to the moving shoreline at the next time level t^*. The incident wave train η_i specified at $x = 0$ for each of the cross-shore lines is the input to this cross-shore fluid motion computation.

The Lax-Wendroff finite difference method is discussed briefly in the following for the subsequent comparison between this method and the MacCormack method used to solve the alongshore momentum equation (3.3). The continuity and cross-shore momentum equations (3.1) and (3.2) and (3.4) can be rewritten in terms of h and $q = hU$ as follows:

$$\frac{\partial h}{\partial t} + \frac{\partial q}{\partial x} = 0 \tag{3.12}$$

$$\frac{\partial q}{\partial t} + \frac{\partial}{\partial x}\left(\frac{q^2}{h} + \frac{h^2}{2}\right) = -\theta h - f_b|U|U \tag{3.13}$$

where $\theta = \partial(-d)/\partial x$ is the normalized local slope.

Equations (3.12) and (3.13) can be combined and expressed in the following vector form:

$$\frac{\partial \mathbf{U}}{\partial t} + \frac{\partial \mathbf{F}}{\partial x} + \mathbf{G} = 0 \tag{3.14}$$

where

$$\mathbf{U} = \begin{bmatrix} q \\ h \end{bmatrix} \tag{3.15}$$

$$\mathbf{F} = \begin{bmatrix} F_1 \\ F_2 \end{bmatrix} = \begin{bmatrix} \frac{q^2}{h} + \frac{1}{2}h^2 \\ q \end{bmatrix} \tag{3.16}$$

$$\mathbf{G} = \begin{bmatrix} G_1 \\ G_2 \end{bmatrix} = \begin{bmatrix} \theta h + f_b|U|U \\ 0 \end{bmatrix} \tag{3.17}$$

Using a Taylor series expansion, $\mathbf{U}^*$ at the next time level $t^* = (t + \Delta t)$ is expressed as

$$\mathbf{U}^*(x, t + \Delta t) = \mathbf{U}(x, t) + \Delta t \frac{\partial \mathbf{U}(x,t)}{\partial t} + \frac{(\Delta t)^2}{2} \frac{\partial^2 \mathbf{U}(x,t)}{\partial t^2} + \mathrm{O}\,(\Delta t)^3 \tag{3.18}$$

The main feature of the Lax-Wendroff scheme of second-order accuracy in Δt and Δx is to express the temporal derivatives in (3.18) in terms of the spatial derivatives. From (3.14), the temporal derivatives of $\mathbf{U}$ can be written as

$$\frac{\partial \mathbf{U}}{\partial t} = -\frac{\partial \mathbf{F}}{\partial x} - \mathbf{G} \tag{3.19}$$

and

$$\frac{\partial^2 \mathbf{U}}{\partial t^2} = \frac{\partial}{\partial t}\left(-\frac{\partial \mathbf{F}}{\partial x} - \mathbf{G}\right) = -\frac{\partial}{\partial x}\left(\frac{\partial \mathbf{F}}{\partial t}\right) - \frac{\partial \mathbf{G}}{\partial t} \tag{3.20}$$

in which $\partial \mathbf{F}/\partial t$ can be expressed as

$$\frac{\partial \mathbf{F}}{\partial t} = \mathbf{A}\frac{\partial \mathbf{U}}{\partial t} = \mathbf{A}\left(-\frac{\partial \mathbf{F}}{\partial x} - \mathbf{G}\right) \tag{3.21}$$

where

$$\mathbf{A} = \frac{\partial \mathbf{F}}{\partial \mathbf{U}} = \begin{bmatrix} 2\frac{q}{h} & \left(h - \frac{q^2}{h^2}\right) \\ 1 & 0 \end{bmatrix} \tag{3.22}$$

By use of (3.12) and (3.13), $\partial G_1/\partial t$ can be shown to be expressed as

$$\frac{\partial G_1}{\partial t} = -\theta \frac{\partial q}{\partial x} + 2 f_b \frac{|U|}{h}\left[(U^2 - h)\frac{\partial h}{\partial x} - U\frac{\partial q}{\partial x} - \theta h - f_b|U|U\right] \tag{3.23}$$

Substitution of (3.19) and (3.20) together with (3.21) into (3.18) leads to

$$\mathbf{U}^* = \mathbf{U} - \Delta t \left[\frac{\partial \mathbf{F}}{\partial x} + \mathbf{G}\right] + \frac{(\Delta t)^2}{2}\left[\frac{\partial}{\partial x}\left[\mathbf{A}\left(\frac{\partial \mathbf{F}}{\partial x} + \mathbf{G}\right)\right] - \frac{\partial \mathbf{G}}{\partial t}\right] + \mathrm{O}\,(\Delta t)^3 \quad (3.24)$$

Using the finite difference approximations of second-order accuracy in Δx, (3.24) can be shown to be expressed in the following explicit form:

$$\mathbf{U}_j^* = \mathbf{U}_j - \lambda\left[\frac{1}{2}(\mathbf{F}_{j+1} - \mathbf{F}_{j-1}) + \Delta x \mathbf{G}_j\right] + \frac{(\lambda)^2}{2}(\mathbf{g}_j - \mathbf{g}_{j-1} - \Delta x \mathbf{S}_j) + \mathbf{D}_j \quad (3.25)$$

with

$$\lambda = \frac{\Delta t}{\Delta x} \quad (3.26)$$

$$\mathbf{g}_j = \frac{1}{2}(\mathbf{A}_{j+1} + \mathbf{A}_j)\left[\mathbf{F}_{j+1} - \mathbf{F}_j + \frac{\Delta x}{2}(\mathbf{G}_{j+1} + \mathbf{G}_j)\right] \quad (3.27)$$

$$\mathbf{S}_j = \begin{bmatrix} \Delta x e_j - \frac{1}{2}\theta_j(q_{j+1} - q_{j-1}) \\ 0 \end{bmatrix} \quad (3.28)$$

$$e_j = 2(f_b)_j \frac{|U_j|}{h_j}\left[(U_j^2 - h_j)\frac{h_{j+1} - h_{j-1}}{2\Delta x} - U_j \frac{q_{j+1} - q_{j-1}}{2\Delta x} - \theta_j h_j - (f_b)_j |U_j| U_j\right] \quad (3.29)$$

The superscript asterisk indicates the quantities at the next time level $t^* = (t + \Delta t)$ and the subscript j denotes the nodal location at $x_j = (j-1)\Delta x$.

The vector $\mathbf{D}_j$ in (3.25) represents the additional term for damping high frequency parasitic oscillations, which tend to appear at the rear of a breaking wave, and is given by (Kobayashi *et al.* 1987)

$$\mathbf{D}_j = \frac{\lambda}{2}\left[\mathbf{Q}_j(\mathbf{U}_{j+1} - \mathbf{U}_j) - \mathbf{Q}_{j-1}(\mathbf{U}_j - \mathbf{U}_{j-1})\right] \quad (3.30)$$

with

$$\mathbf{Q}_j = p_j \mathbf{I} + \frac{1}{2} r_j (\mathbf{A}_j + \mathbf{A}_{j+1}) \quad (3.31)$$

where $\mathbf{I}$ = unit matrix. The coefficients p_j and r_j are given by

$$p_j = -\frac{1}{2(c_{j+1} + c_j)}\left[\epsilon_1 |\phi_{j+1} - \phi_j|(\psi_{j+1} + \psi_j) - \epsilon_2 |\psi_{j+1} - \psi_j|(\phi_{j+1} + \phi_j)\right] \quad (3.32)$$

$$r_j = \frac{\epsilon_1 |\phi_{j+1} - \phi_j| - \epsilon_2 |\psi_{j+1} - \psi_j|}{(c_{j+1} + c_j)} \quad (3.33)$$

with

$$c = \sqrt{h} \quad ; \quad \phi = U + c \quad ; \quad \psi = U - c$$

where ϵ_1 and ϵ_2 are the positive numerical damping coefficients on the order of unity.

3.1.3 Numerical Method for Alongshore Velocity

Along each of the cross-shore lines excluding the cross-shore lines at $i = 1$ and I, the value of V_j^* at the node j with $j = 1, 2, \ldots, s^*$ is computed using (3.3), which is expressed in terms of $q_\ell = hV$ where $q_{\ell_j} = h_j V_j$ and $q_{\ell_j}^* = h_j^* V_j^*$

$$\frac{\partial q_\ell}{\partial t} + \frac{\partial q_\ell U}{\partial x} = -h\frac{\partial \eta}{\partial y} - f_b|U|V \tag{3.34}$$

This equation for q_ℓ is solved numerically using the MacCormack method (MacCormack 1969). The use of the MacCormack method eliminates the algebraic manipulations involved in the Lax-Wendroff method to express the temporal derivatives in terms of the spatial derivatives performed in (3.19), (3.20) and (3.21).

The MacCormack method consists of two steps, *i.e.*, predictor and corrector steps, with forward and backward spatial differences which are interchangeable (Anderson *et al.* 1984). When applied to (3.34), the **predictor** step is expressed as

$$\dot{q}_{\ell_j} = q_{\ell_j} - \frac{\Delta t}{\Delta x}\left(U_{j+1}^* q_{\ell_{j+1}} - U_j^* q_{\ell_j}\right) - \Delta t\left[h_j^*\left(\frac{\partial \eta^*}{\partial y}\right)_j + (f_b)_j |U_j^*| V_j\right] \tag{3.35}$$

for $j = 1, 2, \ldots, s^*$ where U_j^* and h_j^* have already been computed and $U_{s^*+1}^* = 0$ landward of the moving shoreline node s^*. The term $\dot{q}_{\ell_j}$ given by (3.35) is a temporary predicted value at the next time level t^*. The normalized bottom friction factor f_b given by (3.4) is allowed to vary spatially and $(f_b)_j$ is used in (3.35). The **corrector** step of the MacCormack method is given by

$$\ddot{q}_{\ell_j} = \dot{q}_{\ell_j} - \frac{\Delta t}{\Delta x}\left(U_j^* \dot{q}_{\ell_j} - U_{j-1}^* \dot{q}_{\ell_{j-1}}\right) - \Delta t\left[h_j^*\left(\frac{\partial \eta^*}{\partial y}\right)_j + (f_b)_j |U_j^*| \dot{q}_{\ell_j}\left(h_j^*\right)^{-1}\right] \tag{3.36}$$

for $j = 2, 3, \ldots, s^*$. Finally, the value of $q^*_{\ell_j}$ at the node j and at the next time level t^* is computed from

$$q^*_{\ell_j} = \frac{1}{2}\left(q_{\ell_j} + \ddot{q}_{\ell_j}\right) + D_j \qquad \text{for } j = 2, 3, \ldots, s^* \tag{3.37}$$

with

$$D_j = \frac{\epsilon_\ell \Delta t}{2\Delta x}\left[|U^*_{j+1} - U^*_j|\left(q_{\ell_{j+1}} - q_{\ell_j}\right) - |U^*_j - U^*_{j-1}|\left(q_{\ell_j} - q_{\ell_{j-1}}\right)\right] \tag{3.38}$$

where D_j is the numerical damping term based on the procedure described in Richtmyer and Morton (1967) and ϵ_ℓ is the numerical damping coefficient. The term D_j is added to (3.37) except for $j = s^*$ and $q^*_{\ell_j} = 0$ with $j = (s^* + 1), \ldots, J$ landward of the moving shoreline.

The term $(\partial \eta^*/\partial y)_j$ for the cross-shore line i in (3.35) and (3.36) is approximated by a central finite difference based on the computed values of η^*_j at the two adjacent cross-shore lines $(i - 1)$ and $(i + 1)$ if all the nodes j at the three lines $(i - 1), i$ and $(i + 1)$ are wet and seaward of the shoreline whose location varies for the three cross-shore lines. Otherwise, this term is set to be zero because the alongshore fluid motion turns out to be sensitive to spurious shoreline oscillations of a short duration unlike the cross-shore fluid motion as will be explained in Section 4.3 in relation to the computed results of V and U.

The numerical damping term D_j given by (3.38) tends to reduce high-frequency numerical oscillations at the rear of a steep wave front without modifying the slowly varying part of the alongshore fluid motion. The computed alongshore fluid motions with the numerical damping coefficient $\epsilon_\ell = 0$ and 1 are found to be the same except for the slight reduction of the high-frequency numerical oscillations as will be shown in Section 4.3. The computed results presented in Sections 4.2 and 4.3 are based on $\epsilon_\ell = 1$ unless stated otherwise.

It is noted that a forward spatial difference is used for the second term on the right hand side of the predictor equation (3.35), while a backward spatial difference

is used for this term in the corrector equation (3.36). This is because the spatial difference in the predictor equation is recommended to be in the direction of propagation of wave fronts (Anderson *et al.* 1984). Since wave breaking can also occur during wave downrush on the slope, the computation is also made by reversing the spatial differencing in the predictor and corrector equations. The computed results are found to be practically the same as will be shown in Section 4.3. As a result, the MacCormack method based on (3.35) and (3.36) should be applicable to wave fronts propagating seaward as well as landward.

3.1.4 Numerical Stability Criterion for MacCormack Method

The linear stability criterion for the MacCormack method applied to (3.34) without the terms on the right hand side of (3.34) is the Courant condition (*e.g.*, Ryrie 1983; Anderson *et al.* 1984) as shown in the following. For the linear stability criterion, U is assumed constant. The predictor, corrector and final steps of the MacCormack method applied to this simplified alongshore momentum equation may be written as

$$\begin{aligned}
\dot{q}_{\ell_j} &= q_{\ell_j} - \frac{U\Delta t}{\Delta x}\left(q_{\ell_{j+1}} - q_{\ell_j}\right) \\
\ddot{q}_{\ell_j} &= \dot{q}_{\ell_j} - \frac{U\Delta t}{\Delta x}\left(\dot{q}_{\ell_j} - \dot{q}_{\ell_{j-1}}\right) \\
q^*_{\ell_j} &= \frac{1}{2}\left(q_{\ell_j} + \ddot{q}_{\ell_j}\right)
\end{aligned}$$

Substituting $\ddot{q}_{\ell_j}$ into the final step, the value of $q^*_{\ell_j}$ is given by

$$q^*_{\ell_j} = \frac{1}{2}\left[(2-2\alpha^2)q_{\ell_j} + (\alpha^2-\alpha)q_{\ell_{j+1}} + (\alpha^2+\alpha)q_{\ell_{j-1}}\right]$$

with

$$\alpha = \frac{U\Delta t}{\Delta x}$$

For the assumed form of $q_{\ell_j} = e^{at}e^{ikx_j}$, with $x_j = (j-1)\Delta x$, the amplification factor G for the time step from the present time t to the next time level $t^* = (t + \Delta t)$ is written as

$$G = e^{a\Delta t} = 1 - \alpha^2(1 - \cos k\Delta x) - i\alpha \sin k\Delta x$$

The stability condition of $|G| \leq 1$ is satisfied if $\alpha \leq 1$ (Anderson *et al.* 1984), which leads to

$$\frac{|U_m|\Delta t}{\Delta x} \leq 1 \tag{3.39}$$

where $|U_m|$ is the maximum absolute value of U in the computation domain.

On the other hand, the numerical stability criterion for the dissipative Lax-Wendroff method used to solve (3.12) and (3.13) is given by (Packwood 1980)

$$\frac{\Delta t}{\Delta x} < \frac{1}{|U_m| + c_m}\left[(1 + \frac{\epsilon^2}{4})^{1/2} - \frac{\epsilon}{2}\right] \tag{3.40}$$

with

c_m = maximum value of $\sqrt{h} > 0$

ϵ = maximum value of ϵ_1 and ϵ_2 introduced in (3.32) and (3.33).

Using the following inequalities

$$\left[(1 + \frac{\epsilon^2}{4})^{1/2} - \frac{\epsilon}{2}\right] \leq 1 \quad \text{for } \epsilon \geq 0$$

and

$$|U_m| + c_m > |U_m|$$

(3.40) leads to

$$\frac{\Delta t}{\Delta x} < \frac{1}{|U_m|} \tag{3.41}$$

As a result, the Courant condition for the MacCormack method used to solve (3.37) is satisfied if the numerical stability criterion for the dissipative Lax-Wendroff method used to solve (3.12) and (3.13) is satisfied.

For the computed results presented in Chapter 4, the value of Δt smaller than that required by the numerical stability criterion is used to minimize spurious shoreline oscillations as will be discussed in more detail in Section 4.3.

3.1.5 Seaward Boundary Algorithm

The value of $q^*_{\ell_1}$ with $j = 1$ at the seaward boundary $x = 0$ can not be computed using (3.37). To devise an appropriate seaward boundary algorithm, the depth-integrated alongshore momentum equation (3.34) is expressed in the following characteristic form as depicted in Figure 3.2:

$$\frac{\partial V}{\partial t} + U\frac{\partial V}{\partial x} = -\frac{\partial \eta}{\partial y} - \frac{f_b|U|V}{h} \tag{3.42}$$

where use is made of the continuity equation (3.12). The variation of the characteristic variable V along $dx/dt = U$ is given by (3.42).

To compute V_1^* and $q^*_{\ell_1} = h_1^* V_1^*$ using (3.42), the linear approximation of $dx/dt = U$ at $x = 0$ and at the time level t^* is expressed as $\delta x/\Delta t = U_1^*$ as depicted in Figure 3.2 where the spatial increment δx satisfies $|\delta x| < \Delta x$ due to the Courant condition, $\Delta t \leq \Delta x/|U_m|$. If $U_1^* > 0$, $\delta x > 0$ and the characteristic path is directed landward. If $U_1^* < 0$, $\delta x < 0$ and the characteristic path is directed seaward. The finite difference approximation of (3.42) along this characteristic path may be expressed as

$$\frac{V_1^* - \hat{V}}{\Delta t} = -\left(\frac{\partial \eta^*}{\partial y}\right)_1 - \frac{(f_b)_1\,|U_1^*|V_1^*}{h_1^*} \tag{3.43}$$

where $\hat{V}$ is the value of V at the start of this characteristic path at the time level t with $\delta x = \Delta t\, U_1^*$.

If $U_1^* > 0$, the characteristic variable propagates into the computation domain and $\hat{V}$ should be specified as input; however, this option is not feasible for practical applications. Alternatively, $\hat{V}$ may be estimated from V_1 and V_2 by interpolation for $U_1^* < 0$ and by extrapolation for $U_1^* > 0$.

$$\hat{V} = V_1 - \frac{\Delta t}{\Delta x} U_1^* (V_2 - V_1) \tag{3.44}$$

Substitution of (3.44) into (3.43) yields

$$V_1^* = \left[1 + \Delta t \frac{(f_b)_1\,|U_1^*|}{h_1^*}\right]^{-1} \left[V_1 - \frac{\Delta t}{\Delta x}\, U_1^* (V_2 - V_1) - \Delta t \left(\frac{\partial \eta^*}{\partial y}\right)_1\right] \tag{3.45}$$

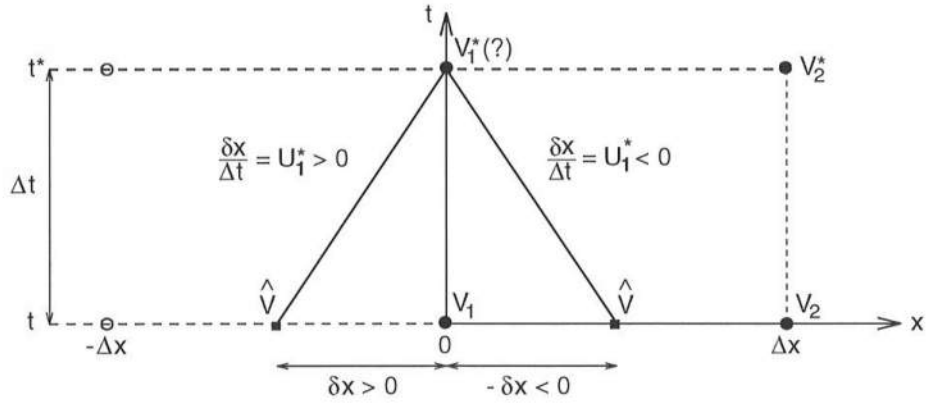

Figure 3.2: Sketch of seaward boundary algorithm for alongshore velocity V.

where $(\partial\eta^*/\partial y)_1$ is approximated by a central finite difference based on the computed values η_1^* at the two adjacent cross-shore lines.

3.2 3D Numerical Model

3.2.1 Summary of Equations

The equations used for the quasi-3D model are summarized in the following. The depth-integrated continuity equation (2.41) and the horizontal momentum equations (2.42) and(2.43) are given by

$$\frac{\partial h}{\partial t} + \frac{\partial}{\partial x}(hU) = 0 \tag{3.46}$$

$$\frac{\partial}{\partial t}(hU) + \frac{\partial}{\partial x}(hU^2 + m) = -h\frac{\partial \eta}{\partial x} - \tau_{bx} \tag{3.47}$$

$$\frac{\partial}{\partial t}(hV) + \frac{\partial}{\partial x}(hUV + n) = -h\frac{\partial \eta}{\partial y} - \tau_{by} \tag{3.48}$$

with

$$m = \int_{-d}^{\eta}(u-U)^2 dz \quad ; \quad n = \int_{-d}^{\eta}(u-U)(v-V)dz \tag{3.49}$$

$$\tau_{bx} = f_b|u_b|u_b \quad ; \quad \tau_{by} = f_b|u_b|v_b \quad ; \quad f_b = \frac{1}{2}\sigma f_b' \tag{3.50}$$

$$u_b = U + \tilde{u}_b \quad ; \quad v_b = V + \tilde{v}_b \tag{3.51}$$

The two additional equations (2.62) and (2.70) for m and n are given by

$$\frac{\partial m}{\partial t} + \frac{\partial}{\partial x}(3mU + m_3) = 2\left(U\frac{\partial m}{\partial x} - \tilde{u}_b\tau_{bx} - D_B\right) \tag{3.52}$$

$$\frac{\partial n}{\partial t} + \frac{\partial}{\partial x}(nU + mV + n_3) = V\frac{\partial m}{\partial x} - n\frac{\partial U}{\partial x} - \tilde{v}_b\tau_{bx} - \tilde{u}_b\tau_{by} - 2D_n \tag{3.53}$$

with

$$\tilde{u}_b = -\left(\frac{m}{C_2 h}\right)^{\frac{1}{2}} \text{ for } U \geq 0 \; ; \; \tilde{u}_b = \left(\frac{m}{C_2 h}\right)^{\frac{1}{2}} \text{ for } U < 0 \; ;$$

$$\tilde{v}_b = \frac{n}{C_2 h \tilde{u}_b} \; ; \; C_2 = \int_0^1 F^2 \, d\zeta \tag{3.54}$$

$$m_3 = C_3 h \tilde{u}_b^3 \quad ; \quad n_3 = C_3 h \tilde{u}_b^2 \tilde{v}_b \quad ; \quad C_3 = \int_0^1 F^3 \, d\zeta \tag{3.55}$$

$$D_B = C_B \sigma C_\ell^2 |\tilde{u}_b|^3 \; ; \; D_n = C_B \sigma C_\ell^2 |\tilde{u}_b| \tilde{u}_b \tilde{v}_b \; ; \; C_B = \int_0^1 \left|\frac{dF}{d\zeta}\right|^3 d\zeta \tag{3.56}$$

The instantaneous cross-shore and alongshore velocities are expressed as

$$u(t,x,y,z) = U(t,x,y) + \tilde{u}_b(t,x,y)F(\zeta) \tag{3.57}$$

$$v(t,x,y,z) = V(t,x,y) + \tilde{v}_b(t,x,y)F(\zeta) \tag{3.58}$$

with

$$\zeta = \frac{z + d(x,y)}{h(t,x,y)} \tag{3.59}$$

and

$$F = 1 - (3 + 0.75a)\,\zeta^2 + a\zeta^3 \qquad \text{for} \quad 0 \leq \zeta \leq 1 \tag{3.60}$$

The typical values of $C_\ell = 0.1$ and $a = 3$ are employed for the 3D computations. For $a = 3, C_2 = 0.55, C_3 = -0.07$ and $C_B = 15.2$.

The time-averaged alongshore momentum equation (2.89) is given by

$$\frac{\partial}{\partial x}S_{xy} = -\frac{\partial \overline{n}}{\partial x} - \overline{\tau}_{by} - \overline{h}\frac{\partial \overline{\eta}}{\partial y} - \frac{1}{2}\frac{\partial}{\partial y}\overline{(\eta - \overline{\eta})^2} \tag{3.61}$$

with

$$S_{xy} = \overline{hUV} \tag{3.62}$$

The time-averaged cross-shore energy equation (2.91) is given by

$$\Delta E + \frac{d}{dx}(\overline{E_F}) = -\overline{D_f} - \overline{D_B} \tag{3.63}$$

with

$$\begin{aligned}
E &= \frac{1}{2}\left(\eta^2 + hU^2 + m\right) \qquad \text{for} \quad d > 0 \\
E &= \frac{1}{2}\left(\eta^2 - d^2 + hU^2 + m\right) \qquad \text{for} \quad d < 0 \qquad (3.64) \\
\Delta E &= \frac{E(t = t_{\text{end}}) - E(t = t_{\text{begin}})}{t_{\text{end}} - t_{\text{begin}}} \qquad (3.65) \\
E_F &= \eta hU + \frac{1}{2}(hU^3 + 3mU + m_3) \qquad (3.66) \\
D_f &= \tau_{bx} u_b \qquad (3.67) \\
D_B &= C_B \sigma C_\ell^2 |\tilde{u}_b|^3 \qquad (3.68)
\end{aligned}$$

The numerical energy dissipation rate, $\overline{D}_{\text{numerical}}$, is defined as

$$\overline{D}_{\text{numerical}} = -\Delta E - \frac{d}{dx}(\overline{E_F}) - \overline{D_f} - \overline{D_B} \tag{3.69}$$

which will be zero if the computed results satisfy (3.63).

3.2.2 Numerical Procedures

The 2D numerical model presented in Section 3.1 is extended herein to include the two additional equations (3.52) and (3.53) for m and n, respectively. The coordinate system, boundary and initial conditions as well as the specified incident wave train at the seaward boundary remain the same. For the known values of η, $h = (\eta + d)$, U, m, V and n at the time level t and at all the nodes used in the computation, the values of these variables at the next time level $t^* = (t + \Delta t)$, which are denoted by the superscript asterisk, are computed in sequence. The variable time step size Δt is determined for each time step using an approximate numerical stability criterion for the explicit finite difference method adopted in the following.

First, along each of the cross-shore lines, the values of η_j^*, $h_j^* = (\eta_j^* + d_j)$, U_j^* and m_j^* at the node j with $j = 1, 2, \cdots, s^*$ are computed from (3.46), (3.47) and (3.52) for the incident wave train η_i specified at $x = 0$. The integer s^*, which must be less than J, indicates the wet node next to the moving shoreline at the next time level $t = t^*$. To compute the cross-shore wave motion along each line, the computer program VBREAK developed for normally incident waves, as described in detail in the report by Kobayashi and Johnson (1995), is modified slightly for the obliquely incident wave trains. VBREAK solves (3.46), (3.47) and (3.52) using the MacCormack method (MacCormack 1969).

The variable time step size Δt is determined at the beginning of each time step using an approximate equation

$$\Delta t = \frac{C_n \, \Delta x}{\max\left(|U_j| + \sqrt{h_j}\right)} \qquad \text{for} \quad j = 1, 2, \cdots, s \tag{3.70}$$

in which C_n is the Courant number and the denominator in (3.70) is the maximum value of $(|U_j| + \sqrt{h_j})$ at all the wet nodes at the present time t. The stability criterion for the MacCormack method applied to (3.46) and (3.47) with $m = 0$ and without the terms on the right hand side of (3.47) is $C_n \leq 1$ (*e.g.,* Anderson *et al.* 1984). Equation (3.70) is approximate because the characteristic equations corresponding to (3.46), (3.47) and (3.52) with $m \neq 0$ can not be expressed in simple analytical forms. Moreover, (3.70) does not account for the shoreline algorithm which tends to suffer numerical difficulties. Consequently, the value of C_n less than unity is specified as input to adjust Δt for successful computation.

Use of the MacCormack method results in numerical high-frequency oscillations which tends to appear at the rear of a breaking wave, especially on a gentle slope (Kobayashi and Johnson 1995). The procedure for smoothing these high-frequency numerical oscillations presented by Jameson *et al.* (1981) and summarized by Chaudhry (1993) for hydraulic jumps is modified slightly for breaking waves on a sloping beach. This modified smoothing procedure is presented in detail by

Kobayashi and Johnson (1995), who have stated that for breaking waves on gently sloping beaches, the numerical damping coefficient κ specified as input to VBREAK on the order of unity is necessary to damp the high-frequency oscillations whereas for waves surging on steep slopes of coastal structure, the value of κ on the order of 0.1 appears to be sufficient. The computed results for different values of κ were presented by Johnson *et al.* (1996).

The seaward boundary algorithm for h_1^* and U_1^* at $x = 0$ is based on the characteristic equations derived from (3.46) and (3.47) in a manner similar to that devised by Kobayashi *et al.* (1987, 1989) for the case of $m = 0$. To obtain the value of m_1^* at $x = 0$, (3.52) for $m = C_2 h \tilde{u}_b^2$ from (3.54) is rewritten in terms of $\tilde{u}_b$ and approximated by an explicit first-order finite difference based on the known values at the nodes $j = 1$ and 2. This is because $m = 0$ is a trivial solution of (3.52) for $x \geq 0$ and $t \geq 0$ for the initial condition $m = 0$ at $t = 0$. This problem could be avoided if the value of m associated with the vertical variation of u at $x = 0$ were known in the presence of reflected waves. On the other hand, the landward boundary algorithm dealing with the moving shoreline is a minor extension of that used by Kobayashi *et al.* (1987) for the case of $m = 0$ where the vertical variation of u is assumed to be small in the vicinity of the moving shoreline.

After computing the values of η_j^*, h_j^*, U_j^* and m_j^* with $j = 1, 2, \cdots, s^*$ for each line, the values of V_j^* and n_j^* at the node j with $j = 1, 2, \cdots, s^*$ along the middle cross-shore line are computed using (3.48) and (3.53) which are expressed in the following vector form:

$$\frac{\partial \mathbf{V}}{\partial t} + \frac{\partial \mathbf{P}}{\partial x} + \mathbf{R} = \mathbf{0} \tag{3.71}$$

with

$$\mathbf{V} = \begin{bmatrix} q_\ell \\ n \end{bmatrix} \quad ; \quad \mathbf{P} = \begin{bmatrix} P_1 \\ P_2 \end{bmatrix} \quad ; \quad \mathbf{R} = \begin{bmatrix} R_1 \\ R_2 \end{bmatrix} \tag{3.72}$$

and

$$P_1 = U^* q_\ell + n \tag{3.73}$$

$$P_2 = nU^* + m^* V + C_3 h^* \left(\tilde{u}_b^*\right)^2 \tilde{v}_b \tag{3.74}$$

$$R_1 = h^* \frac{\partial \eta^*}{\partial y} + f_b |u_b^*| v_b \tag{3.75}$$

$$R_2 = f_b |u_b^*| u_b^* \tilde{v}_b + f_b |u_b^*| \tilde{u}_b^* v_b + 2 C_B \sigma C_\ell^2 |\tilde{u}_b^*| \tilde{u}_b^* \tilde{v}_b - V \frac{\partial m^*}{\partial x} + n \frac{\partial U^*}{\partial x} \tag{3.76}$$

where $q_\ell = hV$ and use is made of (3.50), (3.55) and (3.56). The computed values of h^*, U^*, $m^* = C_2 h^* (\tilde{u}_b^*)^2$, $\tilde{u}_b^*$ and $u_b^* = (\tilde{u}_b^* + U^*)$ at the next time level t^* along the middle cross-shore line i are used in (3.73) – (3.76). The term $(\partial \eta^* / \partial y)_j$ for the cross-shore line i at the node j is approximated by a central finite difference based on the computed values of η^* at the node j at the two adjacent cross-shore lines $(i-1)$ and $(i+1)$ if all the nodes j at the three lines $(i-1), i$, and $(i+1)$ are wet and seaward of the shoreline whose location varies for the three cross-shore lines. Otherwise, this term is set to be zero.

For the known values of $q_\ell = hV$, $n = C_2 h \tilde{u}_b \tilde{v}_b$ from (3.54) and $v_b = (V + \tilde{v}_b)$ from (3.51) at the present time t along the cross-shore line, (3.71) is solved using the MacCormack method whose accuracy is second order in time and space. The predictor and corrector steps of the MacCormack method and the value of $\mathbf{V}_j^*$ at the node j and at the next time level t^* are expressed as

$$\dot{\mathbf{V}}_j = \mathbf{V}_j - \frac{\Delta t}{\Delta x} \left(\mathbf{P}_{j+1} - \mathbf{P}_j\right) - \Delta t \mathbf{R}_j \tag{3.77}$$

$$\ddot{\mathbf{V}}_j = \dot{\mathbf{V}}_j - \frac{\Delta t}{\Delta x} \left(\dot{\mathbf{P}}_j - \dot{\mathbf{P}}_{j-1}\right) - \Delta t \dot{\mathbf{R}}_j \tag{3.78}$$

$$\mathbf{V}_j^* = \frac{1}{2} \left(\mathbf{V}_j + \ddot{\mathbf{V}}_j\right) \qquad \text{for} \quad j = 1, 2, \cdots, s^* \tag{3.79}$$

Equation (3.77) yields the temporary predicted values of $\dot{q}_{\ell_j}$ and $\dot{n}_j$. Use is made of $\dot{V}_j = \dot{q}_{\ell_j} / h_j^*$, $(\dot{\tilde{v}}_b)_j = \dot{n}_j / [C_2 h_j^* (\tilde{u}_b)_j^*]$ and $(\dot{v}_b)_j = [(\dot{\tilde{v}}_b)_j + \dot{V}_j]$ to compute $\dot{\mathbf{P}}_j$ and $\dot{\mathbf{R}}_j$ in (3.78). The terms $\partial m^* / \partial x$ and $\partial U^* / \partial x$ in (3.76) are approximated by the forward and backward spatial differences in (3.77) and (3.78), respectively, to

be consistent with the forward and backward spatial differences of $\partial \mathbf{P}/\partial x$ used in (3.78) and (3.79).

The moving shoreline is accounted for in (3.77) by setting $\mathbf{P}_j = \mathbf{0}$ at $j = (s^* + 1)$ for the dry node landward of the moving shoreline. As for the seaward boundary algorithm at the node $j = 1$, the 2D model used the characteristic equation (3.42) for the case of $n = 0$. An alternative and simpler algorithm is adopted herein considering the difficulty in deriving the characteristic equations corresponding to (3.71). The imaginary node at $j = 0$ is added to compute $\ddot{\mathbf{V}}_1$ using (3.78) in which the linearly extrapolated values of $\dot{\mathbf{P}}_0 = (2\dot{\mathbf{P}}_1 - \dot{\mathbf{P}}_2)$, $U_0^* = (2U_1^* - U_2^*)$ and $m_0^* = (2m_1^* - m_2^*)$ at the node $j = 0$ are employed for the backward spatial differences involved in (3.78).

After $q_{\ell_j}^*$ and n_j^* with $j = 1, 2, \cdots, s^*$ are computed using (3.79), $V_j^* = q_{\ell_j}^*/h_j^*$ is computed and the procedure used to smooth h_j^*, U_j^* and m_j^* is applied to smooth V_j^* and n_j^*. The values of $(\tilde{v}_b)_j^*$ and $(v_b)_j^*$ are then computed using the smoothed V_j^* and n_j^* together with (3.54) and (3.51). Finally, the values of these variables for $j \geq (s^* + 1)$ are set to be zero for the dry nodes landward of the moving shoreline.

Chapter 4

COMPARISON OF THE 2D MODEL WITH AVAILABLE DATA

The 2D numerical model developed in Section 3.1 is compared with regular wave laboratory data as well as field data. First, the incident wave profiles used in these comparisons are described in the following.

4.1 Incident Wave Profiles

4.1.1 Regular Waves

The incident wave profile at the seaward boundary needs to be specified as input to the numerical model. The obliquely incident **regular** wave train $\eta_i'(t', y')$ at $x' = 0$ for the small angles of incidence θ_i in radian is assumed to be in the following dimensional form:

$$\eta_i'(t', y') = \text{ periodic function of } \left(\frac{t'}{T'} - \frac{y'}{L'/\theta_i}\right) = \frac{1}{T'}\left(t' - \frac{y'}{C'/\theta_i}\right) \tag{4.1}$$

in which

L' = wavelength at the seaward boundary

$C' = L'/T'$ = phase velocity at the seaward boundary

Equation (4.1) accounts for the phase or time lag along the alongshore coordinate y'. The periodic function in (4.1) is specified using Stokes second-order or cnoidal

wave theory depending on the value of Ursell parameter U_r in the same way as in the existing one-dimensional model (Kobayashi *et al.* 1987) where U_r is defined as

$$U_r = \frac{L^2}{d_t} \tag{4.2}$$

with

$L = L'/d'_t$ = normalized wavelength at the seaward boundary

$d_t = d'_t/H'$ = normalized water depth at the seaward boundary

The periodic function in (4.1) is specified using Stokes second-order theory if $U_r < 26$ and using cnoidal wave theory if $U_r \geq 26$. The dimensional wave train $\eta'_i(t', y')$ is computed using (4.1) and normalized using (2.4) and (2.15).

4.1.2 Irregular Waves

On the other hand, the incident **random** wave train at the seaward boundary is assumed to be unidirectional and expressible in the following dimensional form:

$$\eta'_i(t', y') = \sum_{n=1}^{N} C'_n \cos\left(2\pi f'_n t' - \theta_i k'_n y' + \Phi_n + \Delta\Phi\right) \tag{4.3}$$

with

$$\begin{aligned}
f'_n &= n\Delta f' = \text{frequency} \\
\Delta f' &= \frac{1}{t'_{\max}} = \text{frequency band width} \\
t'_{\max} &= \text{computation duration} \\
N &= \frac{t'_{\max}}{2\Delta t'_s} = \text{number of harmonics} \\
\Delta t'_s &= \text{sampling rate} \\
k'_n &= \text{wave number for } f'_n \text{ based on linear wave theory} \\
\theta_i &= \text{representative incident wave angle } (\theta_i^2 \ll 1) \\
\Phi_n &= \text{random phase angle in the range } 0 - 2\pi \\
C'_n &= [2S'(f'_n)\Delta f']^{1/2} = \text{amplitude}
\end{aligned}$$

$$
\begin{aligned}
S'(f'_n) &= \text{measured incident wave frequency spectrum} \\
\Delta\Phi &= \text{phase shift chosen such that } \eta'_i = 0 \text{ at } t' = 0 \\
&\quad \text{as well as } \frac{\partial \eta'_i}{\partial t'} > 0 \text{ at } t' = 0 \text{ and } y' = 0
\end{aligned}
$$

The incident random wave train η'_i at given y' is computed using an inverse fast Fourier transform of the following equation obtained from (4.3):

$$
\eta'_i(t', y') = \sum_{n=1}^{N} [a'_n \cos(2\pi f'_n t') + b'_n \sin(2\pi f'_n t')] \tag{4.4}
$$

with

$$
\begin{aligned}
a'_n &= C'_n \cos(k'_n \theta_i y' - \Phi_n - \Delta\Phi) \\
b'_n &= C'_n \sin(k'_n \theta_i y' - \Phi_n - \Delta\Phi)
\end{aligned}
$$

The phase shift $\Delta\Phi$ in (4.3) is introduced to satisfy the initial conditions of $\eta'_i = 0$ at $t' = 0$. The condition of $\partial\eta'_i/\partial t' > 0$ at $t' = 0$ is imposed to produce initial longshore current in the downwave direction for positive θ_i for the coordinate system shown in Figure 3.1. This procedure reduces the transient duration associated with the slow development of longshore current as will be shown in Section 4.3. To satisfy the above two conditions, the phase shift $\Delta\Phi$ is computed from (4.3) with $\eta'_i = 0$ at $t' = 0$ and $y' = 0$

$$
\tan \Delta\Phi = \frac{\sum_{n=1}^{N} C'_n \cos \Phi_n}{\sum_{n=1}^{N} C'_n \sin \Phi_n} \tag{4.5}
$$

which has two roots in the range $0 \leq \Delta\Phi \leq 2\pi$. The condition of $\partial\eta'_i/\partial t' > 0$ at $t' = 0$ and $y' = 0$ requires that

$$
\sum_{n=1}^{N} C'_n 2\pi f'_n \sin(\Phi_n + \Delta\Phi) \leq 0 \tag{4.6}
$$

Only one of the two roots obtained from (4.5) satisfies (4.6).

The incident random wave profile η'_i at given y' is computed using (4.4) with (4.5) and (4.6). Since (4.5) does not ensure $\eta'_i = 0$ at $t' = 0$ for $y' > 0$, the computed values of η'_i at $t' = 0$ for $y' > 0$ are adjusted as will be explained in Section 4.3.

4.2 Comparison with Regular Wave Data

Visser (1991) conducted eight monochromatic wave experiments in 34 m long, 16.6 m wide and 0.68 m deep wave basin. A pumping system was installed to ensure the alongshore uniformity of longshore current. The beaches were made of concrete with 1:10 and 1:20 slopes. Detailed data on uniform longshore currents, local wave heights, angles of wave incidence, wave setup and runup were tabulated. The observations were started 60 minutes after the start of the wave generator to eliminate start-related variations in flow and wave fields. Current velocities were measured using a dye method whereas wave runup was measured visually.

4.2.1 Input Parameters

The numerical model is compared with four experiments for which the seaward boundary location can be taken to be in relatively shallow water seaward of the breaker line. Table 4.1 lists the experiment number used by Visser (1991) and the slope and incident wave characteristics specified as input to the numerical model where

$\tan\theta'$ = uniform slope

d'_t = water depth below SWL at the seaward boundary located at $x' = 0$

T' = regular wave period used for the normalization

H' = incident regular wave height at $x' = 0$ used for the normalization

θ_i = angle in degrees of wave incidence at $x' = 0$

σ = ratio between the cross-shore and vertical length scales defined as $T'(g/H')^{\frac{1}{2}}$ in (2.6)

θ_c = θ_i = reference incident wave angle in radian used for the normalization

ξ = surf similarity parameter (Battjes 1974) given by $\xi = \sigma \tan\theta'/\sqrt{2\pi}$.

Table 4.1: Incident waves at seaward boundary $x' = 0$.

Expt. No.	$\tan\theta'$	d_t' (cm)	T' (s)	H' (cm)	θ_i (deg)	σ	θ_c^2	ξ
2	0.101	21.1	1.00	9.5	26.0	10.2	0.206	0.409
3	0.101	21.3	1.00	8.7	14.2	10.6	0.061	0.428
4	0.050	18.5	1.02	7.9	13.9	11.4	0.059	0.227
5	0.050	18.2	1.85	9.0	12.9	19.3	0.051	0.385

For these experiments, plunging breakers were observed. The assumptions of $\sigma^2 \gg 1$ and $\theta_c^2 \ll 1$ may be appropriate except for experiment 2 with $\theta_c^2 = 0.206$. The only empirical parameter involved in the numerical model is the bottom friction factor f_b' in (2.51) where $f_b' \simeq 0.05$ has been used for predicting wave runup on smooth slopes in small-scale experiments (*e.g.*, Kobayashi *et al.* 1989). The value of $f_b' = 0.05$ is used here for both cross-shore and alongshore fluid motions.

The normalized grid sizes Δx and Δy in Figure 3.1 need to be chosen to be small enough to resolve breaking waves in the surf and swash zones. For these experiments of alongshore uniformity, it is sufficient to use the three cross-shore lines at $y = 0$, Δy and $2\,\Delta y$ in Figure 3.1. The value of Δx is selected to be on the order of 0.01, corresponding to 200 grid spacings between the seaward boundary and the still water shoreline. The value of Δy is chosen to be the same as Δx to yield the same spatial resolution in the normalized coordinates. A limited sensitivity analysis with $(\Delta y/\Delta x) \simeq 1, 2, 5$, and 10 has indicated that the computed results for experiment 2 remain essentially the same as long as Δy is on the order of Δx as will be shown in Figure 4.10 as an example.

The incident wave train η_i as a function of time t at longshore location $y = 0, \Delta y$ and $2\,\Delta y$ is computed using (4.1) and normalized using (2.4) and (2.5). The incident wave train η_i at $y = 0$ is computed in the same way as in the existing one-dimensional model (*e.g.*, Kobayashi *et al.* 1987) whereas the time series of η_i at

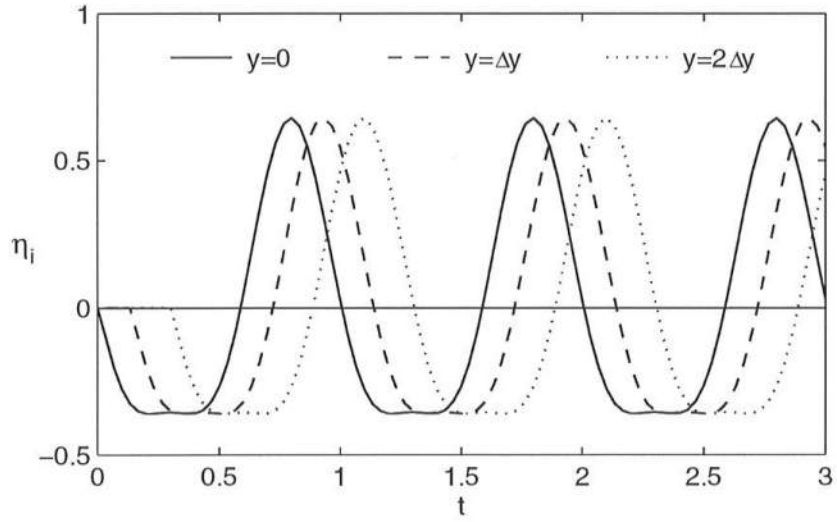

Figure 4.1: Example of incident regular wave trains at $y = 0$, Δy, $2\,\Delta y$ (alongshore phase shift is exaggerated for clarity).

$y = \Delta y$ and $2\,\Delta y$ are computed using the computed time series of $\eta_i(t, 0)$ with the alongshore phase shifts depending on the characteristics of the incident wave and the value of Δy. As an example, Figure 4.1 shows a Stokes second-order incident wave train for experiment 2 at location $y = 0, \Delta y$ and $2\,\Delta y$ where the alongshore phase shifts have been exaggerated for clarity.

4.2.2 Computed Time Series

The detailed computed results for experiment 2 are presented as an example. The temporal and cross-shore variations of the free surface elevation η, the depth-averaged cross-shore velocity U, and the depth-averaged alongshore velocity V are stored along the center line at $y = \Delta y$.

The temporal variations of η, U and V for the duration $0 \leq t \leq 300$ at $x = 0$ (at the seaward boundary), $x = 0.509$ (immediately seaward of the breaker line), $x = 0.770$ (in the outer surf zone), $x = 1.550$ (in the inner surf zone), and $x = 2.265$ (in the swash zone) are shown in Figures 4.2, 4.3 and 4.4, respectively. The

cross-shore fluid motion represented by η and U computed using (3.12) and (3.13) becomes periodic fairly quickly for $t \gtrsim 20$ as has been the case with the previous one-dimensional computations for beaches (*e.g.*, Kobayashi *et al.* 1989). The alongshore fluid motion represented by V computed using (3.34) becomes periodic very slowly especially in the vicinity of the breaker line. The very slow response of the alongshore fluid motion is qualitatively consistent with the analytical result of Ryrie (1983) for the periodic solution development as well as the experimental procedure adopted by Visser (1991) who made measurements one hour after the start of the wave maker. In light of Figure 4.4, the time averaging denoted by the overbar in the following is performed for the duration $200 \leq t \leq 300$.

The computed cross-shore variations of $\overline{\eta}$, $\eta_{\rm rms}$, $\overline{U}$, $U_{\rm rms}$, $\overline{V}$ and $V_{\rm rms}$ for experiment 2 are shown in Figure 4.5 where the root-mean-square values representing the magnitude of the oscillatory components are defined as

$$\eta_{\rm rms}^2 = \overline{(\eta - \overline{\eta})^2} \;\; ; \;\; U_{\rm rms}^2 = \overline{\left(U - \overline{U}\right)^2} \;\; ; \;\; V_{\rm rms}^2 = \overline{\left(V - \overline{V}\right)^2} \tag{4.7}$$

For example, if $\eta = 0.5\cos(2\pi t)$, $\overline{\eta} = 0$ and $\eta_{\rm rms} = 1/\sqrt{8} = 0.35$. The normalized uniform slope is indicated by the dashed-dotted straight line in the top panel in Figure 4.5. The upper limit of the wave setup $\overline{\eta}$ is the maximum runup elevation on the slope above SWL because $\overline{h} \geq 0$ in the region wetted by water. The increase of $\overline{\eta}$ and the decrease of $\eta_{\rm rms}$ in the surf and swash zones are approximately linear. On the other hand, $U_{\rm rms}$ decreases slowly in the surf zone and rapidly in the swash zone. $\overline{U}$ is negative and represents the cross-shore return current as explained by Kobayashi *et al.* (1989). The longshore current $\overline{V}$ is dominant in the surf zone and the oscillatory component $V_{\rm rms}$ decreases approximately linearly in the surf and swash zones.

Figure 4.6 shows the computed cross-shore variations of the normalized quantities involved in the time-averaged cross-shore wave energy equation (3.7) and the time-averaged alongshore momentum equation (3.5). In Figure 4.6, $\overline{E}$ = specific

energy per unit horizontal area; $\overline{E_F}$ = energy flux per unit width; $\overline{D_f}$ = energy dissipation rate due to bottom friction per unit horizontal area; $\overline{D_B}$ = energy dissipation rate due to wave breaking per unit horizontal area; S_{xy} = alongshore radiation stress given by (3.6); and $f_b\overline{|U|V}$ = alongshore bottom shear stress.

Figure 4.6 indicates that the energy dissipation due to wave breaking is dominant and does not occur suddenly in this numerical model which does not account for wave breaking explicitly (Kobayashi and Wurjanto 1992). For these experiments of alongshore uniformity, the computed alongshore gradients of the mean and variance of η are negligible and the time-averaged alongshore momentum equation (3.5) reduces to $dS_{xy}/dx = -f_b\overline{|U|V}$. Figure 4.6 also shows that S_{xy} decreases monotonically in the surf and swash zones. The computed cross-shore variations of dS_{xy}/dx and $-f_b\overline{|U|V}$ are essentially the same where $f_b\overline{|U|V}$ is plotted to distinguish the two curves.

4.2.3 Comparison with Measurements

Figure 4.7 compares the measured and computed cross-shore variations of the normalized local wave height H for each of the four experiments listed in Table 4.1. The agreement is very good in view of no adjustable parameter included in this numerical model to initiate wave breaking. However, it should be stated that this numerical model can not predict wave shoaling without wave breaking over a long distance (Kobayashi *et al.* 1989).

Figure 4.8 compares the measured and computed cross-shore variations of the normalized wave setup $\overline{\eta}$ together with the normalized uniform slope indicated by the dashed line for each of the four experiments. The agreement is good in the swash zone but the computed mean water level rises too rapidly landward of the breaker line as was the case with the previous comparison by Kobayashi *et al.* (1989). The numerical model does not predict the transition zone of constant wave

set-down whose effects on surf zone hydrodynamics were reviewed and elaborated by Nairn *et al.* (1990).

Table 4.2 shows the comparisons of the measured and computed maximum setup and runup for the four experiments. The computed maximum setup and runup correspond to the mean and maximum shoreline elevations, respectively, measured by hypothetical wires placed parallel to and above the uniform slope at elevations of 1, 5 and 10 mm, whereas the actual measurements were made visually.

The computed maximum setup and runup are not very sensitive to the wire elevations and in fair agreement with the measured values except that the numerical model with the bottom friction factor $f_b' = 0.05$ slightly underpredicts the visually measured runup. It is also noted that the swash oscillations in the regular wave experiments are very narrow in comparison to swash oscillations on natural beaches that tend to be dominated by low-frequency motions (Guza and Thornton 1982, Holman and Sallenger 1985).

Table 4.2: Measured and computed maximum setup and runup.

Expt. No.	Maximum Setup				Runup			
	Computed			Meas.	Computed			Meas.
	1mm	5mm	10mm		1mm	5mm	10mm	
2	0.34	0.29	0.26	0.29	0.38	0.35	0.35	0.43
3	0.34	0.28	0.25	0.31	0.38	0.35	0.35	0.47
4	0.19	0.17	0.17	0.20	0.20	0.20	0.21	0.24
5	0.28	0.23	0.21	0.27	0.31	0.29	0.29	0.34

Figure 4.9 compares the measured and computed cross-shore variations of the longshore current $\overline{V}$ for the four experiments. The numerical model with $f_b' = 0.05$ predicts the magnitude of $\overline{V}$ but can not predict the shape of $\overline{V}$ probably because the numerical model based on (3.3) does not include lateral mixing (dispersion) and it can not predict the transition zone as shown in Figure 4.8. Comparing

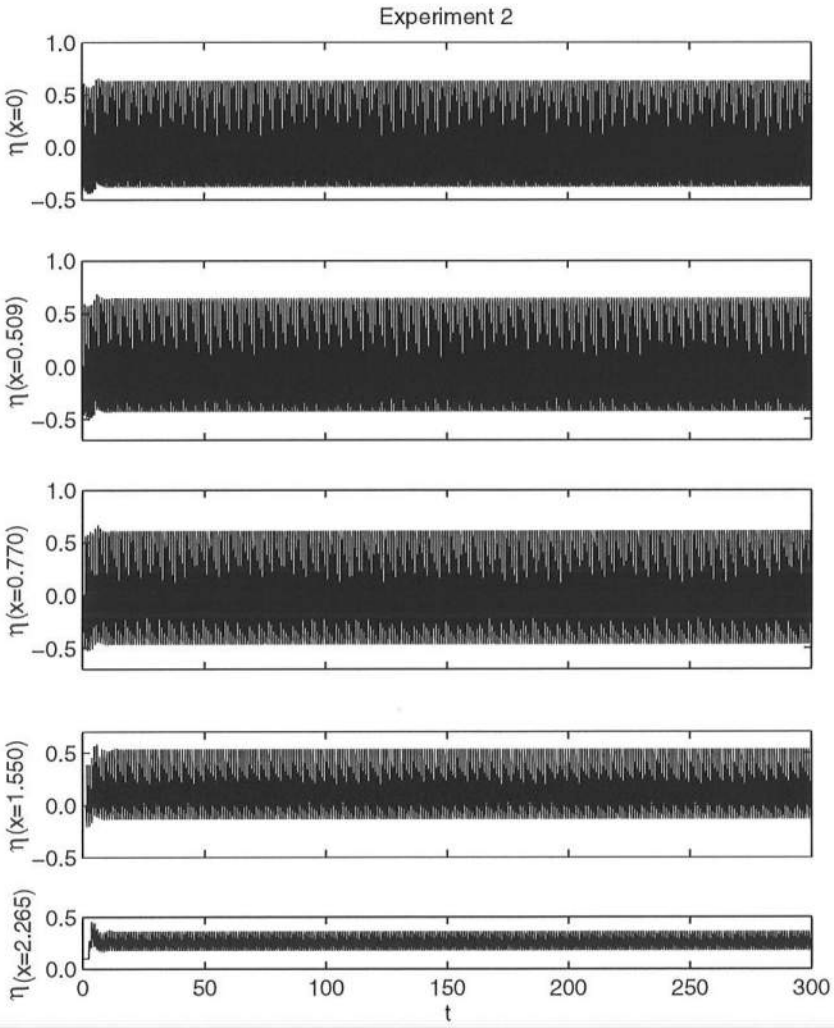

Figure 4.2: Computed temporal variations of free surface elevation η at x=0, 0.509, 0.770, 1.550 and 2.265.

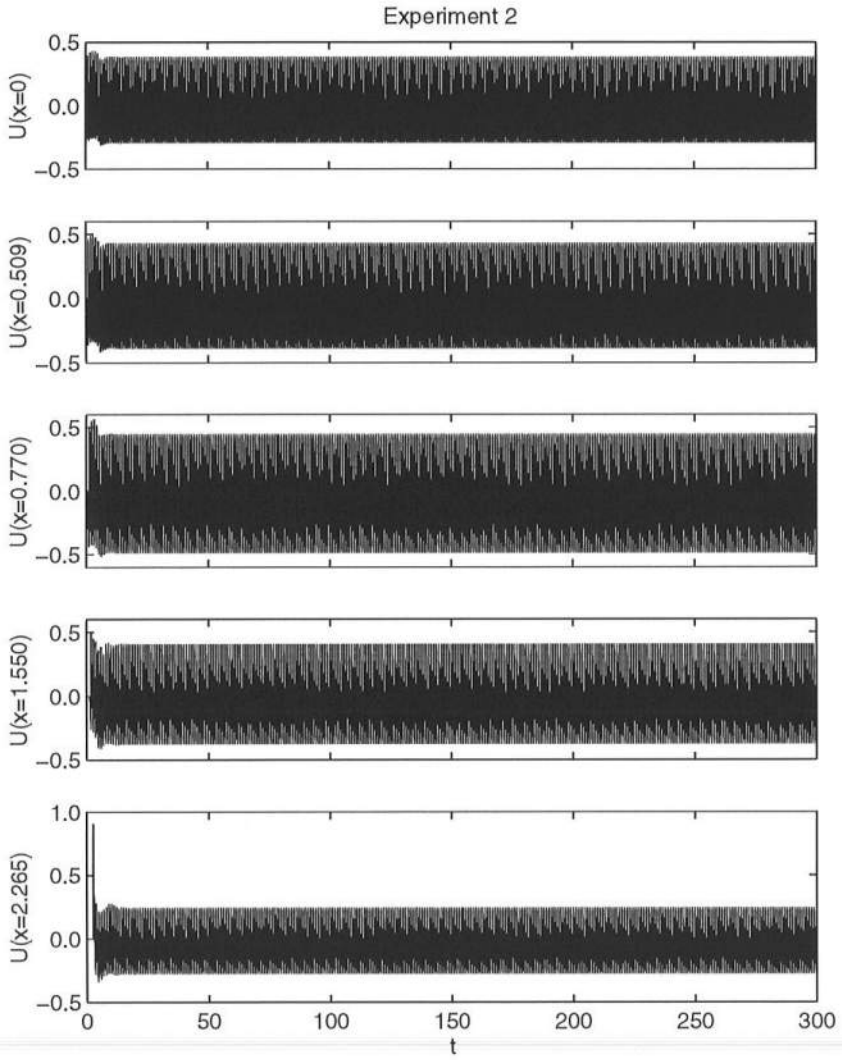

Figure 4.3: Computed temporal variations of depth-averaged cross-shore velocity U at $x = 0, 0.509, 0.770, 1.550$ and 2.265.

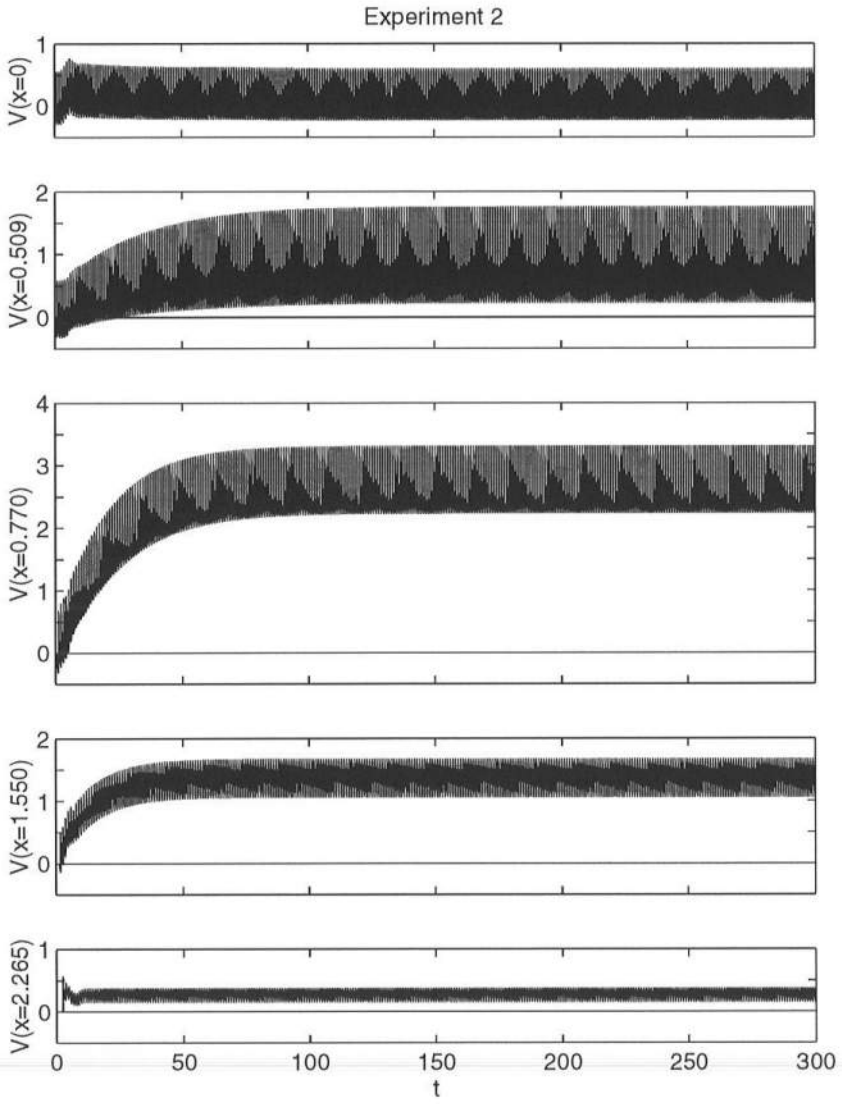

Figure 4.4: Computed temporal variations of depth-averaged alongshore velocity V at $x = 0, 0.509, 0.770, 1.550$ and 2.265.

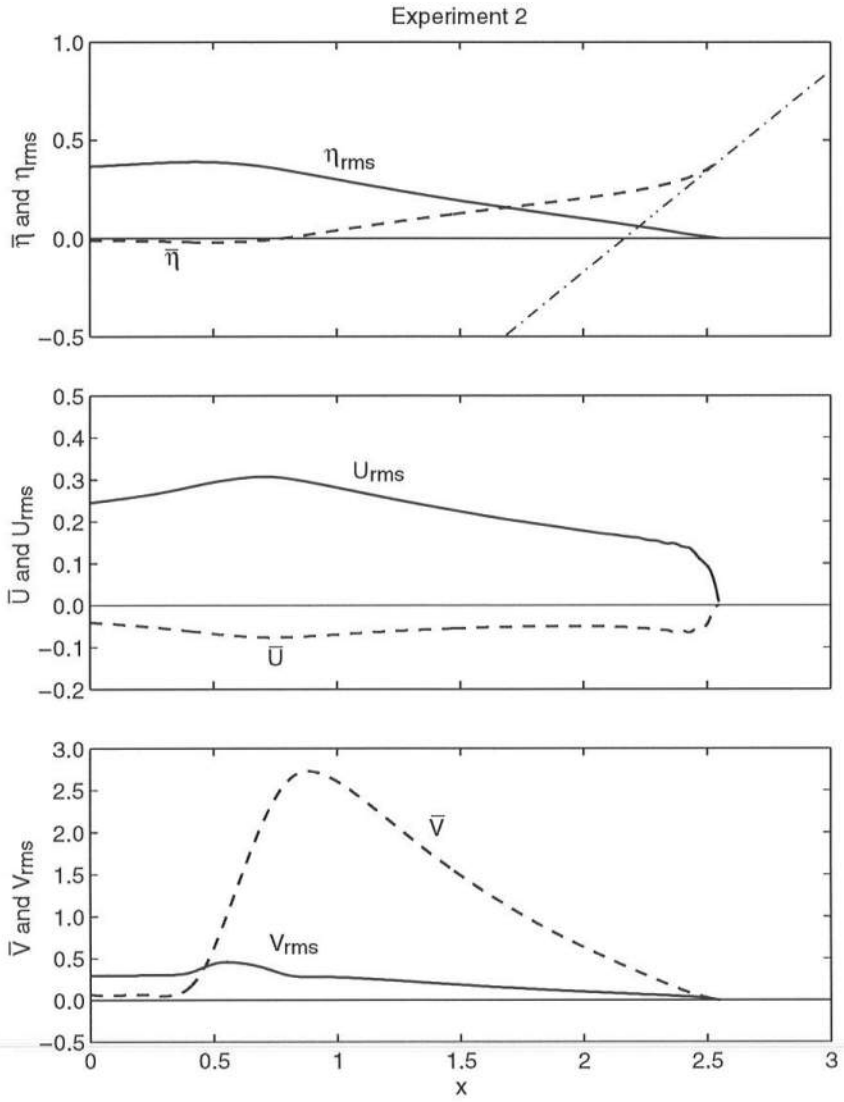

Figure 4.5: Cross-shore variations of $\overline{\eta}, \eta_{\text{rms}}, \overline{U}, U_{\text{rms}}, \overline{V}$, and V_{rms}.

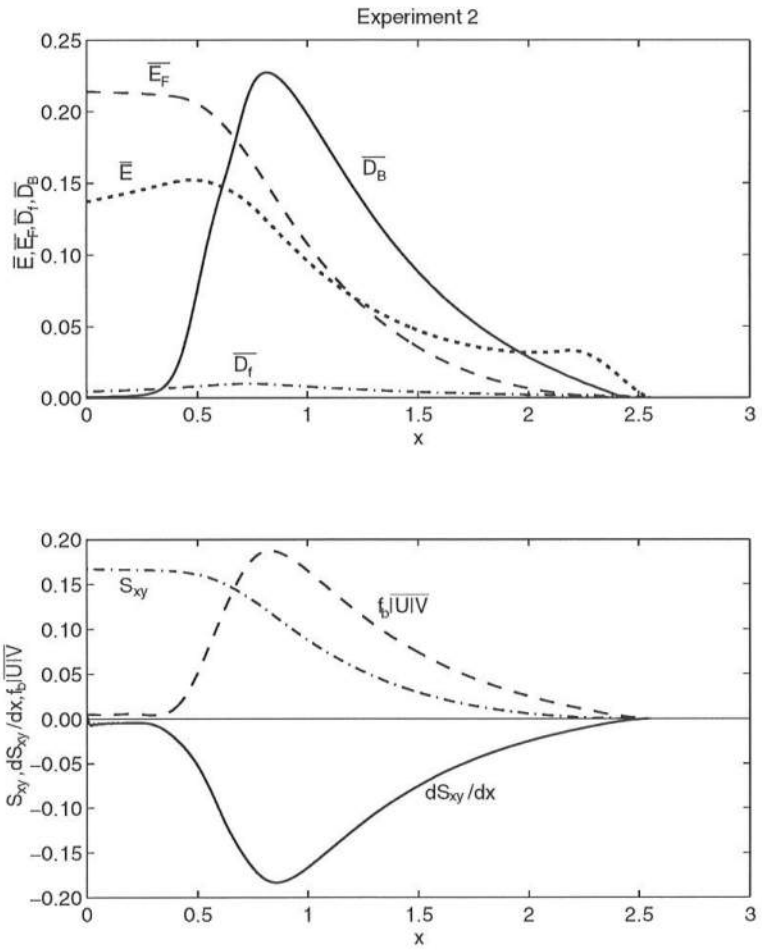

Figure 4.6: Time-averaged cross-shore wave energy and alongshore momentum balances.

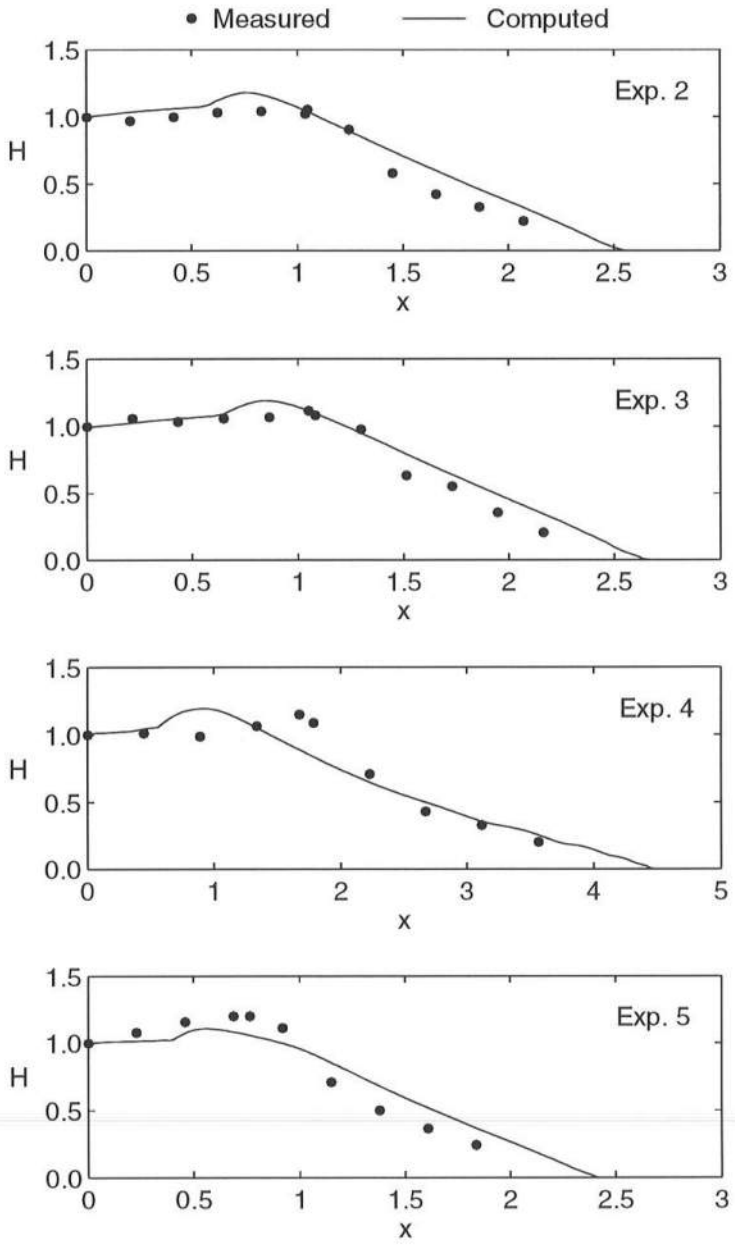

Figure 4.7: Measured and computed local wave height H for four experiments.

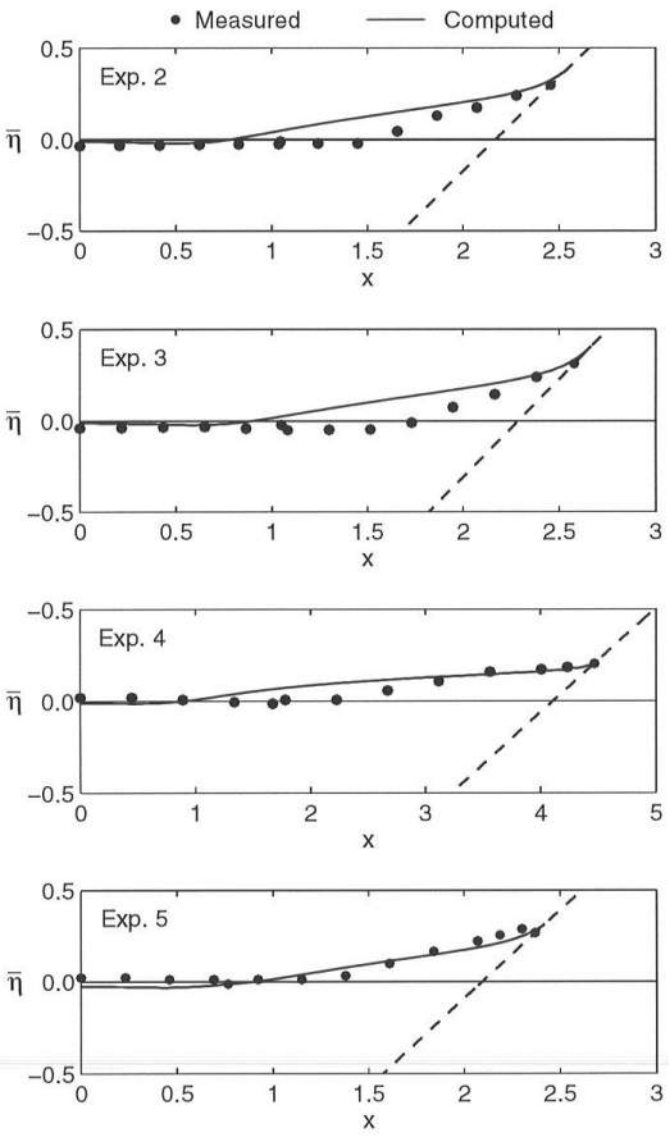

Figure 4.8: Measured and computed wave setup $\overline{\eta}$ for four experiments.

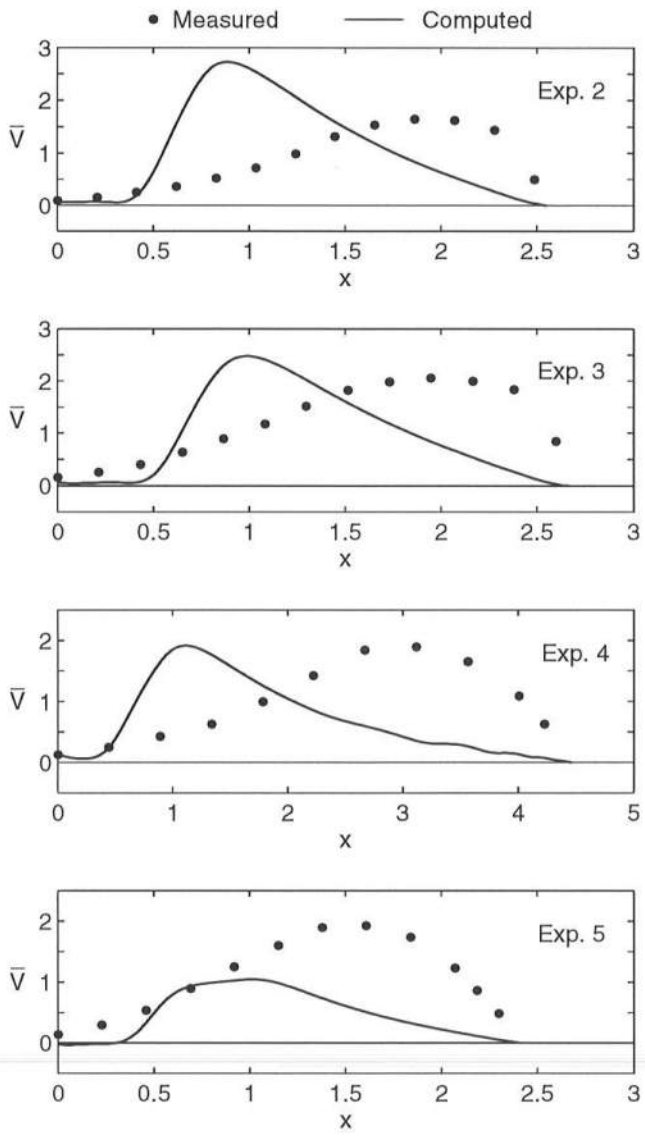

Figure 4.9: Measured and computed longshore current $\overline{V}$ for four experiments.

the similar agreement for experiments 2 and 3 whose incident wave conditions are listed in Table 4.1, it may be concluded that $\theta_c^2 = 0.206$ may still be regarded to be much less than unity. Visser (1984) and Nairn *et al.* (1990) showed it would be necessary to delay the initiation of the influence of energy dissipation on the generation of longshore currents until the landward limit of the transition zone. These shortcomings of the numerical model may be serious for longshore currents generated by regular waves but are much less apparent for irregular waves due to irregular wave breaking and generation of low-frequency motions as can be seen in the comparison with the field data of Thornton and Guza (1986) in the next section.

Finally, Figure 4.10 indicates that the computed longshore current is not sensitive to the values of $(\Delta y/\Delta x)$ used in the computation as long as Δy is on the order of Δx where $\Delta y \simeq \Delta x$ has been used unless stated otherwise.

4.3 Comparison with Field Data

The 2D numerical model is also compared with field data to verify whether the numerical model is applicable to natural beaches as well. The numerical model is compared herein with the field experiments conducted by Thornton and Guza (1986, 1989) at Leadbetter beach in February 1980. The mean nearshore slope $\tan\theta'_m$ varied between 0.03 and 0.06 during the experiment but no major bar was apparent. The incident waves were limited to a narrow window of approach because of the protection from a cape and islands. Comparison is made with the data of February 5 and 6 that included the bottom profiles, the incident wave frequency spectrum and representative angle of incidence in 3 m depth, and the cross-shore variations of the measured root-mean-square wave height and longshore current. The wave conditions and bottom contours near the shoreline could be reasonably assumed to be uniform in the alongshore direction.

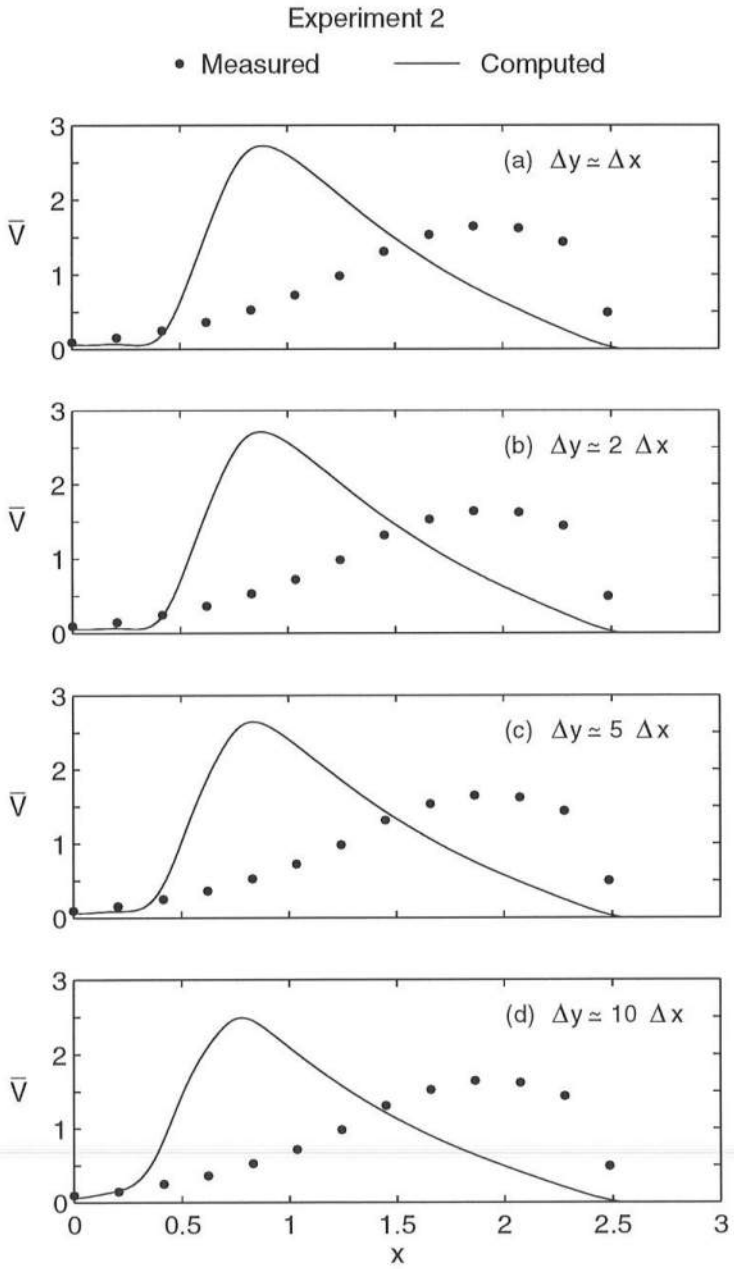

Figure 4.10: Sensitivity analysis for experiment 2 with (a) $\Delta y \simeq \Delta x$, (b) $\Delta y \simeq 2\Delta x$, (c) $\Delta y \simeq 5\Delta x$, (d) $\Delta y \simeq 10\Delta x$.

4.3.1 Input Parameters

The measured incident wave frequency spectra in the 3 m water depth on February 5 and 6 presented by Thornton and Guza (1986) included only the sea-swell band of frequencies (0.05–0.3 Hz). As a result, the incident wave train η_i' computed using (4.4) does not include the incident low-frequency wave components. The spectral peak period T_p', the root-mean-square wave height $H_{\rm rms}'$, and the representative incident wave angle θ_i at the seaward boundary in the depth $d_t' = 3$ m are summarized in Table 4.3. The assumption of random phases in (4.4) is not really valid in shallow water due to nonlinear phase coupling (*e.g.*, Elgar and Guza 1986). The computed results presented in the following will need to be interpreted in light of these limitations of (4.4).

The computed results presented in the following are based on the normalization using $H' = H_{\rm rms}'$, $T' = T_p'$ and $\theta_c = \theta_i$ in radians at the 3 m depth. The parameter σ defined in (2.6) is hence given by

$$\sigma = T_p' \left(\frac{g}{H_{\rm rms}'} \right)^{1/2}$$

The values of σ and θ_c listed in Table 4.3 suggest that the assumptions of shallow water waves with small angles of incidence are appropriate for these data sets.

Table 4.3: Incident wave at seaward boundary $d' = 3$ m.

Date	$\tan\theta_m'$	d_t' (m)	T_p' (s)	$H_{\rm rms}'$ (m)	θ_i (deg)	σ	θ_c^2	ξ
Feb 5	0.035	3.0	12.8	0.49	7.8	57	0.0196	0.80
Feb 6	0.033	3.0	11.1	0.28	7.5	66	0.0169	0.87

The number of cross-shore lines in the finite difference grid shown in Figure 3.1 is taken as $I = 3$ since the beach and incident wave conditions are assumed to be uniform in the longshore direction. The bottom profiles along the three cross-shore lines are assumed to be the same and taken as the measured bottom profiles

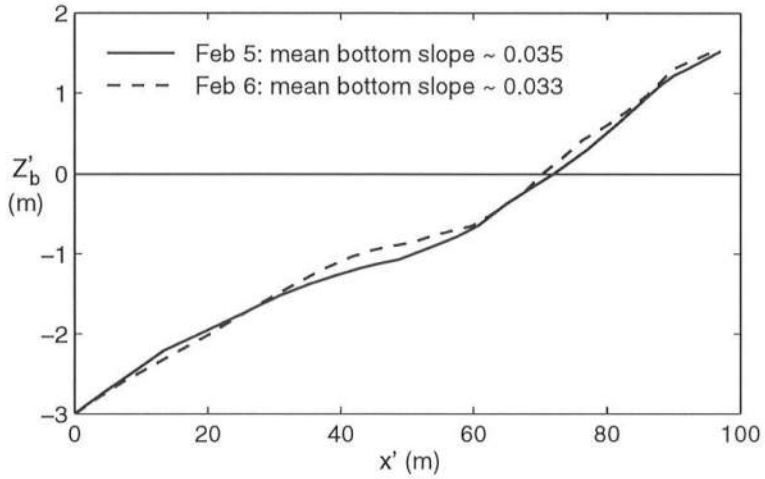

Figure 4.11: Measured bottom profiles for February 5 and 6.

on February 5 and 6. The mean bottom slope, $\tan\theta'_m$, between the shoreline and the mean breaker line was 0.035 and 0.033 on February 5 and 6, respectively, as listed in Table 4.3. The actual bottom profiles shown in Figure 4.11 are used for the following computations. Plunging breakers were most often observed. The surf similarity parameter defined as $\xi = \sigma \tan\theta'_m/(2\pi)^{1/2}$ was $\xi = 0.80$ and 0.87 on February 5 and 6.

The dimensional cross-shore grid spacing is taken as $\Delta x' = 0.180$ m on February 5 with $H'_{\rm rms} = 0.49$ m and $\Delta x' = 0.135$ m on February 6 with $H'_{\rm rms} = 0.28$ m in order to resolve steep wave fronts. The normalized grid spacing Δx is about 0.007 on both days. The number of grid spacings between the 3 m depth and the still water shoreline is 400 and 520 on February 5 and 6, respectively. The dimensional alongshore grid spacing is taken as $\Delta y' = 1.32$ and 1.03 m on February 5 and 6, respectively, so that the normalized grid spacings Δx and Δy are approximately the same.

The normalized computation duration, $t_{\rm max} = t'_{\rm max}/T'_p$, is taken as $t_{\rm max} = 500$. Correspondingly, $t'_{\rm max} = 107$ and 93 min on February 5 and 6, respectively. The

computation duration $t'_{\min}$ exceeds the sampling duration of 68 min employed by Thornton and Guza (1986) to account for the transient duration of the computation initiated from no wave action at $t = 0$.

The incident wave train $\eta'_i(t', y')$ computed at $y' = 0$, $\Delta y'$ and $2\Delta y'$ using (4.4) is normalized as $\eta_i = \eta'_i / H'_{\rm rms}$ with $t = t'/T'_p$. The sampling rate $\Delta t'_s$ associated with N in (4.4) was taken to be 0.5 sec. The normalized sampling rate Δt_s must be small enough to resolve the temporal variation of η_i but is normally much larger than the finite difference time step Δt required by the numerical stability criterion. The time step Δt used for the actual computation is about 0.0002 and much smaller than the sampling rate to minimize spurious shoreline oscillations as will be explained later in the discussion of the computation results for alongshore velocity. A simple linear interpolation of η_i sampled at the rate Δt_s is performed to find the value of η_i at the time level $t^* = (t + \Delta t)$ during the time-marching computation. The values of η_i at $t = 0$ is set to zero for $y' > 0$ since (4.5) does not ensure $\eta'_i = 0$ at $t' = 0$ and $y' > 0$. The effect of these adjustment to the specified spectrum is extremely small. Figure 4.12 shows the normalized incident wave trains η_i at $y = 0, \Delta y$ and $2\Delta y$ which satisfy the initial condition $\eta_i = 0$ at time $t = 0$, and $\partial \eta_i / \partial t > 0$ for small time t.

The only empirical parameter involved in the numerical model is the bottom friction factor f'_b in (3.4). Use is made of $f'_b = 0.015$ which was the value calibrated by Raubenheimer *et al.* (1995) using runup measurements on the fine-grained, gently sloping Scripps beach. The Leadbetter beach is composed of fine to medium size sand. Thornton and Guza (1986) calibrated the friction factor C_f for their longshore current model using the measured longshore currents on the Leadbetter beach. The two friction factors are related by $C_f = 0.5 f'_b$, assuming that the bottom friction factor for the present time-dependent model and their time-averaged model for longshore current are the same. Their calibrated value of $C_f \simeq 0.006$ turns

out to be very consistent with $f_b' \simeq 0.015$ based on the runup measurements by Raubenheimer *et al.* (1995).

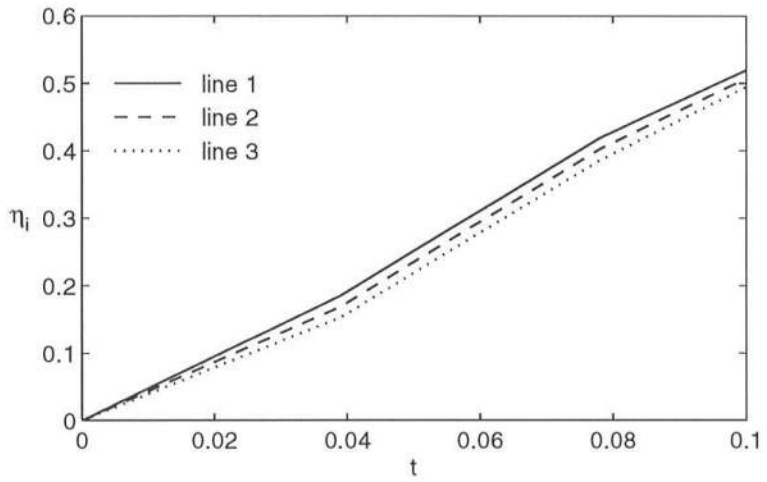

Figure 4.12: Initial portions of adjusted incident random wave trains η_i at $y = 0$ (line 1), Δy (line 2), $2\Delta y$ (line 3).

Figure 4.13 shows the measured and normalized incident wave frequency spectrum $S_i(f)$ for February 5 and 6 corresponding to the incident wave train $\eta_i(t, y)$ at $x = 0$ and at $y = 0$, Δy and $2\Delta y$ specified as input to the numerical model, where the dimensional frequency f' is normalized as $f = f'T_p'$ and the peak of $S_i(f)$ is located at $f = 1$. The spectra $S_i(f)$ at $y = 0$, Δy and $2\Delta y$ are identical because of the assumption of alongshore uniformity of the incident wave conditions. The specified spectra $S_i(f)$ do not include any low-frequency component where Thornton and Guza (1986) used $f' = 0.05$ Hz as a cutoff frequency. The normalized reflected wave trains $\eta_r(t, y)$ at $x = 0$ and at $y = 0$, Δy and $2\Delta y$ are computed when h and U are computed using (3.12) and (3.13) (Kobayashi *et al.* 1989). The corresponding reflected wave spectra are computed to be essentially identical and are also shown in Figure 4.13 which present the smoothed spectra $S_r(f)$ with 64 degrees of freedom.

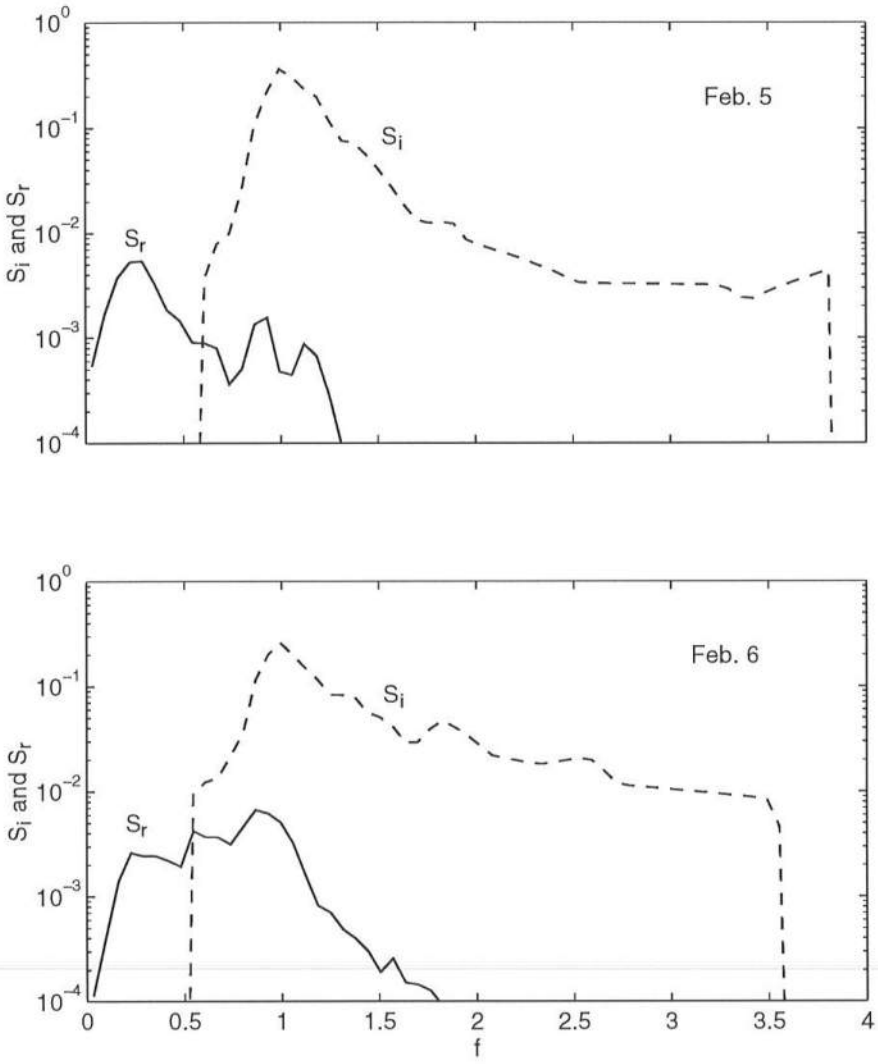

Figure 4.13: Specified incident wave spectrum S_i and computed reflected wave spectrum S_r for February 5 and 6.

The computed reflected wave spectra $S_r(f)$, especially for February 5, are dominated by the low-frequency wave components. The cross spectra among $\eta_r(t, y)$ at $y = 0$, Δy and $2\Delta y$ are also computed. The computed coherence squared is nearly unity, and the computed phase difference is almost zero because of the very small value of $\Delta y \simeq 0.007$ used in the computation. The reflected wave direction may become discernible if the number of cross-shore lines and the value of Δy are increased.

4.3.2 Computed Time Series

The computed temporal and cross-shore variations of η, U and V at $y = \Delta y$ only are used because of the assumed alongshore uniformity. Figures 4.14, 4.15, and 4.16 show the computed temporal variations of the free surface elevation η above SWL, the depth-averaged cross-shore velocity U and the depth-averaged alongshore velocity V, respectively, at $x = 0$ (in the 3 m depth), $x = 1.28$ (in the breaker zone), $x = 1.92$ (in the inner surf zone), $x = 2.56$ (near the still water shoreline), and $x = 2.81$ (above the still water shoreline) for February 5 while Figures 4.19, 4.20, and 4.21 show the computed temporal variations of η, U, and V at $x = 0$ (in the 3 m depth), $x = 1.98$ (in the breaker zone), $x = 3.08$ (in the inner surf zone), $x = 3.82$ (near the still water shoreline), and $x = 3.93$ (above the still water shoreline) for February 6. These figures are explained after some of the details associated with the numerical method are discussed below.

Figure 4.17 shows that the computed alongshore fluid motions without the numerical damping term D_j given by (3.38), where the numerical damping coefficient ϵ_ℓ is set to be zero, are practically the same as those computed using $\epsilon_\ell = 1$ except for the slight modifications of the high-frequency components. Computation is also made by reversing the spatial differencing in the predictor and corrector equations (3.35) and (3.36). Figure 4.18 shows that the computed results are indistinguishable, implying that the MacCormack method adopted in Section 3.1.2

should be applicable to wave fronts propagating seaward as well as landward.

Figures 4.14 and 4.19 and Figures 4.15 and 4.20 indicate that the transient duration of η and U computed using (3.12) and (3.13) with no wave action at $t = 0$ is short as has been the case with the computed results for regular waves shown in Figures 4.2 and 4.3. On the other hand, Figures 4.16 and 4.21 show that the transient duration of V computed using (3.34) is long near the breaker zone and inner surf zone where the longshore current develops very slowly. The slow response of the alongshore fluid motion for irregular waves is qualitatively similar to that in Figure 4.4 for regular waves. The oscillatory components of η in Figures 4.14 decrease landward where the lower limit of η at $x = 2.56$ and 2.81 is limited by the bottom elevation. On the other hand, the oscillatory components of U and V in Figures 4.15 and 4.16 increase landward and become the maximum near the still water shoreline. The comparison of the oscillatory components of η, U and V at $x = 2.81$ above the still water shoreline indicates that the fluid velocities U and V oscillate much more than the water depth h in the swash zone where h equals the free surface elevation η above the bottom elevation. The results for February 6 are also similar as depicted in Figures 4.19, 4.20, and 4.21.

For the computation for February 6, it is found that the value of Δt smaller than that required by the numerical stability criterion is necessary to minimize spurious shoreline oscillations. The computed temporal variations of alongshore velocity V using $\Delta t \simeq 0.0007$ plotted in Figures 4.22 and 4.23 show sudden jumps which originate at the shoreline and propagate in the seaward direction. The shoreline oscillations along the three cross-shore lines depicted in Figure 4.24 confirms that the sudden jumps are caused by spurious large shoreline differences lasting for a short duration. The use of Δt equal to one half of 0.0007 reduces the jumps but does not eliminate the problem completely as can be seen in Figure 4.25. Therefore, the computation is repeated with $\Delta t \simeq 0.0002$ and the numerical algorithm dealing with

the moving shoreline is improved somewhat to minimize spurious shoreline oscillations. This problem was not apparent in the previous one-dimensional cross-shore computations because their effects on the cross-shore fluid motion were limited to the swash zone and lasted only for a short duration. The computed results for η and U using these three different values of Δt remain essentially the same. As a result, the computations for both February 5 and 6 presented in this chapter are based on $\Delta t \simeq 0.0002$ with no apparent unrealistic shoreline oscillation.

4.3.3 Computed Spectra

The computed alongshore velocities V in the region of the slow longshore current development in Figures 4.16 and 4.21 exhibit very slow oscillations which will be elaborated in the following. The computed temporal variations of η, U and V for the duration $200 \leq t \leq 500$ are used in the following spectral and statistical calculations to account for the slow development of the alongshore velocity V. Admittedly, the time-dependent model is not efficient computationally for the alongshore fluid motion because of its slow response and dominant longshore current.

Figures 4.26, 4.27, and 4.28 show the smoothed frequency spectra of η, U, and V with 64 degrees of freedom for February 5 that correspond to the time series of η, U, and V for $200 \leq t \leq 500$ shown in Figures 4.14, 4.15, and 4.16, respectively. The noticeable low-frequency ($f < 0.64$ corresponding to $f' = 0.05$ Hz) wave components near the shoreline are expected from the previous field measurements (*e.g.*, Guza and Thornton, 1982; Holman and Sallenger, 1985) and will be discussed further at the end of this section. Figure 4.28 clearly shows the very low frequency component of V at $x = 1.28$ (in the breaker zone) and 1.92 (in the inner surf zone) corresponding to the very slow oscillations of V in Figure 4.16. The corresponding very low frequency components of η and U at $x = 1.28$ and 1.92 are absent or extremely small in Figures 4.26 and 4.27.

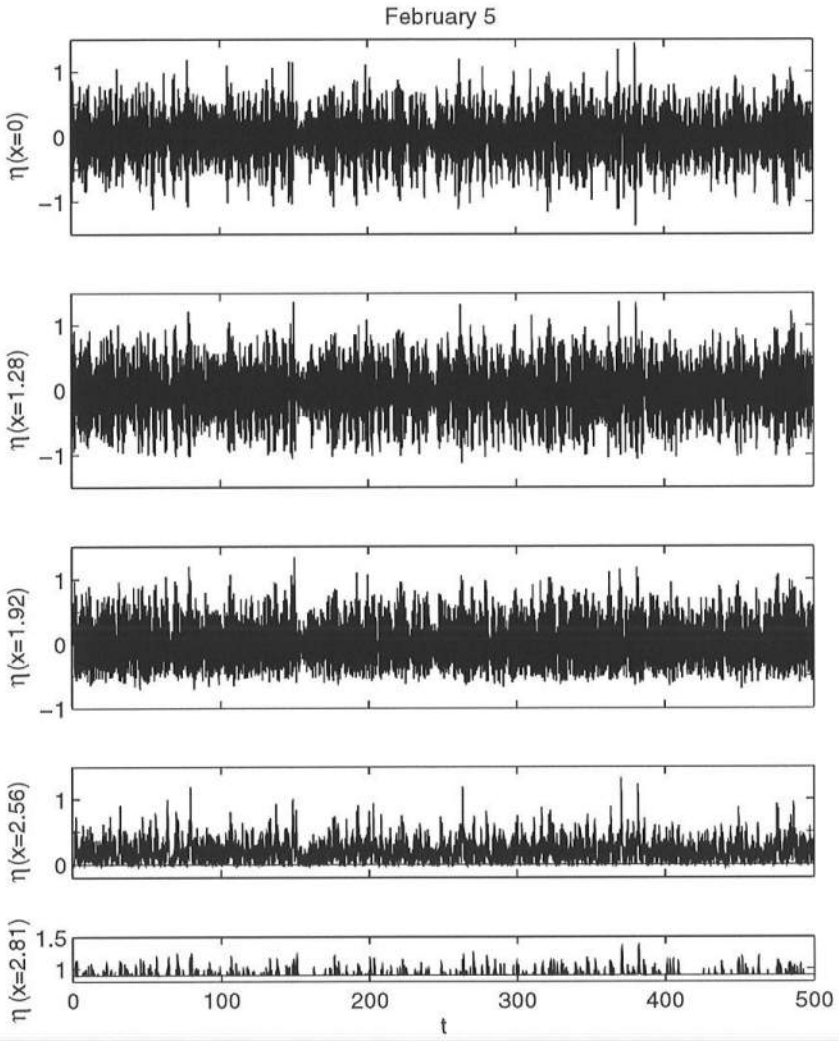

Figure 4.14: Computed temporal variations of free surface elevation η at $x = 0$, 1.28, 1.92, 2.56 and 2.81 for February 5.

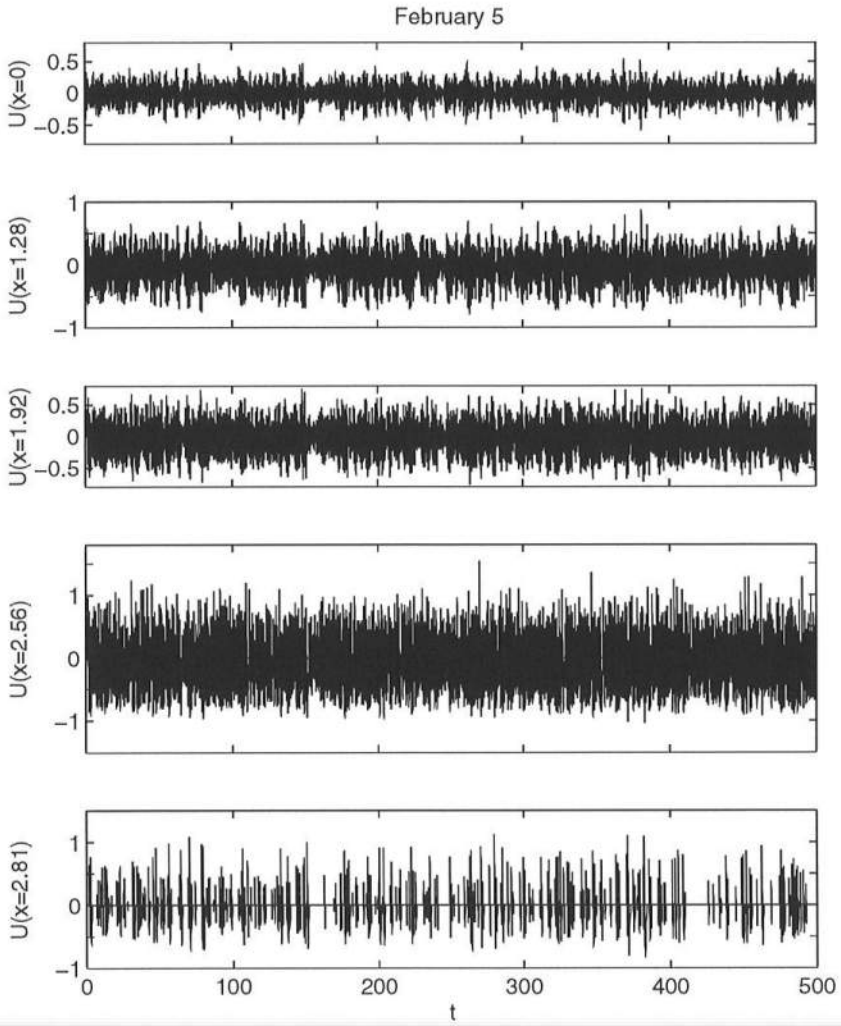

Figure 4.15: Computed temporal variations of depth-averaged cross-shore velocity U at $x = 0$, 1.28, 1.92, 2.56 and 2.81 for February 5.

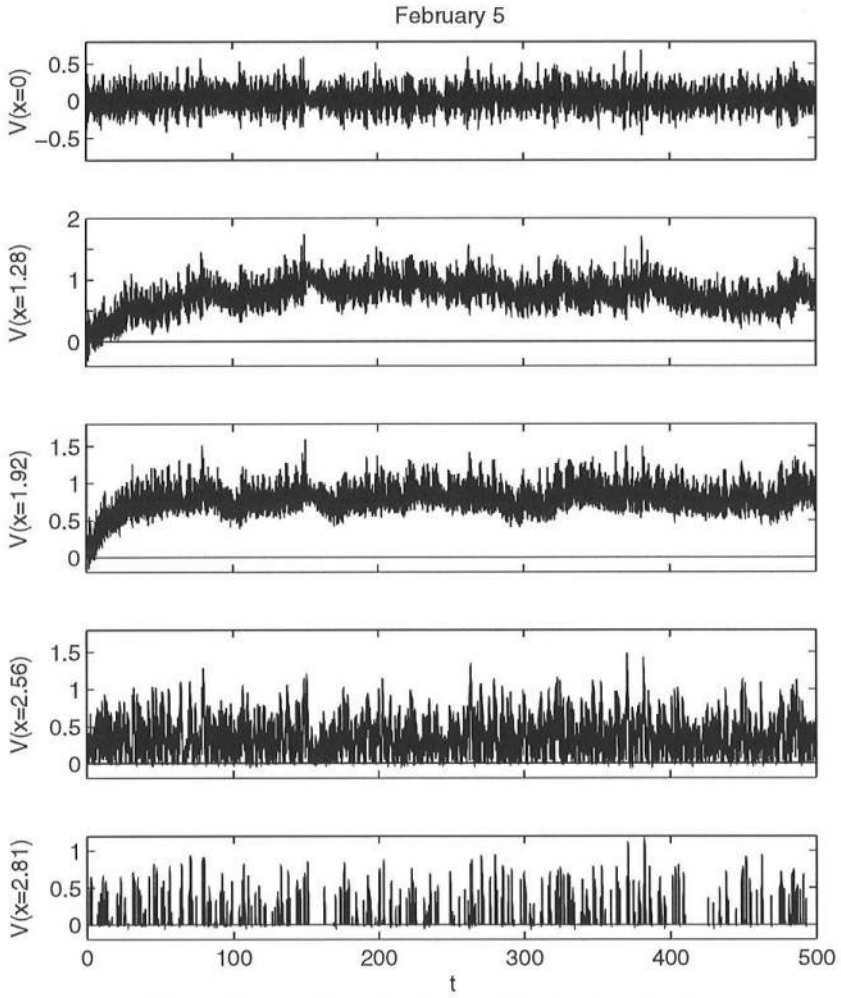

Figure 4.16: Computed temporal variations of depth-averaged alongshore velocity V at $x = 0$, 1.28, 1.92, 2.56 and 2.81 for February 5.

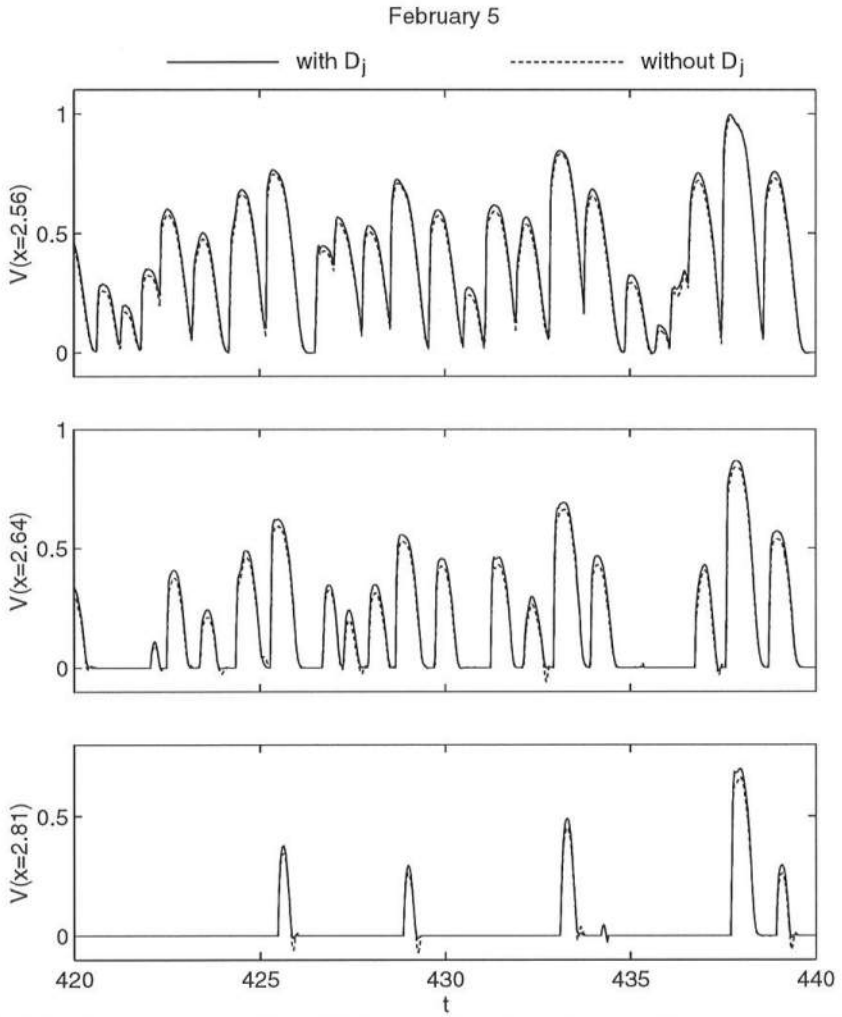

Figure 4.17: Comparison of computed temporal variations of depth-averaged alongshore velocity V at $x = 2.56$, 2.64 and 2.81 for February 5 with and without damping term D_j for t=420–440.

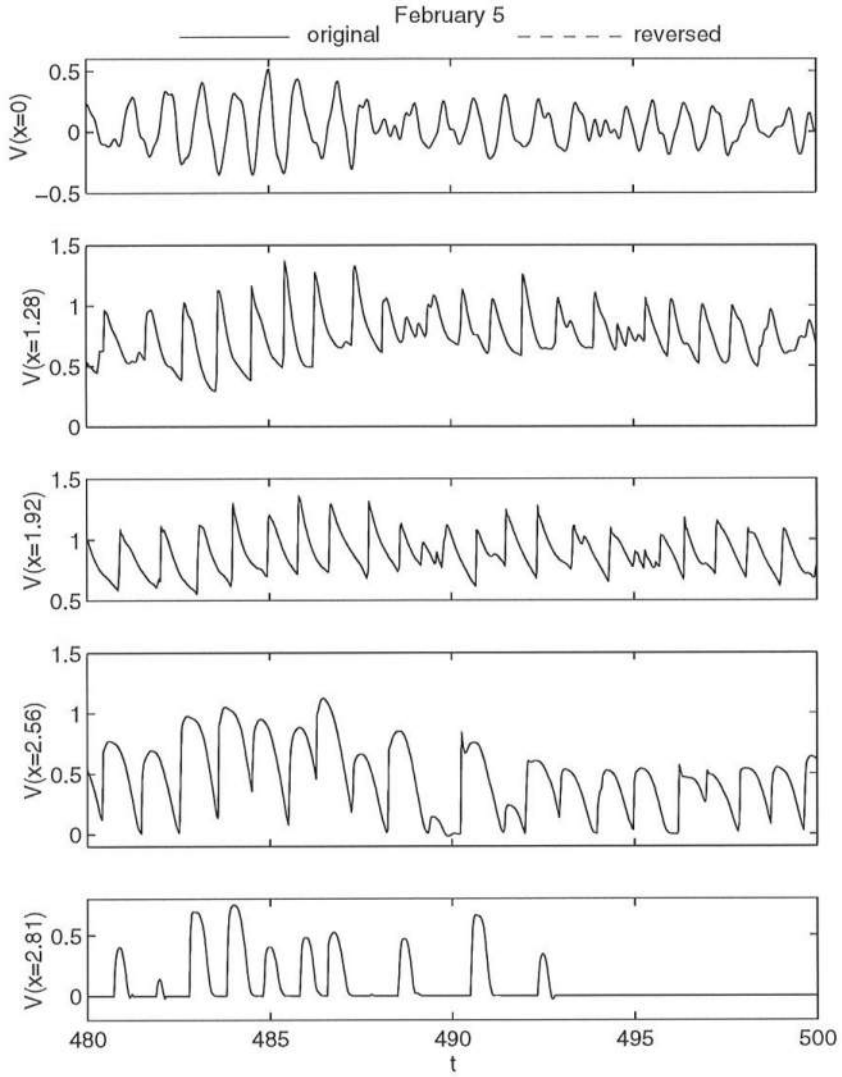

Figure 4.18: Comparison of computed temporal variations of depth-averaged alongshore velocity V at $x = 0$, 1.28, 1.92, 2.56 and 2.81 for February 5 using original scheme and by reversing the spatial differencing in predictor and corrector equations of MacCormack method for t=480–500.

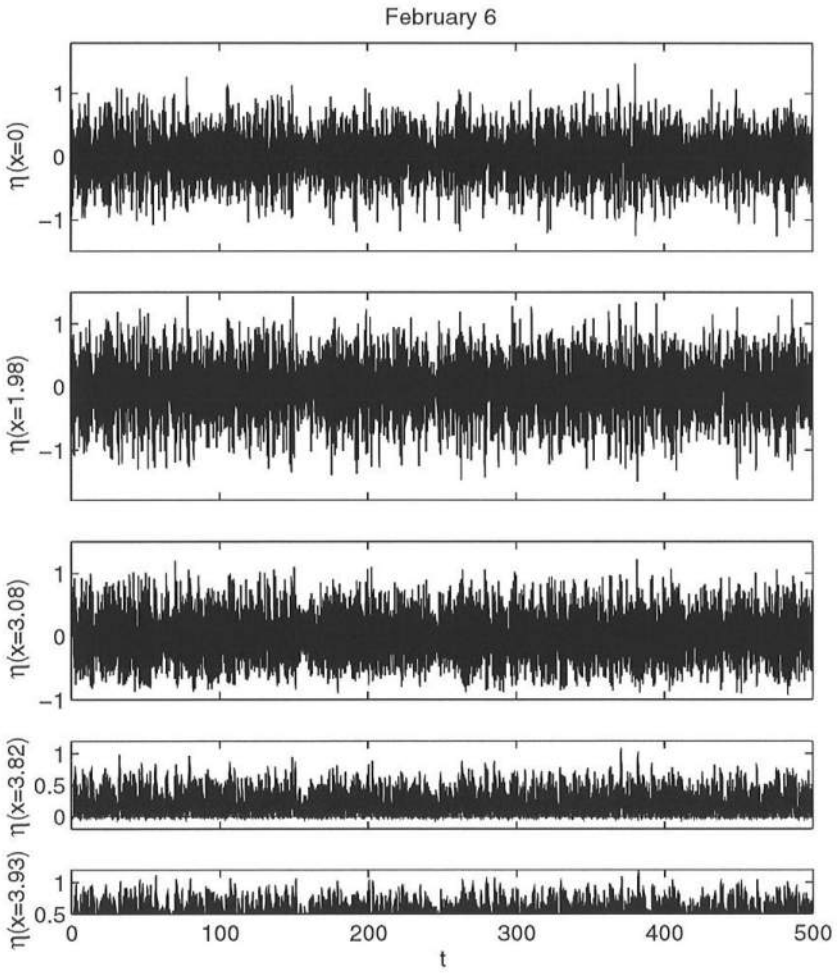

Figure 4.19: Computed temporal variations of free surface elevation η at $x = 0$, 1.98, 3.06, 3.82 and 3.93 for February 6.

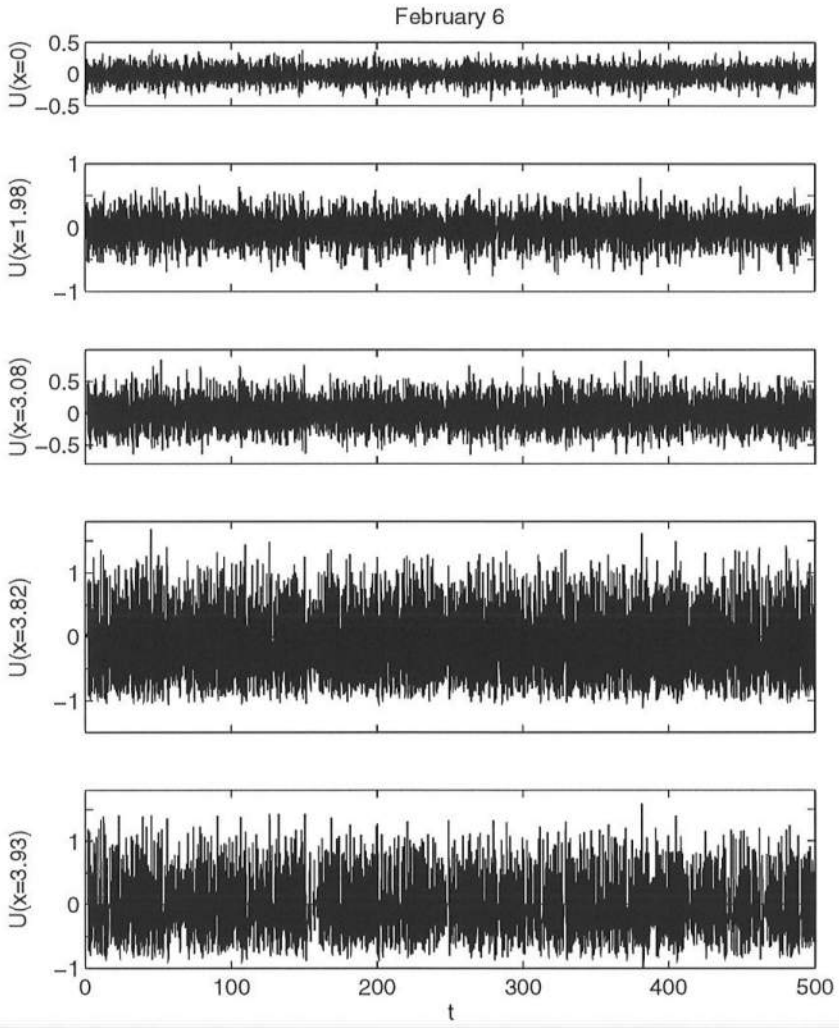

Figure 4.20: Computed temporal variations of depth-averaged cross-shore velocity U at $x = 0$, 1.98, 3.08, 3.82 and 3.93 for February 6.

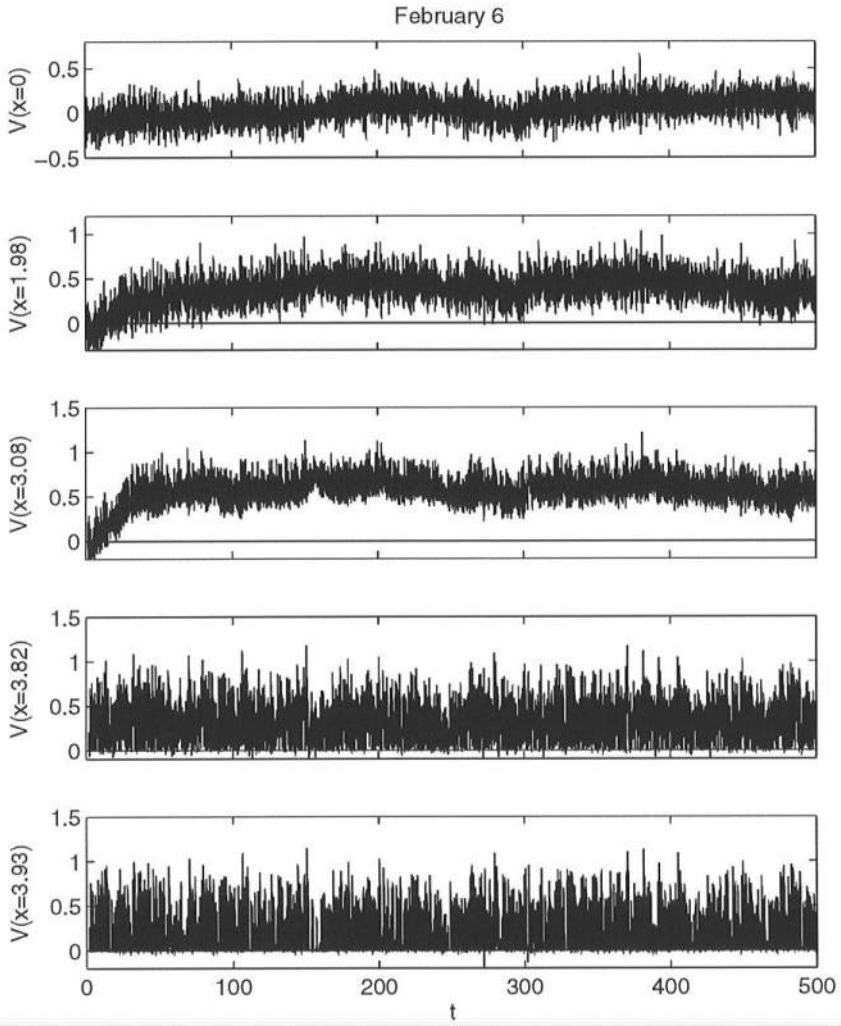

Figure 4.21: Computed temporal variations of depth-averaged alongshore velocity V at $x = 0$, 1.98, 3.08, 3.82 and 3.93 for February 6.

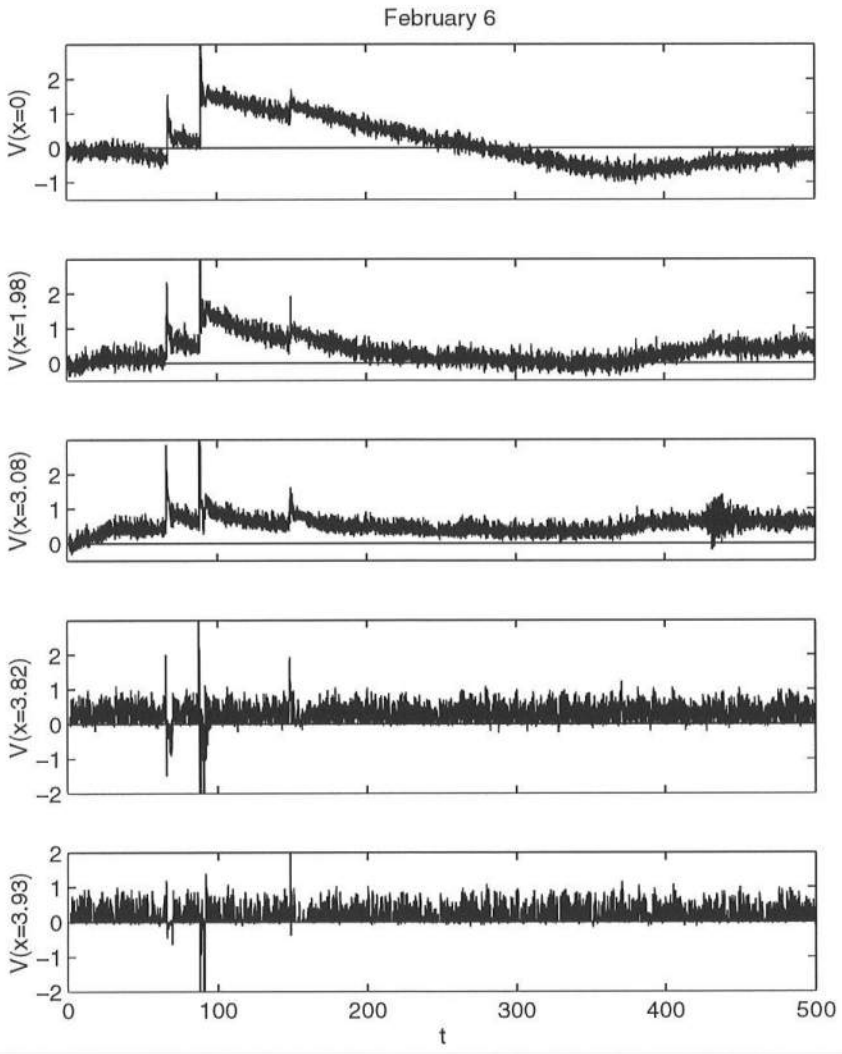

Figure 4.22: Computed temporal variations with sudden jumps of depth-averaged alongshore velocity V at $x = 0$, 1.98, 3.08, 3.82 and 3.93 for February 6 with $\Delta t \simeq 0.0007$.

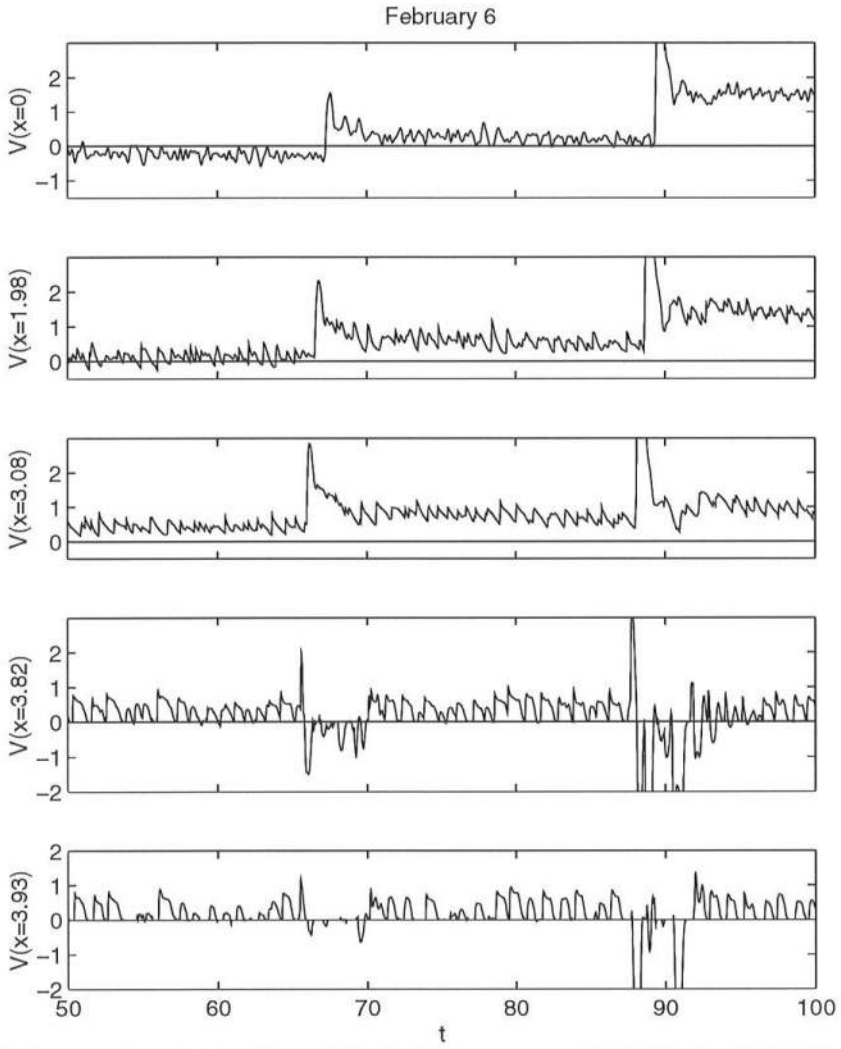

Figure 4.23: Computed temporal variations with sudden jumps of depth-averaged alongshore velocity V at $x = 0$, 1.98, 3.08, 3.82 and 3.93 for February 6 with $\Delta t \simeq 0.0007$ plotted from $t = 50$ to $t = 100$.

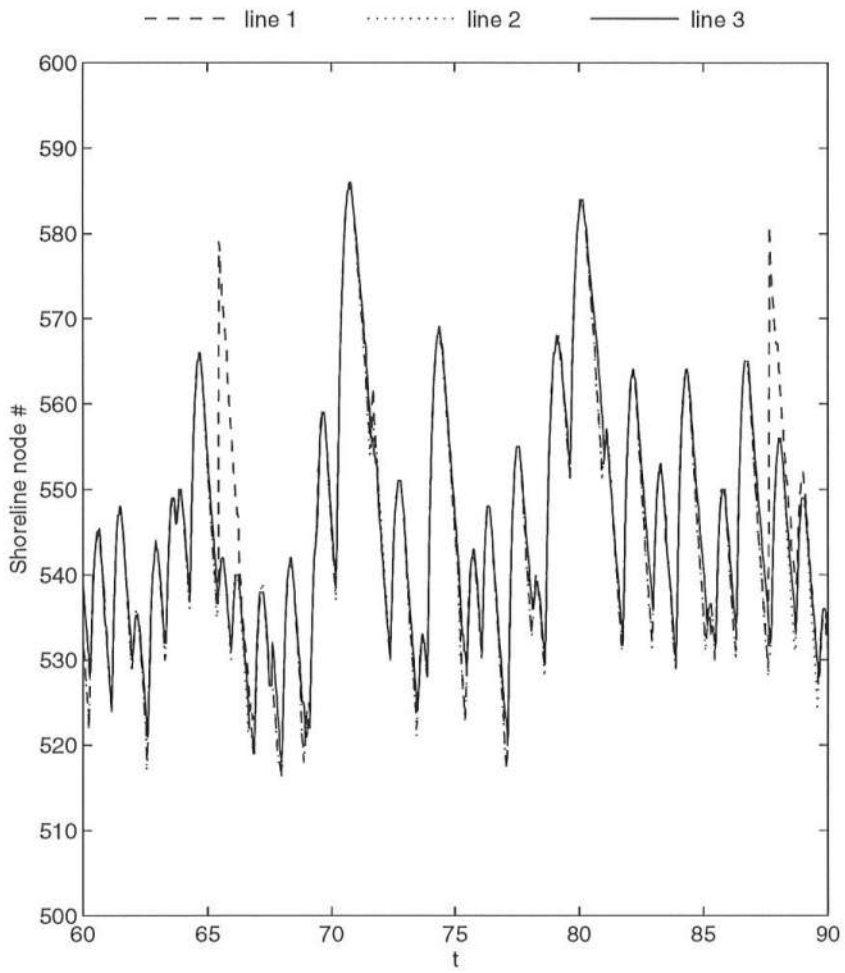

Figure 4.24: Shoreline oscillations at three cross-shore lines for February 6 with $\Delta t \simeq 0.0007$.

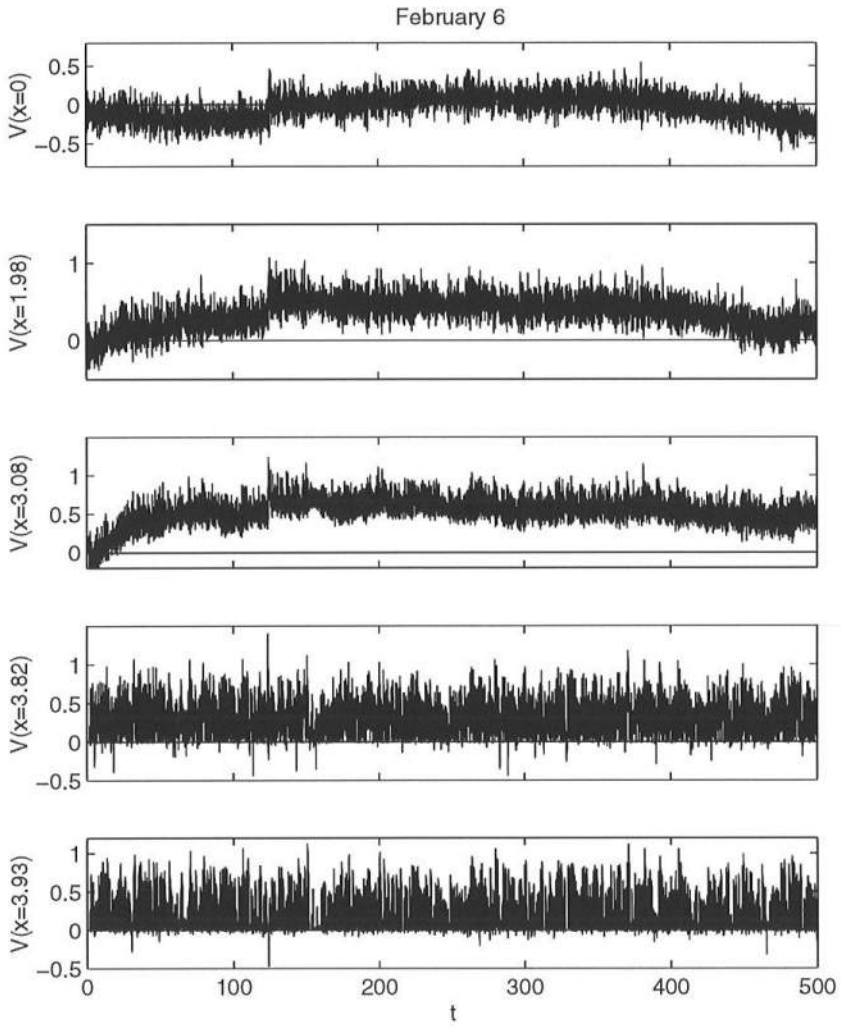

Figure 4.25: Computed temporal variations with reduced jumps of depth-averaged alongshore velocity V at $x = 0$, 1.98, 3.08, 3.82 and 3.93 for February 6 with $\Delta t \simeq 0.00035$.

To infer the likely origin of the very low frequency component of V, the corresponding spectra of $\partial\eta/\partial y, q_\ell U$, and $|U|V$ are plotted in Figures 4.29, 4.30, and 4.31, respectively. The alongshore free surface gradient $\partial\eta/\partial y$ in the approximate alongshore momentum equation (3.34) or (3.42) drives the alongshore wave motion in this simplified numerical model. The alongshore momentum flux, $hUV = q_\ell U$ in (3.34) affects the alongshore fluid motion through the nonlinear interaction of h, U, and V, where h is the sum of η and the still water depth. The alongshore bottom stress $f_b|U|V$ in (3.34) reduces the alongshore fluid motion, where the normalized bottom friction factor defined in (3.4) is $f_b = 0.43$ on February 5. Figure 4.29 indicates the considerably very low frequency component of $\partial\eta/\partial y$ at $x = 1.28$ and 1.92 which does not vary much with the normalized frequency f. Comparing Figures 4.27 and 4.30, the spectral shapes of U and $q_\ell U$ at $x = 1.28, 1.92$, and 2.56 are similar in the region where the mean $\overline{q}_\ell$ is a significant portion of q_ℓ. The temporal variations of q_ℓ are similar to those of V shown in Figure 4.16. The cross-shore variation of $\overline{q}_\ell$ will be presented later in relation to that of the longshore current $\overline{V}$. Comparison of Figures 4.28 and 4.31 indicates that the spectral shapes of V and $|U|V$ are similar except near the shoreline where the spectra of $|U|V$ contain more higher-frequency ($f \gtrsim 1.5$) components, probably due to the nonlinear interaction of $|U|$ and V.

To examine whether the very low frequency component of $\partial\eta/\partial y$ in Figure 4.29 is capable of generating the very low frequency component of V shown in Figure 4.28, use is made of the linearized alongshore momentum equation corresponding to (3.42)

$$\frac{\partial V}{\partial t} \simeq -\frac{\partial \eta}{\partial y} \tag{4.8}$$

The temporal variation of V for $200 \leq t \leq 500$ is calculated by integrating (4.8) for the computed temporal variation of $\partial\eta/\partial y$ at given x corresponding to each spectrum shown in Figure 4.29. The initial value of V at $t = 200$ is taken as the

value of V at $t = 200$ computed using (3.34).

Figure 4.32 compares the spectrum of the temporal variation V at given x calculated using the linear equation (4.8) with the corresponding spectrum of V computed using the nonlinear equation (3.34) and shown in Figure 4.28. It is noted that the linear equation (4.8) amplifies the very low frequency component of V because (4.8) yields $|\hat{V}| = |A|/(2\pi f)$, where $\hat{V}$ and A are the complex amplitude of V and $\partial\eta/\partial y$ for given f, respectively. Figure 4.32 shows that the two spectra of V at $x = 0$ are essentially identical except for the very low frequency range. This indicates that the nonlinear terms in (3.34) are negligible at $x = 0$ as may also be inferred from the spectra of $q_\ell U$ and $|U|V$ at $x = 0$ shown in Figures 4.30 and 4.31. Figure 4.32 also indicates that the nonlinear terms in (3.34) reduce the spectra of V at $x = 1.28$ and 1.92, especially for the low-frequency range. On the other hand, the term $\partial\eta/\partial y$ in (3.34) and (3.42) is negligible relative to the nonlinear terms near the shoreline at $x = 2.56$ and 2.81 except for the very low frequency range. This is consistent with the significant decrease of the spectra of $\partial\eta/\partial y$ near the shoreline as shown in Figure 4.29.

Figure 4.32 suggests that the very low frequency component of $\partial\eta/\partial y$ is large enough to cause the corresponding very slow oscillations of V. However, the origin of this very low frequency component of $\partial\eta/\partial y$ is not certain. It has been mentioned that the earlier computations shown in Figures 4.22–4.25 exhibited infrequent sudden jumps in the computed temporal variations of V caused by the infrequent large differences of the shoreline location along the cross-shore lines 1 and 3. The central finite difference approximation of $\partial\eta/\partial y$ along the cross-shore line 2 using the computed values of η along the two adjacent cross-shore lines is sensitive to the spurious large shoreline difference lasting for a short duration. The final results presented herein are computed using the improved numerical algorithm dealing with the moving shoreline and using a smaller time step Δt as explained in relation to Figures 4.22–4.25. The computed shoreline oscillations along the three cross-shore

lines do not show any unrealistic shoreline location difference. The very low frequency component of the spectrum of $\partial\eta/\partial y$ at $x = 2.81$ shown in Figure 4.29 is indeed extremely small.

The very low frequency component of $\partial\eta/\partial y$ seems to be related to the breaking of obliquely incident random waves because the very low frequency components of $\partial\eta/\partial y$ and V tend to occur in the vicinity of the breaker zone as shown in Figures 4.16, 4.28, and 4.29. No very slow oscillations were found in the computed temporal variations of V for regular waves as shown in Figure 4.4. Cross-spectral analyses of V and $\partial\eta/\partial y$ do not indicate any cross-shore wave pattern in these very low frequency components. Since the present numerical model does not simulate wave breaking explicitly, the origin of the very low frequency component of $\partial\eta/\partial y$ can still be numerical.

4.3.4 Comparison with Measurements

Figure 4.33 shows the comparisons between the measured and computed cross-shore variations of the local root-mean-square wave height, $H_{\rm rms} = H'_{\rm rms}/H'$, on February 5 and 6. Thornton and Guza (1986) obtained $H'_{\rm rms}$ using a zero up-crossing method from 68 minutes free surface elevation records after band-pass filtering between 0.05 and 0.5 Hz. Accordingly, the computed temporal variation of η for $200 \leq t \leq 500$ is analyzed in the same way to obtain $H_{\rm rms}$ based on the zero up-crossing method. In addition, the computed spectral estimate of $H_{\rm rms} = (8m_o)^{1/2}$ is also presented in Figure 4.33 where m_o is the zero moment of the frequency spectrum of η after the band-pass filtering. The agreement between the data and the present time-dependent model is no better than that between the data and the time-averaged model of Thornton and Guza (1983) presented with their data except that the only empirical parameter involved in the time-dependent model is the bottom friction factor f'_b whose effect on the free surface elevation η is essentially limited in the swash zone (*e.g.*, Kobayashi and Wurjanto 1992).

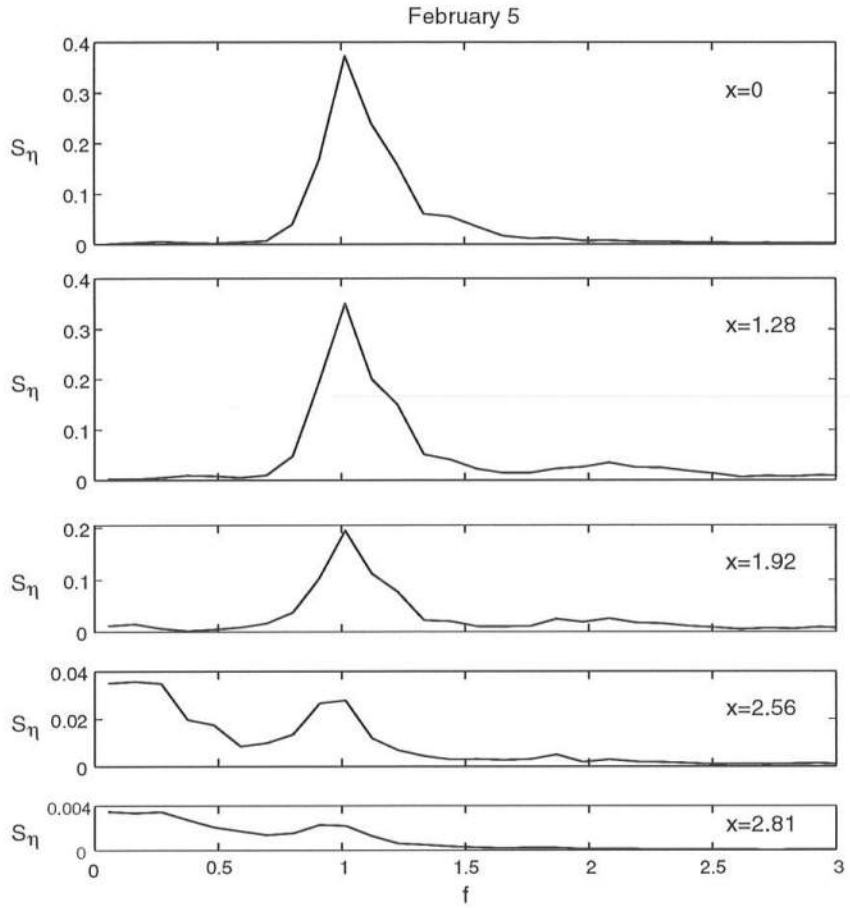

Figure 4.26: Computed frequency spectra of free surface elevation η at $x = 0, 1.28, 1.92, 2.56$, and 2.81 on February 5.

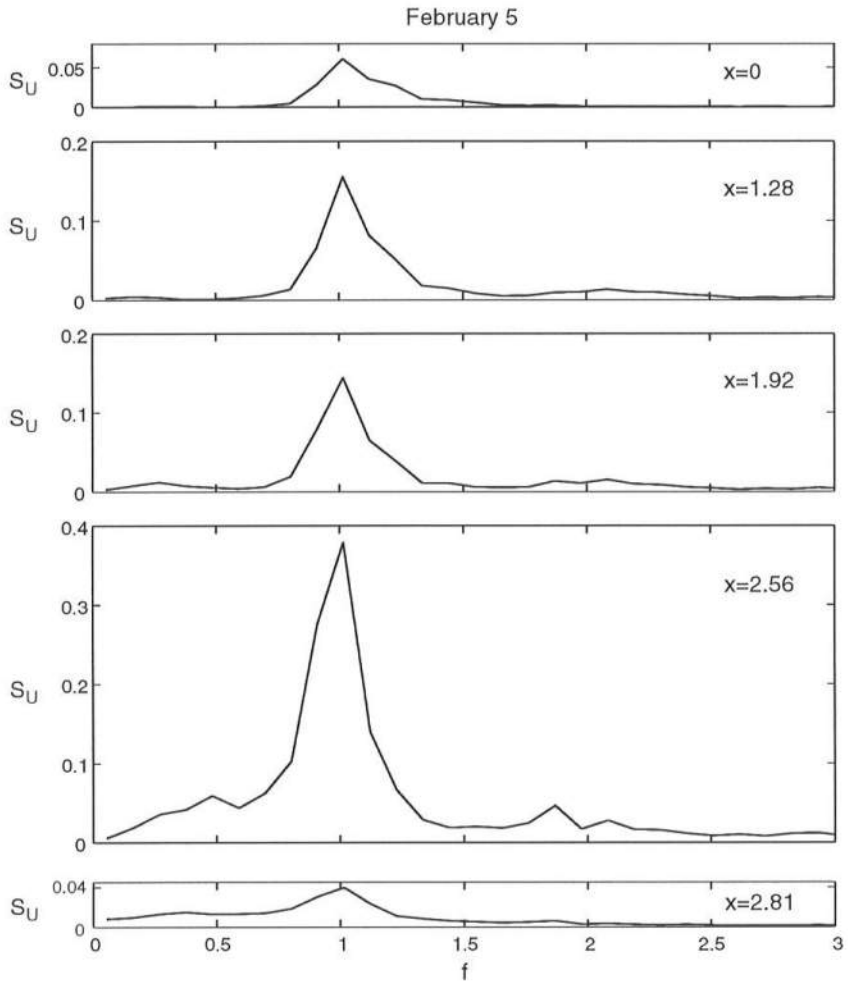

Figure 4.27: Computed frequency spectra of cross-shore velocity U at $x = 0, 1.28, 1.92, 2.56$, and 2.81 on February 5.

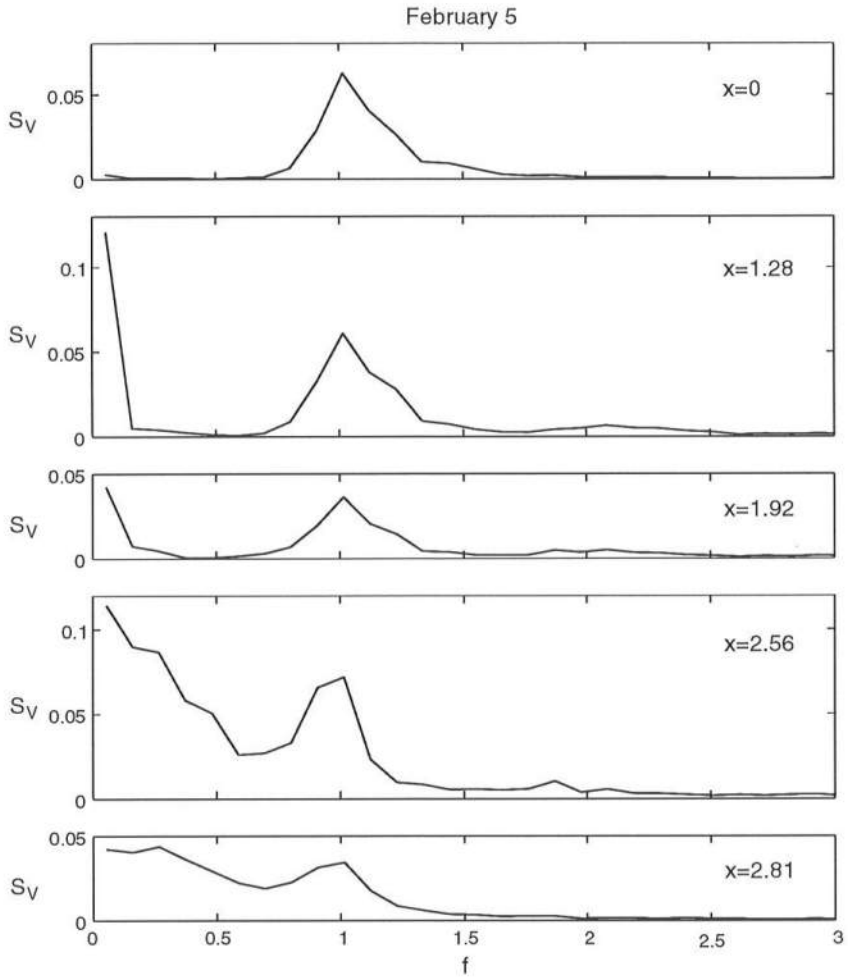

Figure 4.28: Computed frequency spectra of alongshore velocity V at $x = 0, 1.28, 1.92, 2.56$, and 2.81 on February 5.

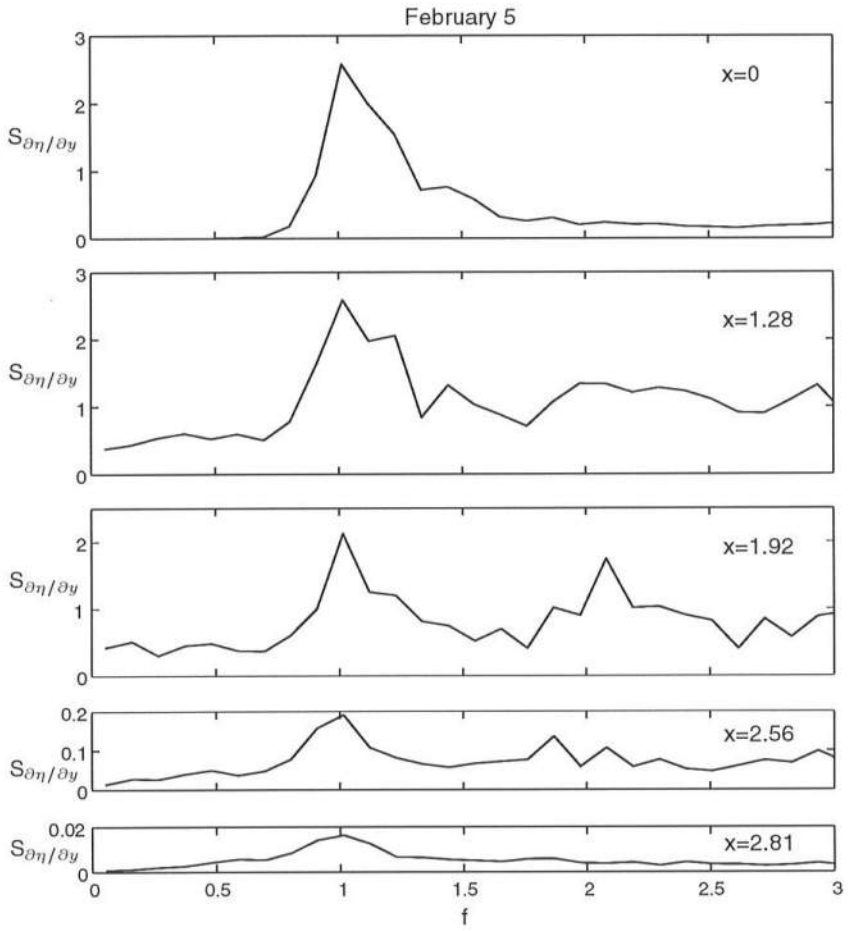

Figure 4.29: Computed frequency spectra of alongshore free surface gradient $\partial\eta/\partial y$ at $x = 0,\ 1.28,\ 1.92,\ 2.56$, and 2.81 on February 5.

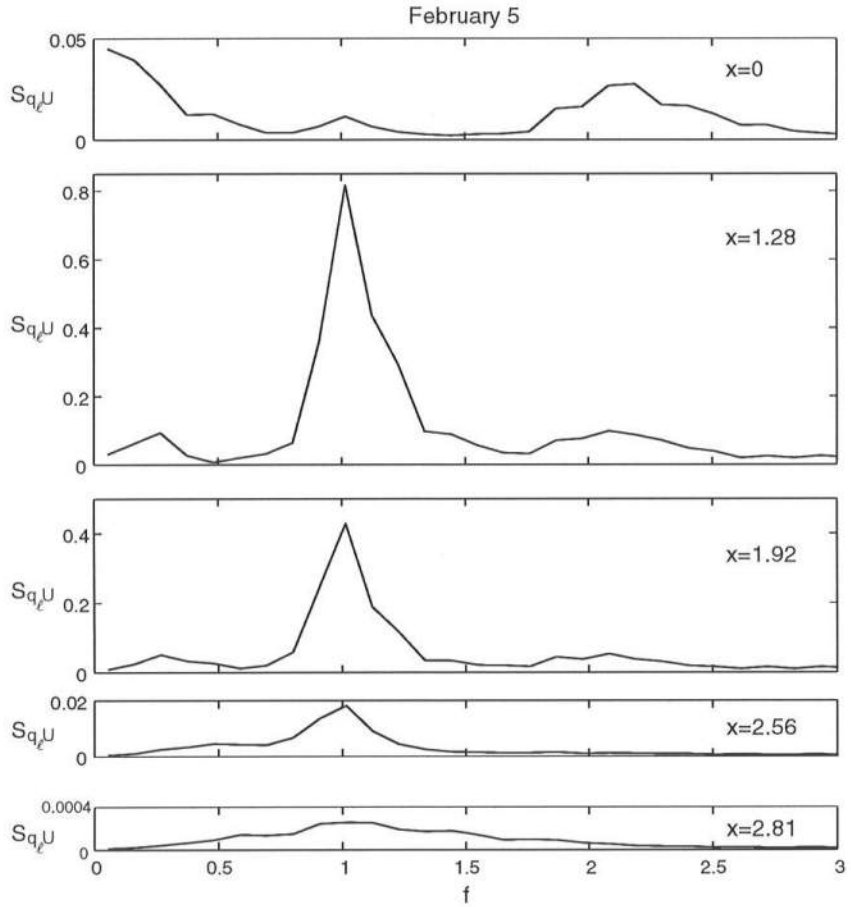

Figure 4.30: Computed frequency spectra of alongshore momentum flux, $hUV = q_\ell U$, at $x = 0,\ 1.28,\ 1.92,\ 2.56$, and 2.81 on February 5.

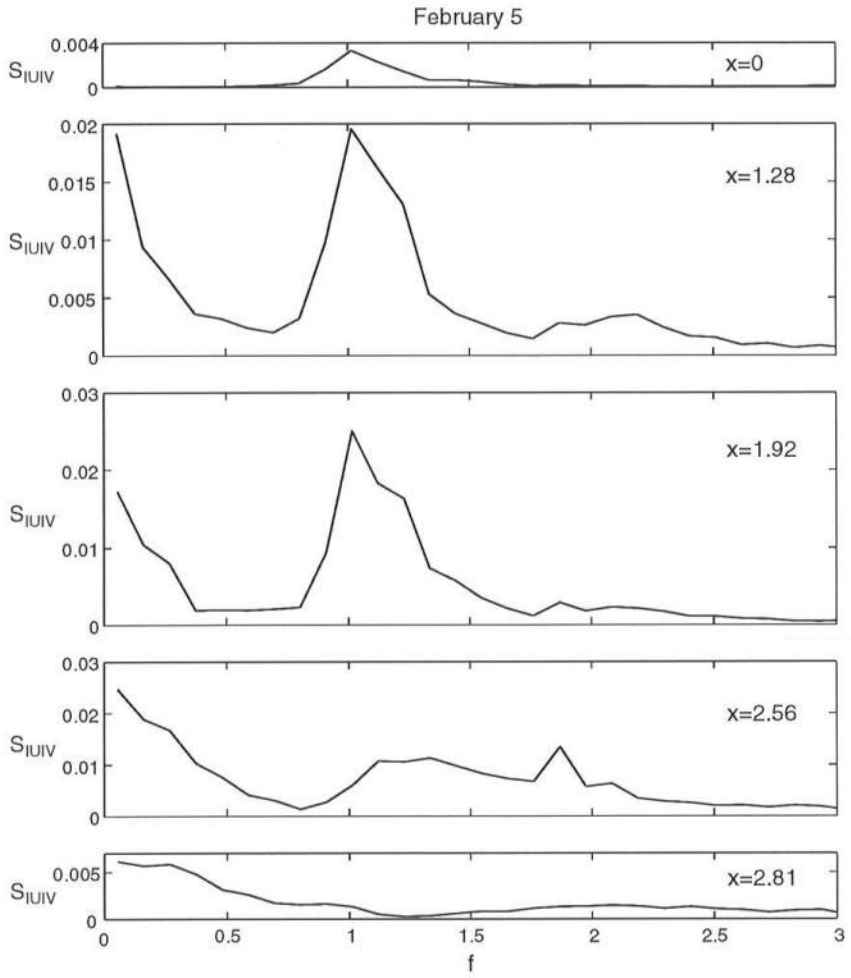

Figure 4.31: Computed frequency spectra of alongshore bottom shear stress $|U|V$ with $f_b = 0.43$ at $x = 0,\ 1.28,\ 1.92,\ 2.56$, and 2.81 on February 5.

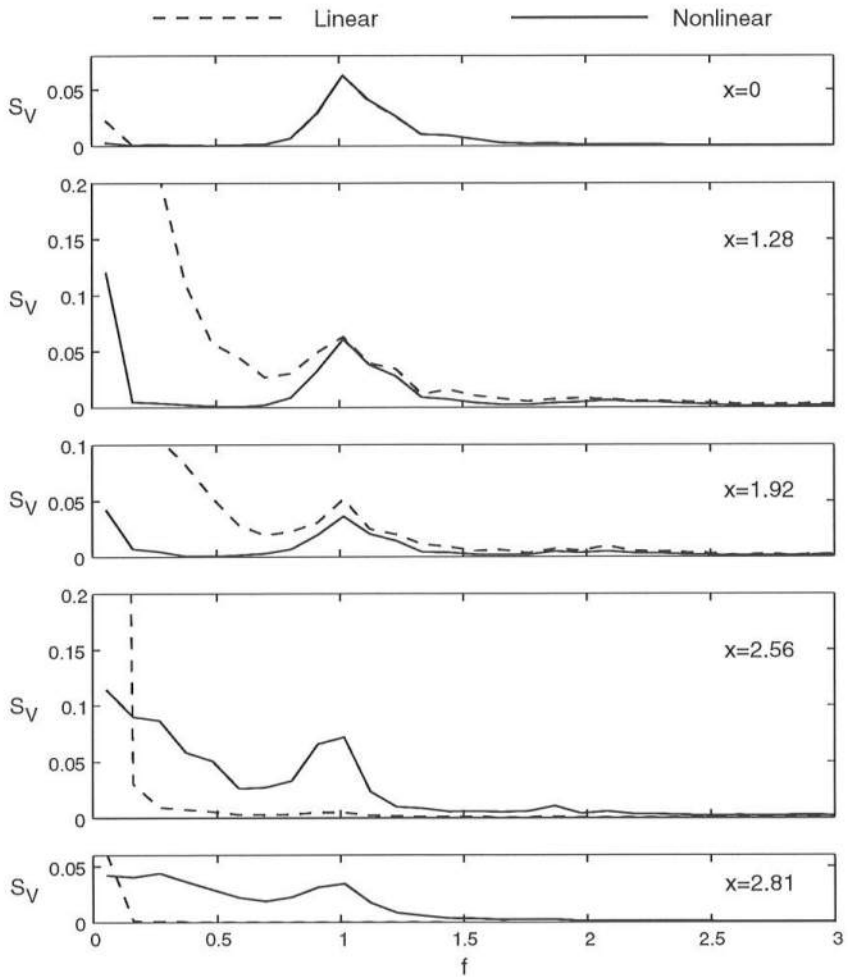

Figure 4.32: Computed frequency spectra of alongshore velocity V at $x = 0, 1.28, 1.92, 2.56$, and 2.81 on February 5 using linear (dashed curves) equation (4.8) and nonlinear (solid curves) equation (3.34).

Figure 4.34 compares the measured and computed cross-shore variations of the longshore current $\overline{V}$ on February 5 and 6 where the overbar denotes the time averaging for $200 \leq t \leq 500$. The computed maximum and minimum alongshore velocities, $V_{\max}$ and $V_{\min}$, during $200 \leq t \leq 500$ are also plotted in Figure 4.34 to show that the alongshore velocity V is oscillatory (positive and negative) outside the surf zone and essentially unidirectional (mostly positive) in the surf zone where the temporal variations of V at five different locations in cross-shore direction have been shown in Figures 4.16 and 4.21. The time-dependent model with the bottom friction factor $f_b' = 0.015$ calibrated by Raubenheimer *et al.* (1995) using runup measurements on a natural beach also predicts the longshore current reasonably well. This suggests the robustness of the adopted empirical formula for bottom friction, (2.46) and (2.47), although it may be too crude to predict the detailed temporal variation of the bottom shear stress accurately. Thornton and Guza (1986) compared their time-averaged model with the longshore current data and obtained similar agreement. No data is available in the swash zone to compare the accuracy of the time-averaged and time-dependent models.

4.3.5 Computed Time-Averaged Quantities

Figure 4.35 shows the computed cross-shore variations of the alongshore radiation stress S_{xy} given by (3.6), its cross-shore gradient, and the time-averaged alongshore bottom shear stress $f_b\overline{|U|V}$ in the time-averaged alongshore momentum equation (3.5). The alongshore variations of the computed mean and variance of η are found to be negligible in (3.5) relative to the other two terms shown in Figure 4.35. It is noted that for this 2D model, the alongshore momentum flux correction $n = 0$. The assumption of alongshore uniformity requires that the computed mean and variance of η at $y = 0$, Δy and $2\Delta y$ should be identical. Figure 4.35 show that the computed time-dependent results satisfy the time-averaged force balance

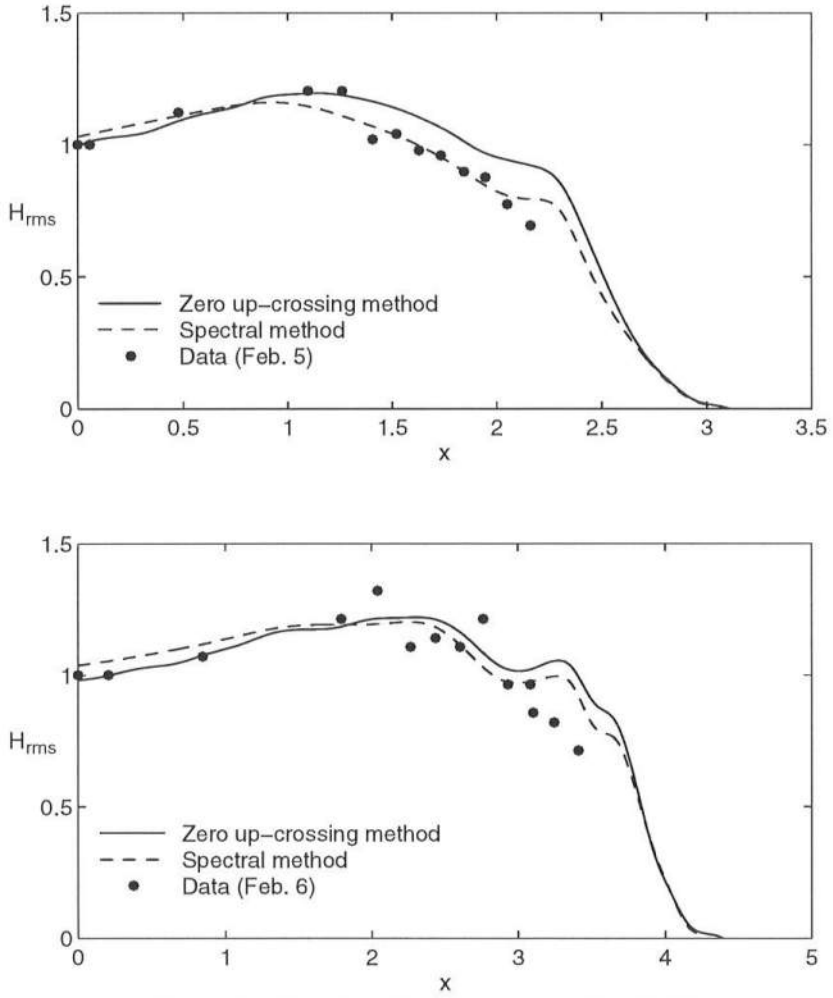

Figure 4.33: Comparisons between measured and computed root-mean-square wave height H_{rms} on February 5 and 6.

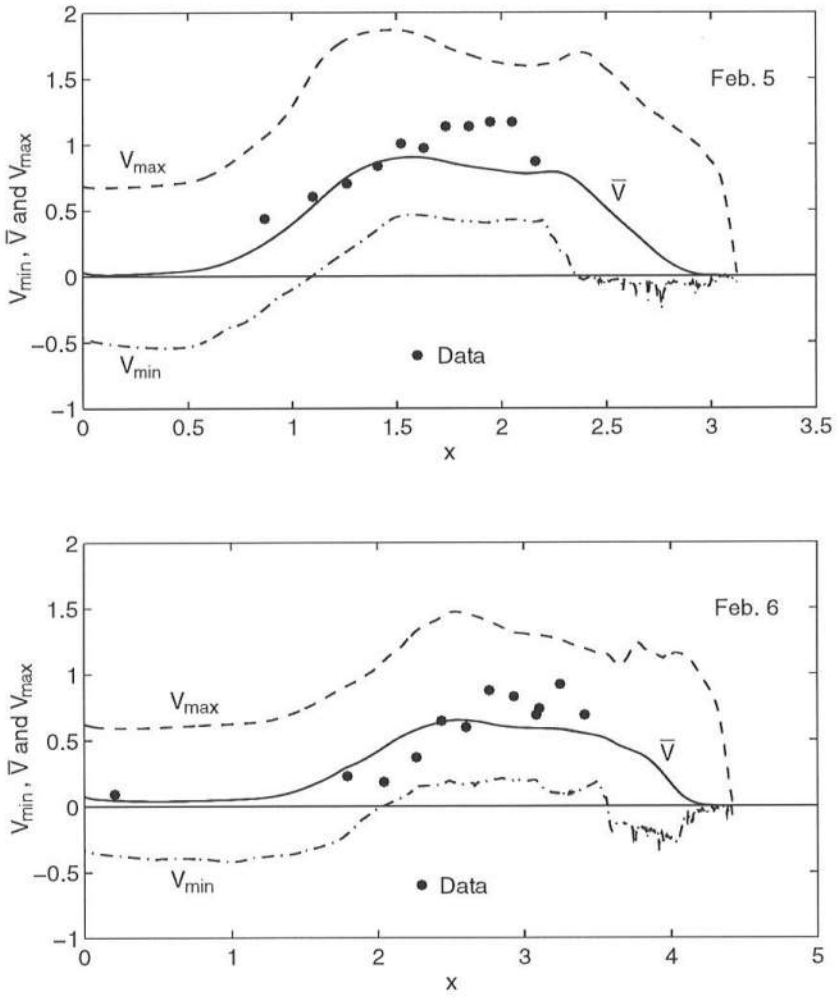

Figure 4.34: Comparisons between measured and computed longshore current $\overline{V}$ together with computed maximum and minimum alongshore velocities, $V_{\max}$ and $V_{\min}$, on February 5 and 6.

between the cross-shore gradient of S_{xy} and the alongshore bottom shear stress apart from the high-frequency numerical oscillations of dS_{xy}/dx. The minute oscillations of S_{xy} caused by the high frequency numerical oscillations of the computed h, U, and V are almost indiscernible in Figure 4.35 but are significantly amplified in the cross-shore derivative of S_{xy} approximated by a central finite difference. The alongshore bottom shear stress shown in Figure 4.35 is the maximum near the still water shoreline as may be expected from U and V shown in Figures 4.15, 4.20, 4.16 and 4.21. Figure 4.35 also indicates that the numerical dispersion of the time-dependent model is negligible in the time-averaged alongshore momentum equation (3.5) which includes no physical dispersion or lateral mixing term. Thornton and Guza (1986) already showed that the lateral mixing was not important for their longshore current data.

Figure 4.36 shows the computed cross-shore variations of $\overline{q}_\ell = \overline{hV}$ and $\overline{h}\,\overline{V}$. The time-averaged alongshore volume flux $\overline{q}_\ell$ per unit width can be expressed as

$$\overline{q}_\ell = \overline{h}\,\overline{V} + \overline{(h-\overline{h})(V-\overline{V})} \tag{4.9}$$

where the second term on the right-hand side of (4.9) is the time-averaged alongshore volume flux component due to the oscillatory components $(h-\overline{h})$ and $(V-\overline{V})$. Figure 4.36 indicates that this component in (4.9) is small in comparison to the product of the mean water depth $\overline{h}$ and the longshore current $\overline{V}$ except for the regions of small $\overline{h}$ in the swash zone and small $\overline{V}$ outside the surf zone.

To examine the nature of large fluid velocities near the still water shoreline, Figures 4.37 and 4.38 show the computed cross-shore variations of the mean values $\overline{\eta}$, $\overline{U}$ and $\overline{V}$ as well as the root-mean-square values of the oscillatory components $(\eta-\overline{\eta})$, $(U-\overline{U})$ and $(V-\overline{V})$ denoted by the subscript rms where $\eta_{\rm rms}$, $U_{\rm rms}$ and $V_{\rm rms}$ are the standard deviations of η, U and V, respectively. The normalized bottom elevation is indicated by the dotted line in the top panel of Figures 4.37 and 4.38.

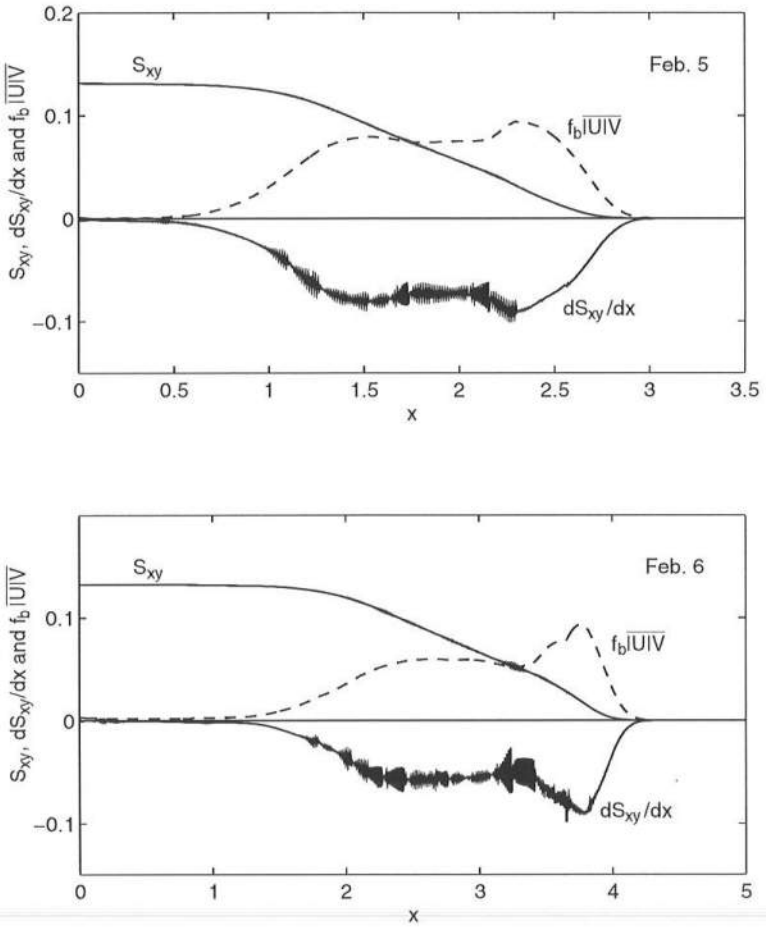

Figure 4.35: Computed cross-shore variations of alongshore radiation stress S_{xy}, its gradient and time-averaged alongshore bottom shear stress for February 5 and 6.

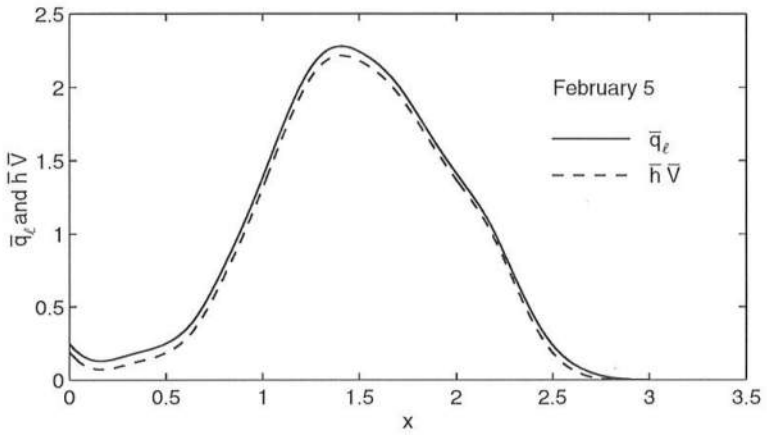

Figure 4.36: Computed cross-shore variations of mean alongshore volume flux $\overline{q_\ell} = \overline{hV}$ and product of mean depth $\overline{h}$ and longshore current $\overline{V}$ on February 5.

The wave setup $\overline{\eta}$ becomes tangential to the beach in the swash zone (Bowen *et al.* 1968). The mean cross-shore velocity $\overline{U}$ is negative and represents the cross-shore return current as explained by Kobayashi *et al.* (1989). Unlike the computed results for regular waves shown in Figure 4.5, $\eta_{\rm rms}$ does not decrease linearly landward, while $U_{\rm rms}$ and $V_{\rm rms}$ actually increase landward before their decrease in the swash zone. For lack of velocity data near the still water shoreline, the computed cross-shore variations of $U_{\rm rms}$ and $V_{\rm rms}$ can not be verified, whereas the cross-shore one-dimensional model has been shown to predict the free surface elevation η in the inner surf and swash zones fairly accurately (Cox *et al.* 1994; Raubenheimer *et al.* 1995). The field data obtained at Torrey Pines Beach, California by Guza and Thornton (1985) indicated that the variance $U^2_{\rm rms}$ was almost constant in depths ranging from 0.4–2.5 m and that the variance $V^2_{\rm rms}$ increased monotonically as depth decreased as shown in Figure 4.39, which indicated the cross-shore variations of the variances of the total, high-frequency, and low-frequency components of the cross-shore and alongshore velocities. Their field data and the computed results shown in

Figures 4.37 and 4.38 point out the inadequacy of the conventional assumption of depth-limited, linear breaking waves made in existing time-averaged models.

The time-averaged wave energy equation (3.7) is used to examine the cross-shore variations of the time-averaged values of the specific energy $\overline{E}$, the energy flux $\overline{E_F}$, the dissipation rate $\overline{D_f}$ due to bottom friction, and the dissipation rate $\overline{D_B}$ due to wave breaking as shown in Figure 4.40. The computed dissipation rate $\overline{D_B}$ indicates intense wave breaking immediately seaward of the still water shoreline located at $x = 2.56$ on February 5 and at $x = 3.82$ on February 6 in Figure 4.40. This intense wave breaking may partly explain the large oscillatory velocities near the still water shoreline shown in Figures 4.37 and 4.38. The computed wave energy dissipation in the swash zone is caused mostly by bottom friction due to the large cross-shore velocity U in the swash zone.

The large oscillatory velocities near the still water shoreline may also be caused by low frequency waves. In the very shallow water for the velocity data of Guza and Thornton (1985) as shown in Figure 4.39, the low- and high-frequency components of the variance $U^2_{\rm rms}$ were of the same magnitude and the variance $V^2_{\rm rms}$ was dominated by the low frequency component. For comparison, the oscillatory components $(\eta - \overline{\eta})$, $(U - \overline{U})$ and $(V - \overline{V})$ are filtered to obtain the components of $\eta^2_{\rm rms}$, $U^2_{\rm rms}$ and $V^2_{\rm rms}$ in the high-frequency $(f' > 0.05\ Hz)$ and low-frequency $(f' < 0.05\ Hz)$ bands as shown in Figures 4.41 and 4.42. The computed low-frequency components of $\eta^2_{\rm rms}$ and $U^2_{\rm rms}$ in the swash zone turn out to be smaller than the corresponding high-frequency components probably because the incident low-frequency wave components are not included in the specified incident wave train in the 3 m depth as shown in Figure 4.13. Furthermore, edge waves are excluded in this numerical model. On the other hand, the computed low- and high-frequency components of $V^2_{\rm rms}$ are of the same magnitude near the still water shoreline even in the absence of incident low frequency waves and edge waves.

Recently, Kobayashi *et al.* (1997) derived simple relationships between the free surface and cross-shore velocity statistics using linear progressive long-wave theory. Accordingly, the relationship between the normalized standard deviations of η and U may be expressed as

$$U_{\rm rms} \simeq \frac{\eta_{\rm rms}}{\sqrt{\overline{h}}} \tag{4.10}$$

whereas the mean cross-shore velocity $\overline{U}$ is estimated as

$$\overline{U} \simeq -\sqrt{\overline{h}} \left(\frac{\eta_{\rm rms}}{\overline{h}} \right)^2 \tag{4.11}$$

where $\eta_{\rm rms}$ and $U_{\rm rms}$ are the standard deviation of η and U, respectively, and $\overline{h}$ is the mean water depth including wave setup.

Figures 4.43 and 4.44 show the comparisons of the cross-shore variations of $U_{\rm rms}$ and $\overline{U}$ computed using the 2D model and using (4.10) and (4.11) together with the computed values of $\eta_{\rm rms}$ and $\eta_{\rm rms}/\overline{h}$ for February 5 and 6, respectively. The normalized bottom elevation is depicted with the dotted line in the top panel of these figures. Similar to the experimental results of Kobayashi *et al.* (1997), the computed values of $\eta_{\rm rms}/\overline{h}$ in Figures 4.43 and 4.44 increases gradually and then rapidly near the shoreline as $\overline{h}$ approaches zero. Hence, contrary to the field data obtained by Thornton and Guza (1982, 1983), the computed values of $\eta_{\rm rms}/\overline{h}$ do not approach constant in the inner surf zone. These figures also show that the simple relationships (4.10) and (4.11) based on linear progressive long-wave theory predicts the standard deviation of cross-shore velocity, $U_{\rm rms}$, and the mean cross-shore velocity, $\overline{U}$, fairly well up to the still water shoreline. Consequently, the large velocities seaward of the still water shoreline may simply be explained by the landward increase of $\eta_{\rm rms}/\overline{h}$ in which the landward decrease of $\eta_{\rm rms}$ is more gradual than that of $\overline{h}$ as shown in Figures 4.43 and 4.44. In the swash zone, local nonlinear effects such as the bottom friction as well as wave reflection appear to be important in view of the comparison shown in these figures.

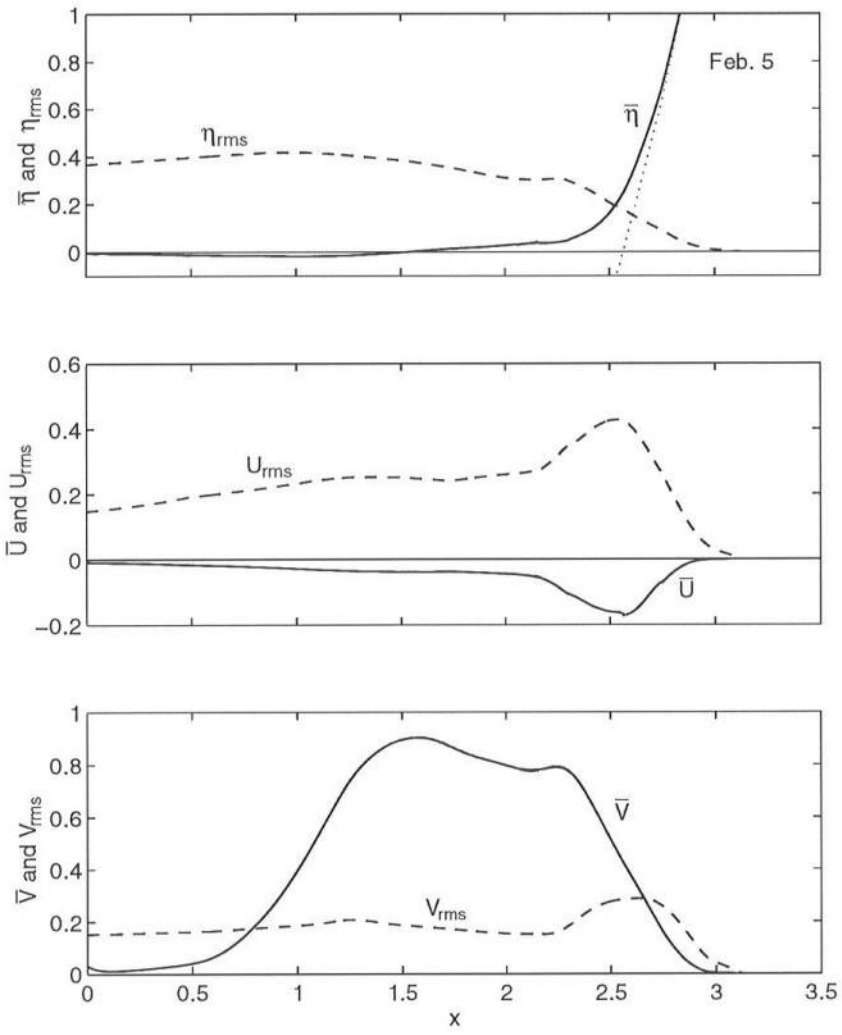

Figure 4.37: Computed cross-shore variations of mean and standard deviation of free surface elevation η, cross-shore velocity U and alongshore velocity V for February 5.

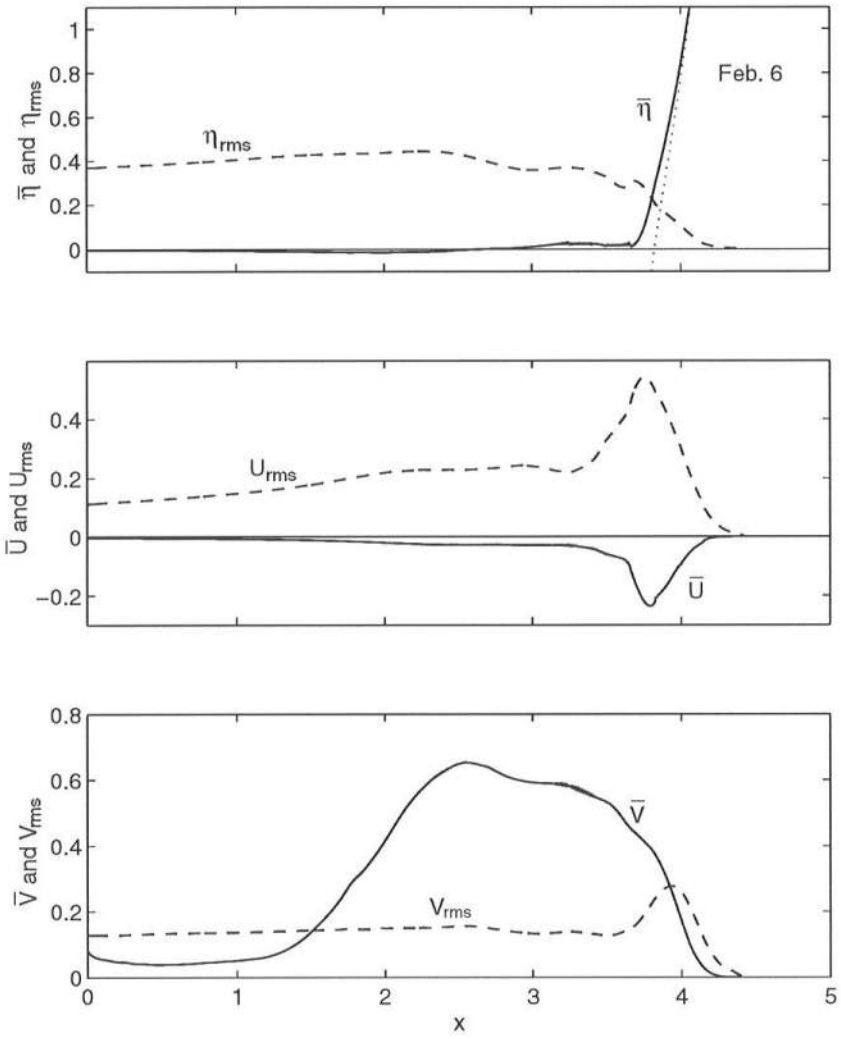

Figure 4.38: Computed cross-shore variations of mean and standard deviation of free surface elevation η, cross-shore velocity U and alongshore velocity V for February 6.

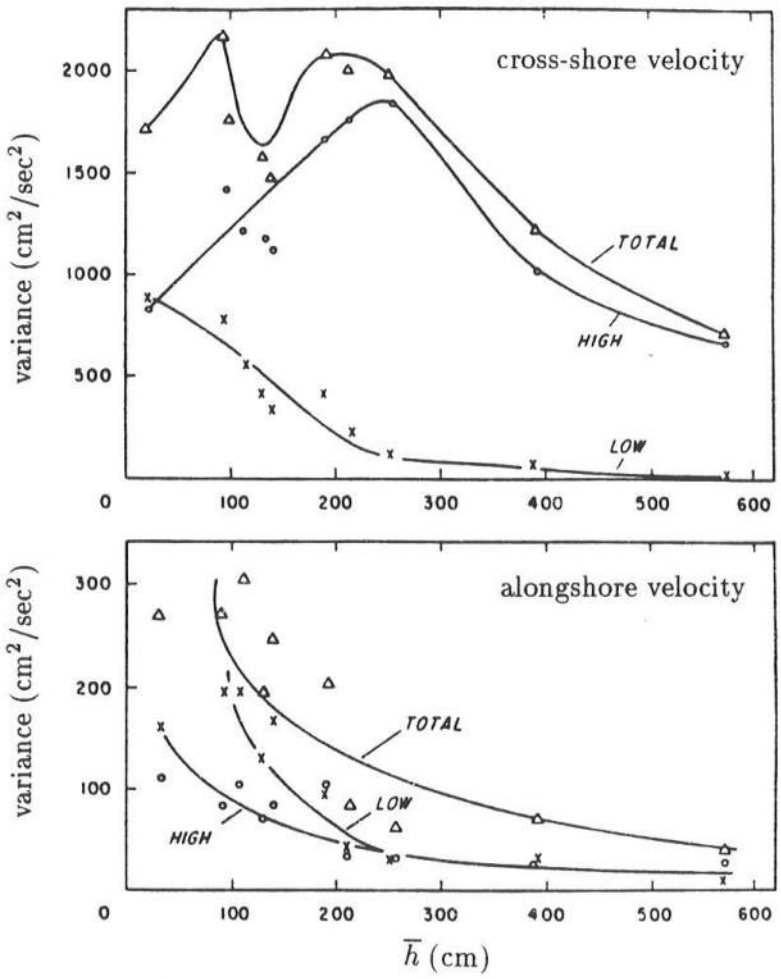

Figure 4.39: Total, high-frequency and low-frequency components of cross-shore velocity and alongshore velocity as a function of mean depth $\overline{h}$ (from Guza and Thornton 1985).

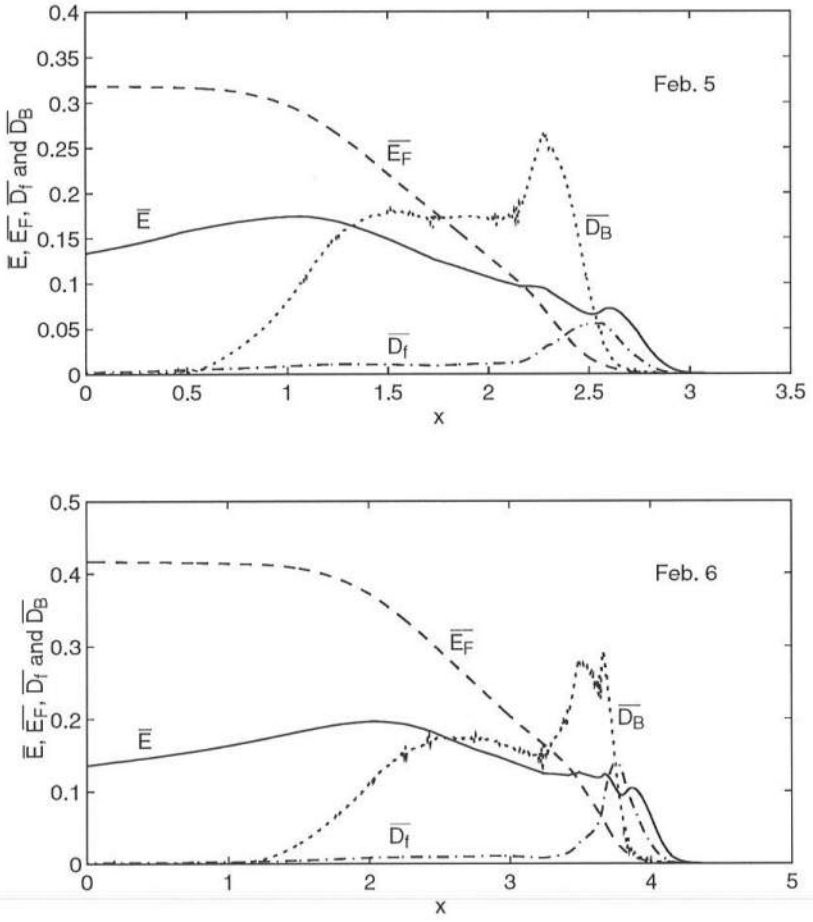

Figure 4.40: Computed cross-shore variations of specific energy $\bar{E}$, energy flux $\bar{E}_F$, dissipation rate $\bar{D}_f$, and $\bar{D}_B$ due to bottom friction and wave breaking, respectively, for February 5 and February 6.

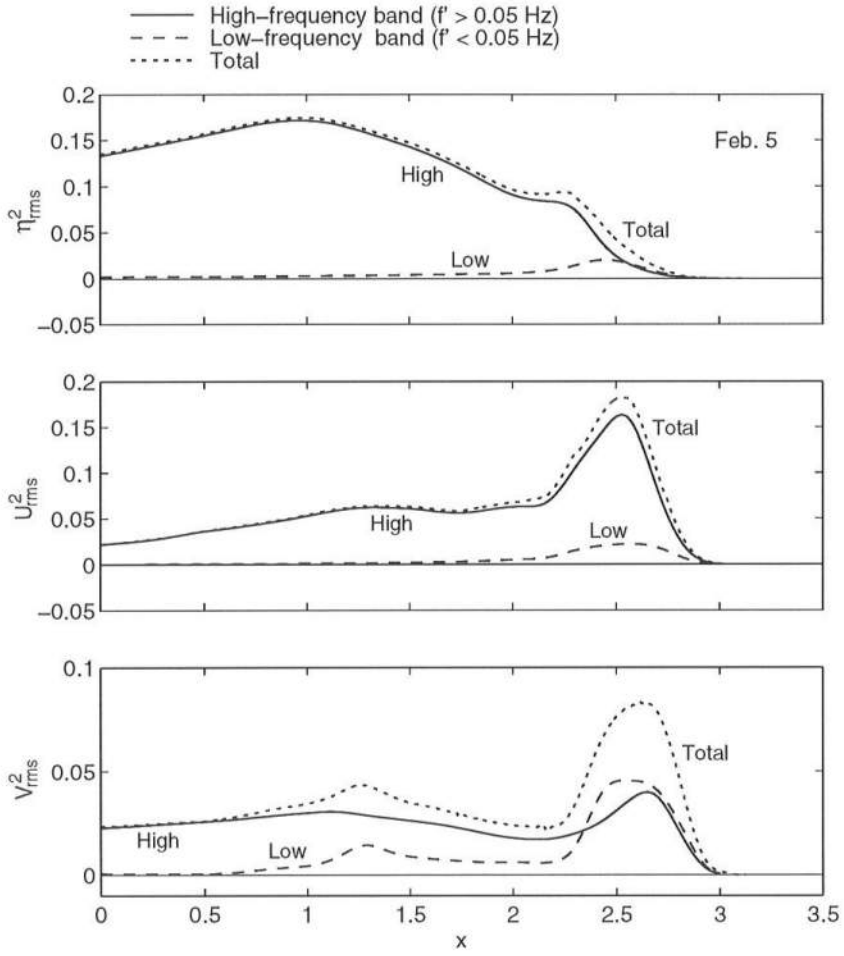

Figure 4.41: Computed cross-shore variations of variances of free surface elevation η, cross-shore velocity U and alongshore velocity V in high ($f' > 0.05Hz$) and low ($f' < 0.05Hz$) frequency bands for February 5.

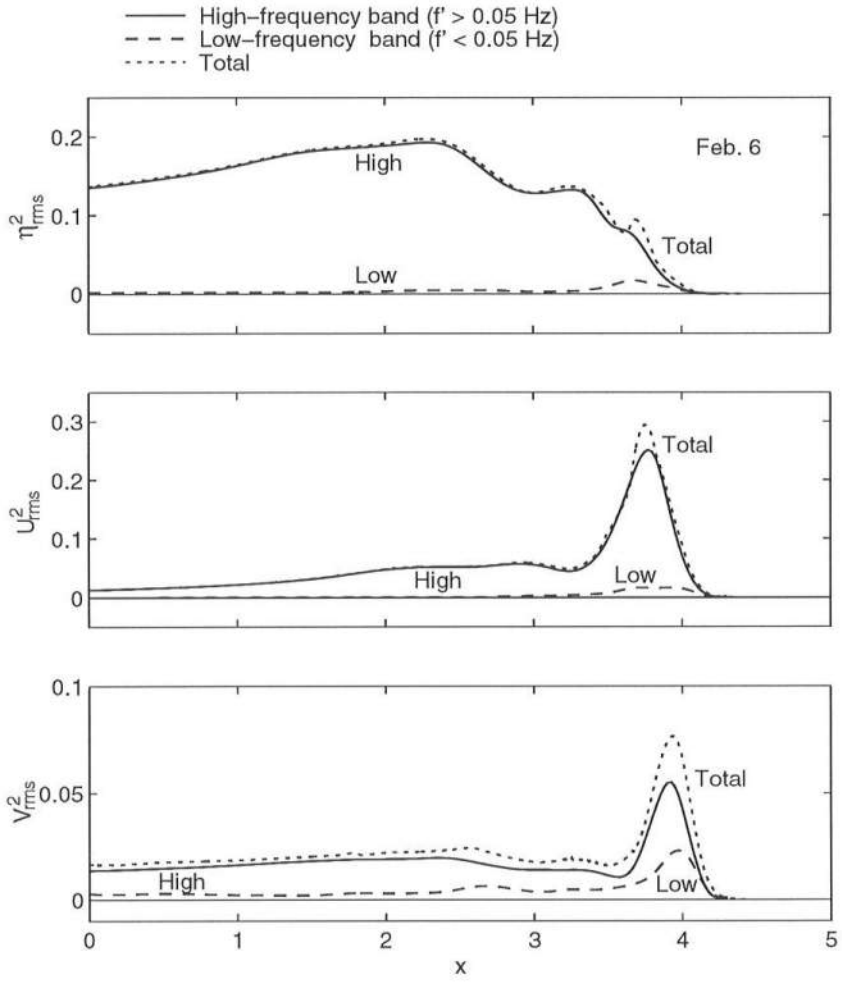

Figure 4.42: Computed cross-shore variations of variances of free surface elevation η, cross-shore velocity U and alongshore velocity V in high ($f' > 0.05Hz$) and low ($f' < 0.05Hz$) frequency bands for February 6.

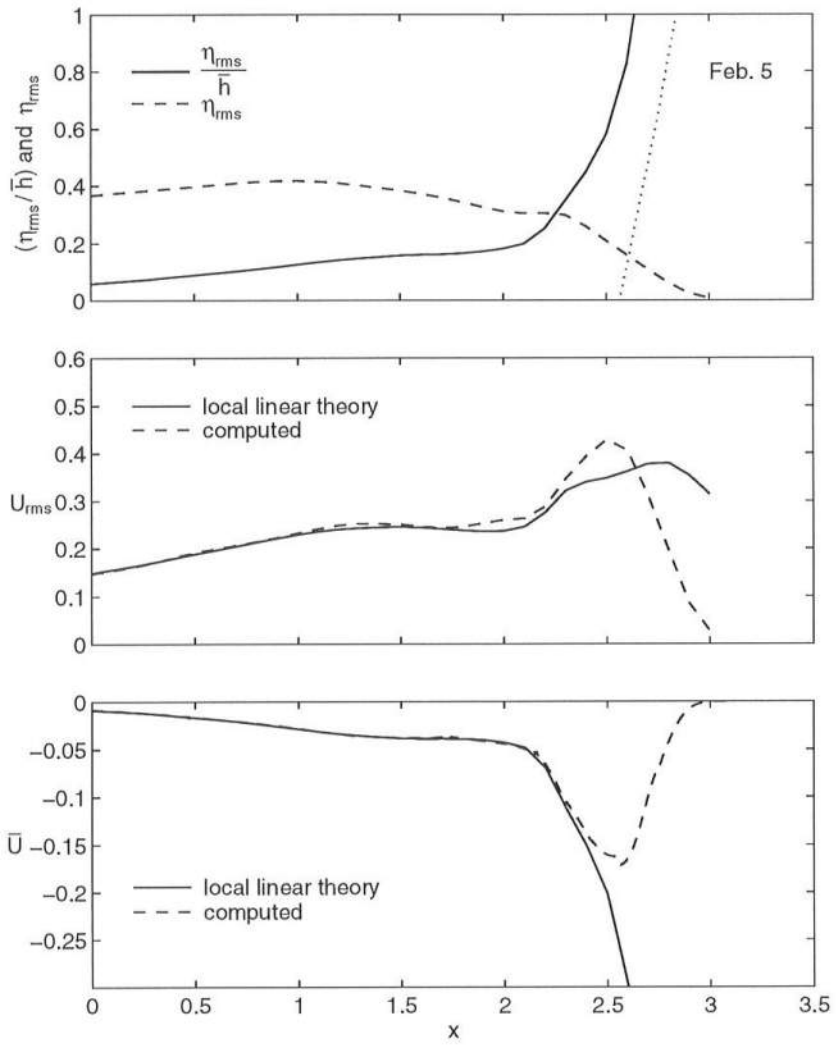

Figure 4.43: Cross-shore variations of $\eta_{\rm rms}, \eta_{\rm rms}/\overline{h}, U_{\rm rms}$ and $\overline{U}$ computed using the 2D model as well as cross-shore variations of $U_{\rm rms}$ and $\overline{U}$ computed using (4.10) and (4.11) together with the normalized bottom elevation for February 5.

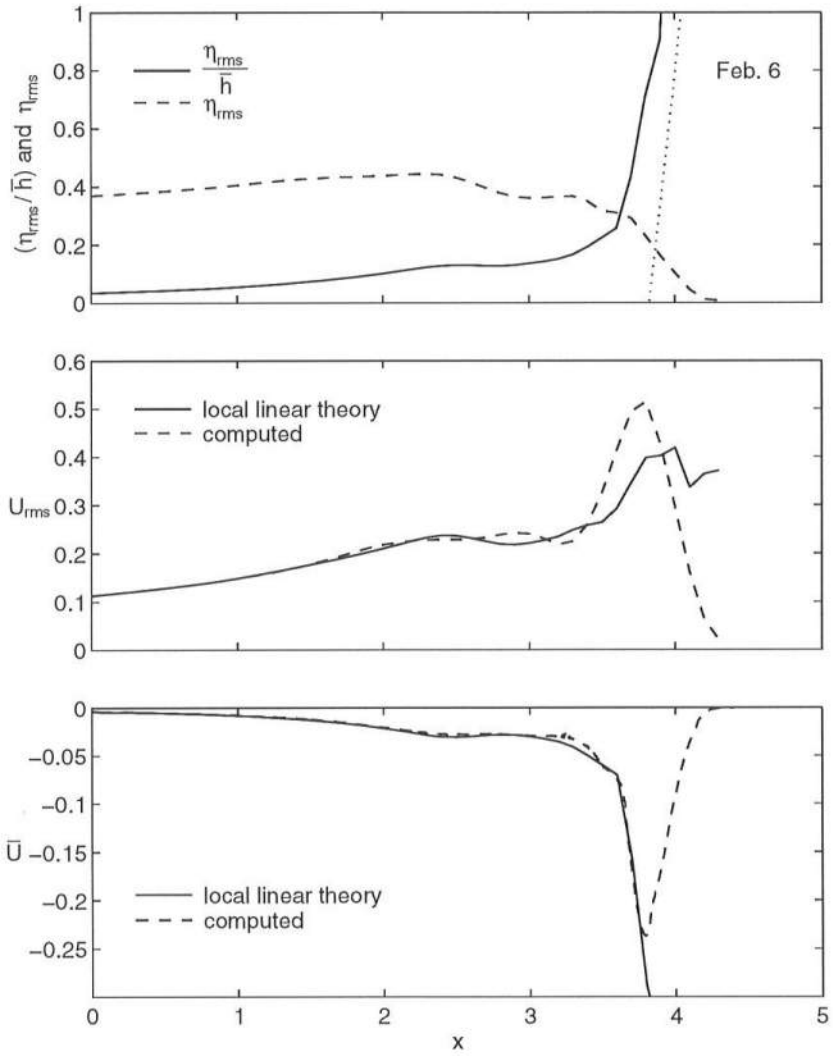

Figure 4.44: Cross-shore variations of $\eta_{\text{rms}}, \eta_{\text{rms}}/\overline{h}, U_{\text{rms}}$ and $\overline{U}$ computed using the 2D model as well as cross-shore variations of U_{rms} and $\overline{U}$ computed using (4.10) and (4.11) together with the normalized bottom elevation for February 6.

Chapter 5

COMPARISON OF THE QUASI-3D MODEL WITH AVAILABLE DATA

The computed results presented in Chapter 4 are based on the depth-integrated continuity equation (3.1) and the depth-integrated horizontal momentum equations (3.2) and (3.3), neglecting the dispersion due to vertical non-uniformities of the horizontal velocities u and v. However, wave breaking produces vertical variations in the horizontal velocities and resulting energy dissipation (*e.g.*, Svendsen and Madsen 1984). Furthermore, the vertical variations of instantaneous velocities and shear stresses are required for detailed analyses of sediment transport in the surf zone. Although Thornton and Guza (1986) have already concluded that the dispersion effects were not important for predicting longshore currents on a planar beach generated by random waves, the computed results for regular waves depicted in Figure 4.9 suggest that the dispersion terms are required to improve the agreement.

Very little is known of these dispersion effects on surf zone hydrodynamics apart from the analysis of Svendsen and Putrevu (1994) that showed the importance of the dispersion effect due to the nonlinear interaction of cross-shore and longshore currents in explaining the measured cross-shore variations of longshore currents induced by regular breaking waves. They used a time-averaged model in their dispersion analysis where linear wave theory with depth-limited breaker height was employed to describe the wave motion.

To assess the importance of the added dispersion terms m and n in the time-dependent momentum equations (3.47) and (3.48) due to the vertical variations of instantaneous horizontal velocities u and v, the 3D model described in Section 3.2 is compared with the same regular and irregular wave data as in Chapter 4.

5.1 Comparison with Regular Wave Data

5.1.1 Comparison of 2D and 3D Models with Data

The 3D model is compared with the same four experiments of Visser (1991) as in Section 4.2. The depth-averaged longshore current data of Visser (1991) was based on the current velocity measurements of dye clouds injected at three depths. The 3D computations are made in the same way as the corresponding 2D computations presented in Section 4.2 except the seaward boundary location for experiment 4 in the 2D and 3D computations is moved somewhat closer to the breaker line to better satisfy the assumption of shallow water. For experiment 4, the incident wave characteristics specified as input to the numerical model are: water depth at the seaward boundary $d_i' = 12.41$ cm, wave period $T' = 1.02$ s, wave height $H' = 8.4$ cm, incident wave angle $\theta_i = 13.1°$ whereas the values for experiments 2, 3 and 5 remain the same as listed in Table 4.1.

The temporal variations of the free surface elevation η and the depth-averaged cross-shore velocity U computed by the 3D model are practically the same as those computed by the 2D model shown in Figures 4.2 and 4.3 and hence are not presented here. The depth-averaged alongshore velocity V shown in Figure 4.4 for the 2D model is modified considerably as depicted in Figure 5.1 for experiment 2. As a whole, the alongshore velocity V is smaller than in Figure 4.4. The measured and computed cross-shore variations of the local wave height H, the wave setup $\overline{\eta}$, and the depth-averaged longshore current $\overline{V}$ for experiments 2–5 are compared in Figures 5.2 – 5.4, respectively. The normalized bottom elevation for each experiment is shown as the straight line in Figure 5.3. For the cross-shore fluid motion repre-

sented by H and $\overline{\eta}$, the differences between the 2D and 3D computations are minor, probably within the accuracy of these models in light of the agreement shown in Figures 5.2 and 5.3. This implies that the dispersion term m in the depth-integrated cross-shore momentum equation (3.47) is secondary as anticipated by Kobayashi and Wurjanto (1992).

The average values of the relative errors for the 2D and 3D computations for each experiment are inserted in the parentheses in Figures 5.2 and 5.3. The relative error for each data point is defined as $|Y_m - Y_c|/|Y_m|$ where Y_m = measured value and Y_c = computed value. The average relative error for the mean water elevation, $\overline{\eta}$, is large because of the difficulty in predicting the relatively small set-down and setup accurately.

On the other hand, for the alongshore fluid motion represented by the longshore current $\overline{V}$, which is dominant in comparison to the oscillatory alongshore velocity in the surf zone in these experiments, the dispersion term n in the depth-integrated alongshore momentum equation (3.48) improves the agreement of the longshore current profile noticeably as shown in Figure 5.4. The longshore currents computed using $f_b' = 0.02$ and 0.025 for experiment 4 and $f_b' = 0.02$ for experiment 5 are also shown in Figure 5.4. The alongshore bottom shear stress τ_{by} in (3.48) is important in determining the magnitude of $\overline{V}$ but modifies its profile little as expected from the previous work (*e.g.*, Longuet-Higgins 1970). It is noted that the cross-shore variations of H and $\overline{\eta}$ computed using these bottom friction factors for experiments 4 and 5 are indistinguishable from those shown in Figures 5.2 and 5.3 for $f_b' = 0.05$ and are not plotted in these figures. The importance of the dispersion effect on the longshore currents in Figure 5.4 is consistent with the analysis of Svendsen and Putrevu (1994) based on the vertical variations of currents only, while the present analysis is based on the vertical variations of the instantaneous horizontal velocities.

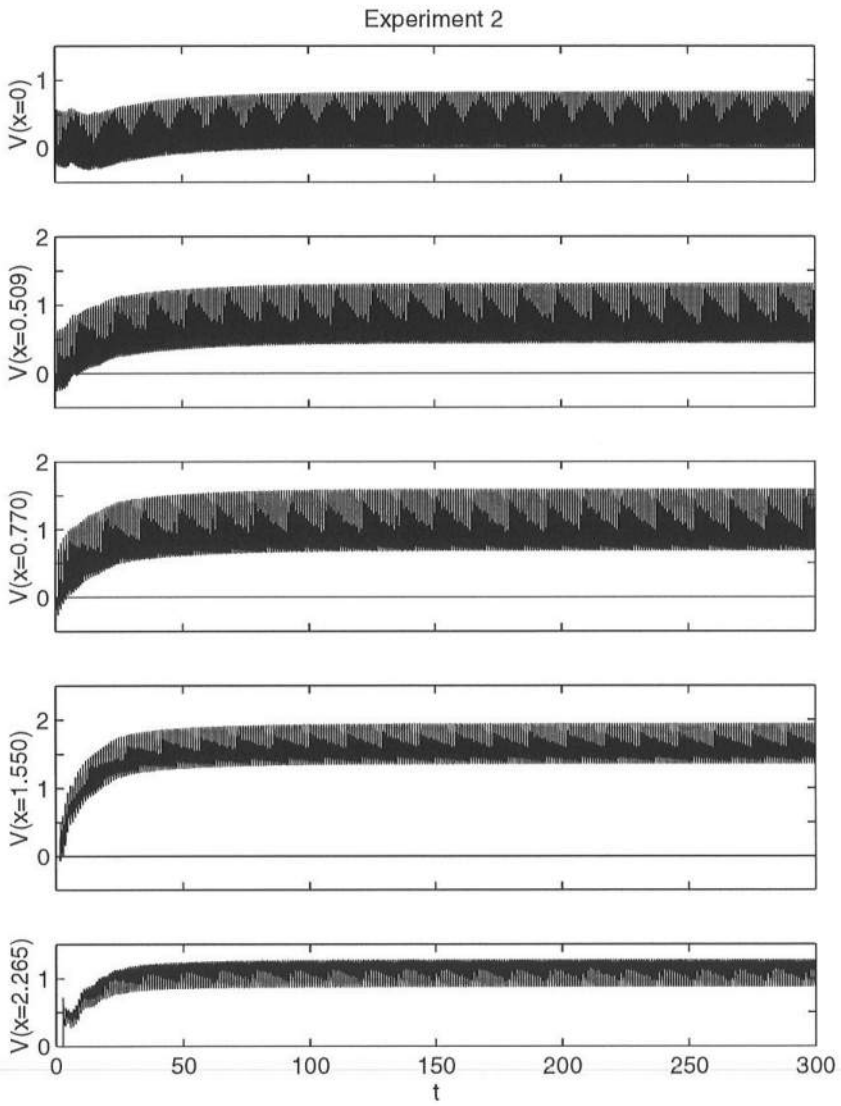

Figure 5.1: Computed temporal variations of depth-averaged alongshore velocity V at $x = 0, 0.509, 0.770, 1.550$ and 2.265 using 3D model.

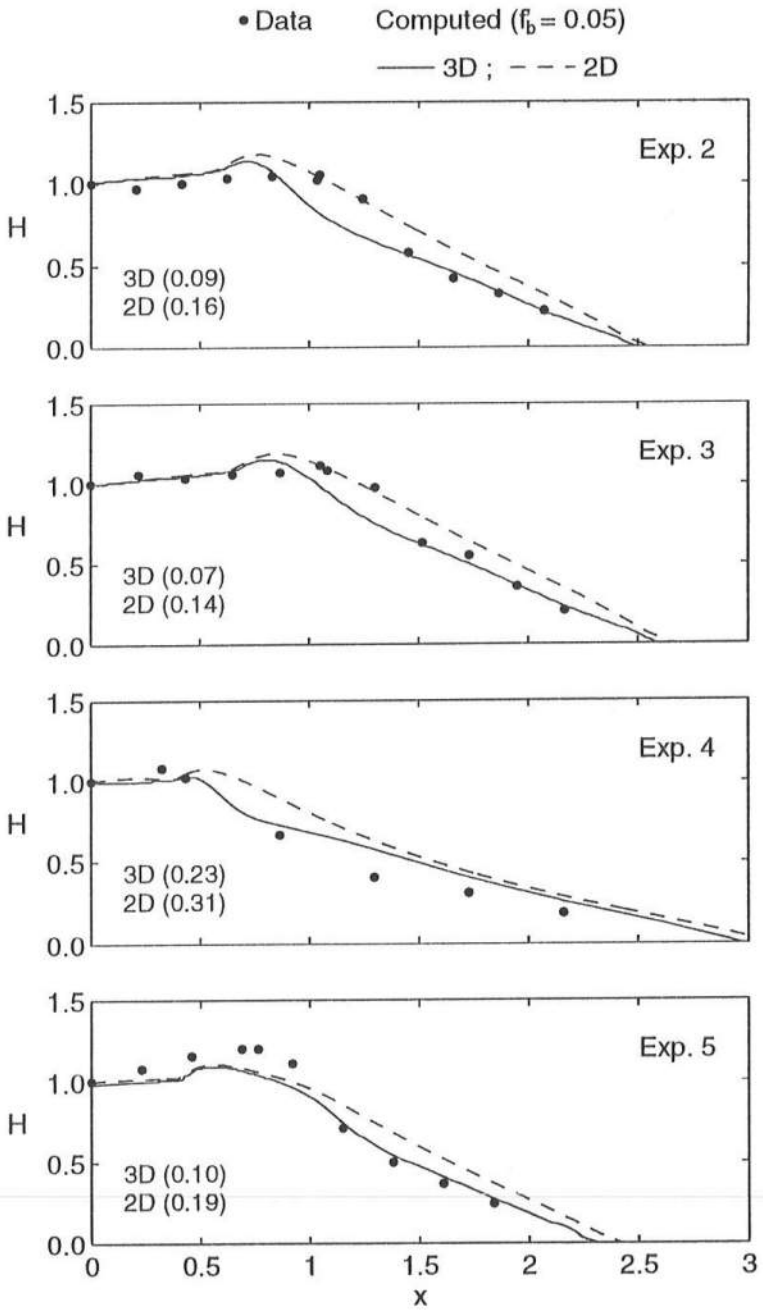

Figure 5.2: Measured and computed local wave height H for four experiments for comparison of 2D and 3D models.

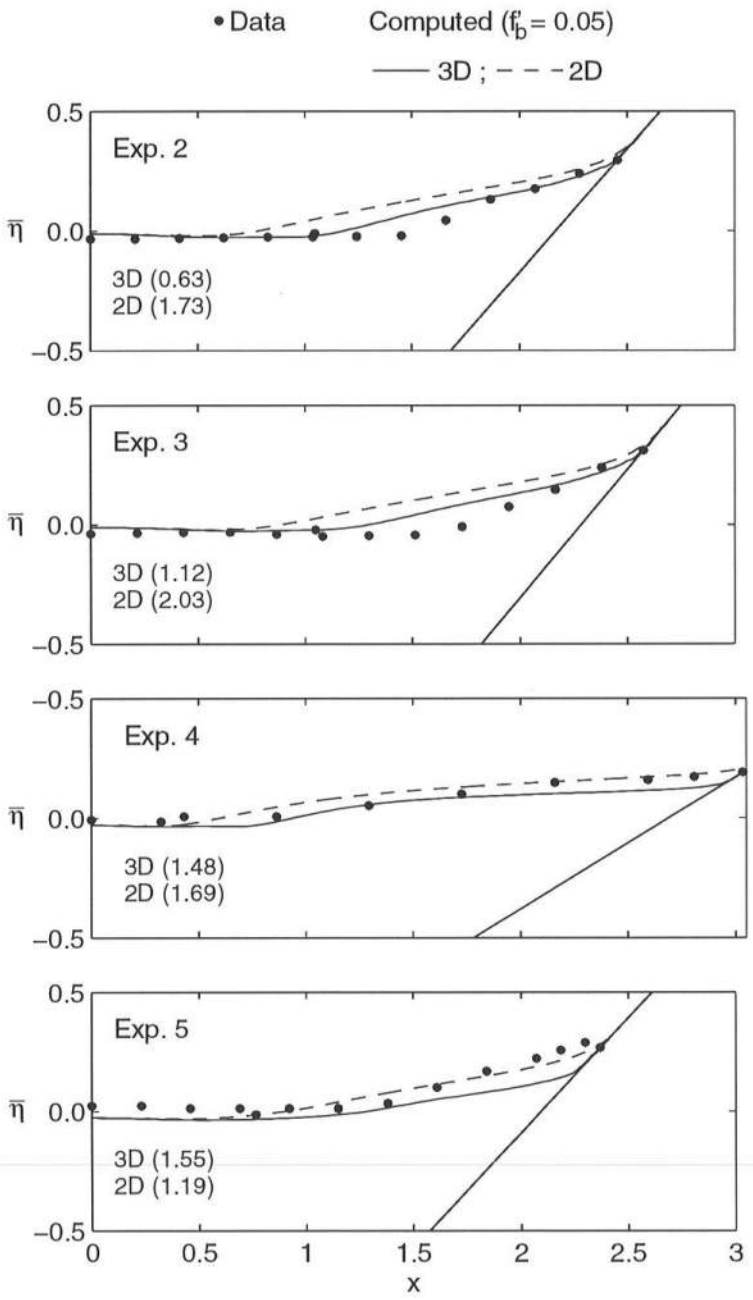

Figure 5.3: Measured and computed wave setup $\overline{\eta}$ for four experiments for comparison of 2D and 3D models.

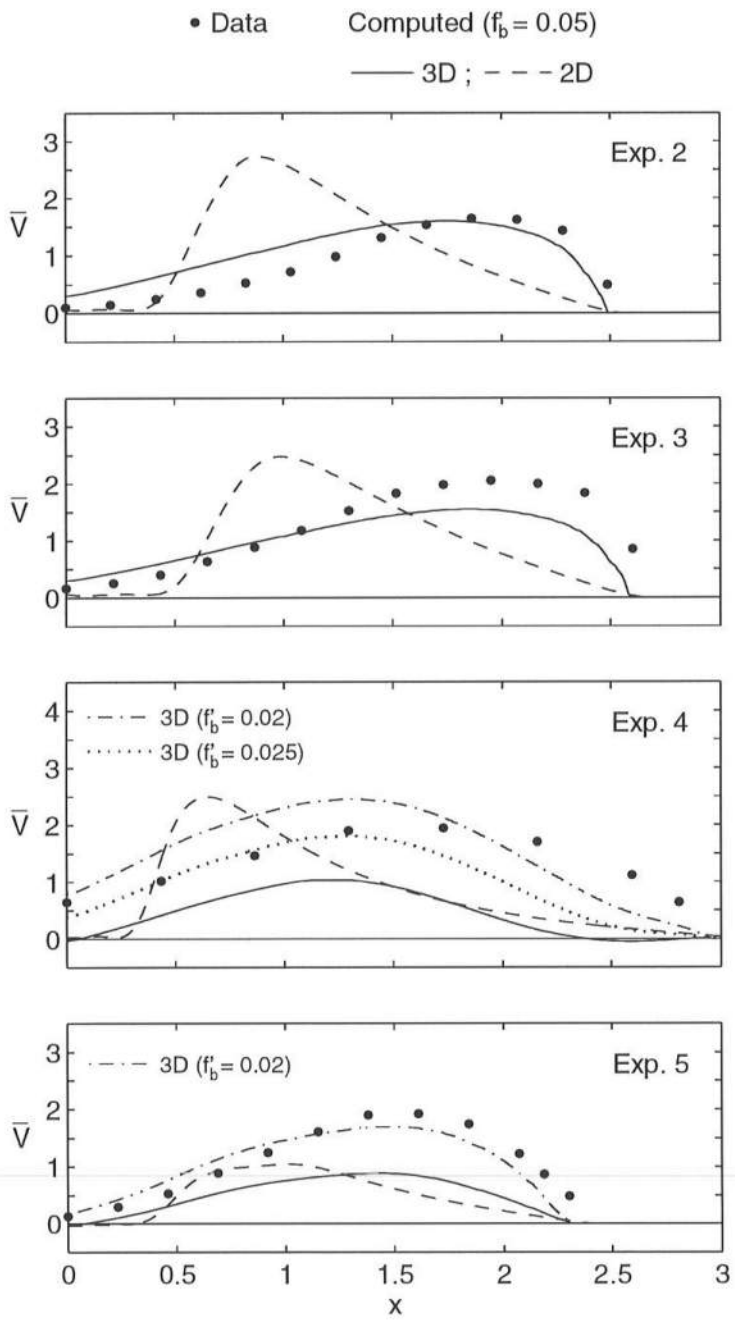

Figure 5.4: Measured and computed depth-averaged longshore current $\overline{V}$ for four experiments for comparison of 2D and 3D models.

To explain the computed results in Figure 5.4, the time-averaged alongshore momentum equation (3.61) for the case of alongshore uniformity is given by

$$\frac{d}{dx}(S_{xy}) + \frac{d\overline{n}}{dx} = -\overline{\tau}_{by} \tag{5.1}$$

in which $S_{xy} = \overline{hUV}$ is the alongshore radiation stress based on the depth-averaged velocities U and V. The mean alongshore momentum flux $\overline{n}$ due to the vertical variations of the horizontal velocities u and v is included in the 3D model, whereas $\overline{n} = 0$ for the 2D model. Figure 5.5 shows the computed cross-shore variations of dS_{xy}/dx and $d\overline{n}/dx$ for experiment 2 as an example. The cross-shore gradients of S_{xy} for the 2D and 3D computations are similar because h, U and V are not affected much by the dispersion terms m and n. This figure indicates that the term $d\overline{n}/dx$ included in the 3D model decreases the force driving the longshore current near the breaker point but increases this force near the shoreline. Correspondingly, the computed longshore current $\overline{V}$ for the 3D model in Figure 5.4 is reduced near the breaker point but increased near the shoreline. In short, the dispersion term $\overline{n}$ is important in the time-averaged alongshore momentum equation (5.1).

5.1.2 Vertical Variations of Longshore Currents

The depth-averaged longshore current data of Visser (1991) were based on the current velocity measurements of dye clouds injected at the surface, mid-depth, and 1 cm above the bed. The measured vertical variations of the longshore current $\overline{v}$ were presented for experiments 3 and 4 in Figures 5.6 and 5.7 where the cross-shore location x is indicated for each vertical measuring line. The vertical variation of the alongshore velocity v for the 3D model is computed using (3.58), (3.59) and (3.60) for the computed temporal and cross-shore variations of V, $\tilde{v}_b$ and h in these equations. It is noted that the 2D model does not yield the vertical velocity variations. The time-averaged velocity $\overline{v}$ is computed for the given elevation $(z-z_b)$ above the bottom and below the wave trough level where $z_b = (-d)$ is the normalized bottom elevation

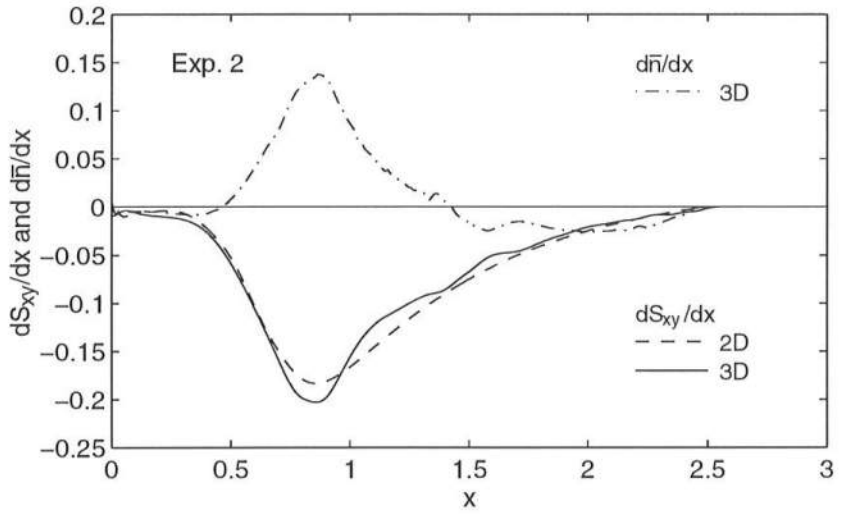

Figure 5.5: Computed cross-shore gradients of S_{xy} and $\overline{n}$ for experiment 2.

introduced for clarity. To estimate $\overline{v}$ above the trough level, $\overline{v}$ is also computed for the given value of $\zeta = (z - z_b)/h$ with $\zeta = 1$ at the instantaneous free surface and plotted as a function of the mean elevation, $(z - z_b) = \zeta\overline{h}$, with $\overline{h}$ = mean water depth. Figures 5.6 and 5.7 show that the vertical variations of $\overline{v}$ computed for the given $(z - z_b)$ and ζ are almost identical inside the surf zone where the breaker point was located at $x = 0.9$ for experiment 3 and $x = 0.5$ for experiment 4. The measured and computed vertical profiles of $\overline{v}$ are approximately parallel except outside the surf zone where the assumed cubic profile (3.60) for breaking waves may not be appropriate. Outside the surf zone, the vertical profile of $\overline{v}$ decreases with the increase of $(z - z_b)$. In this region, $dS_{xy}/dx = 0$, so that the currents are entirely driven by the dispersion mechanism and the (much weaker) turbulent mixing (Svendsen and Putrevu 1994). The discrepancy between the measured and computed longshore current $\overline{v}$ inside the surf zone in Figures 5.6 and 5.7 is mostly caused by the error in the predicted depth-averaged longshore current $\overline{V}$ shown in Figure 5.4 where Figure 5.7 is based on $f_b' = 0.025$ for experiment 4.

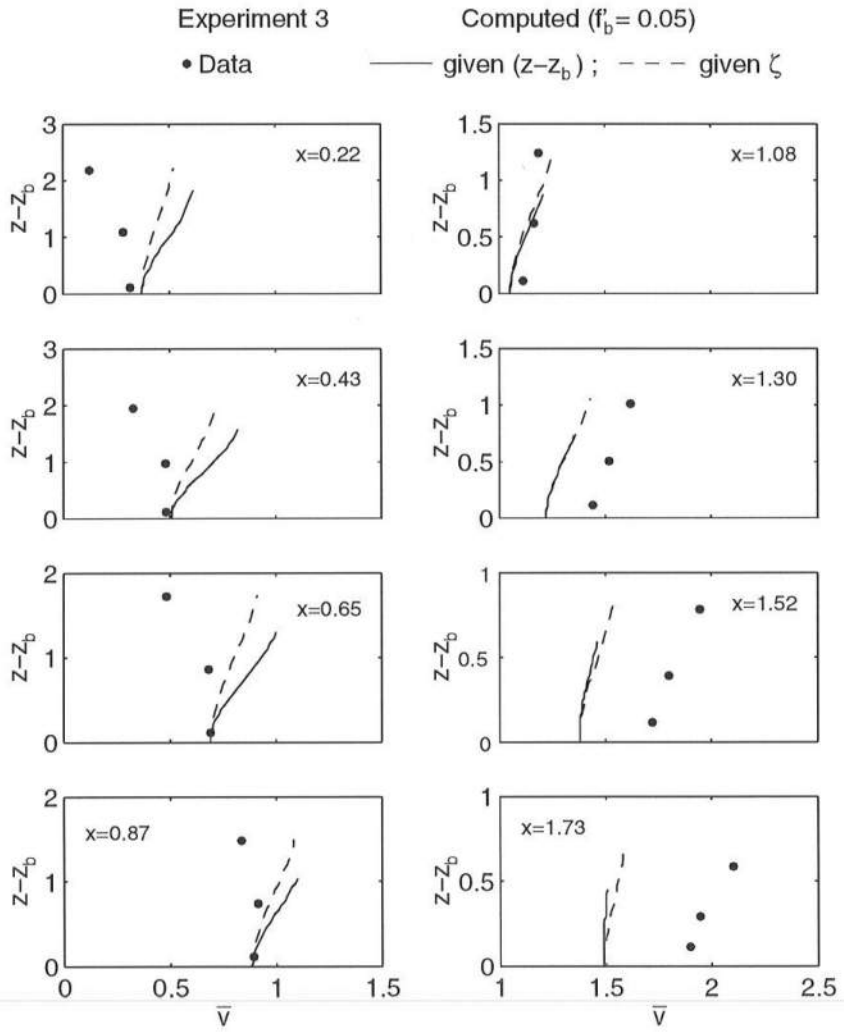

Figure 5.6: Measured and computed vertical variations for longshore current $\overline{v}$ for experiment 3 for 3D model.

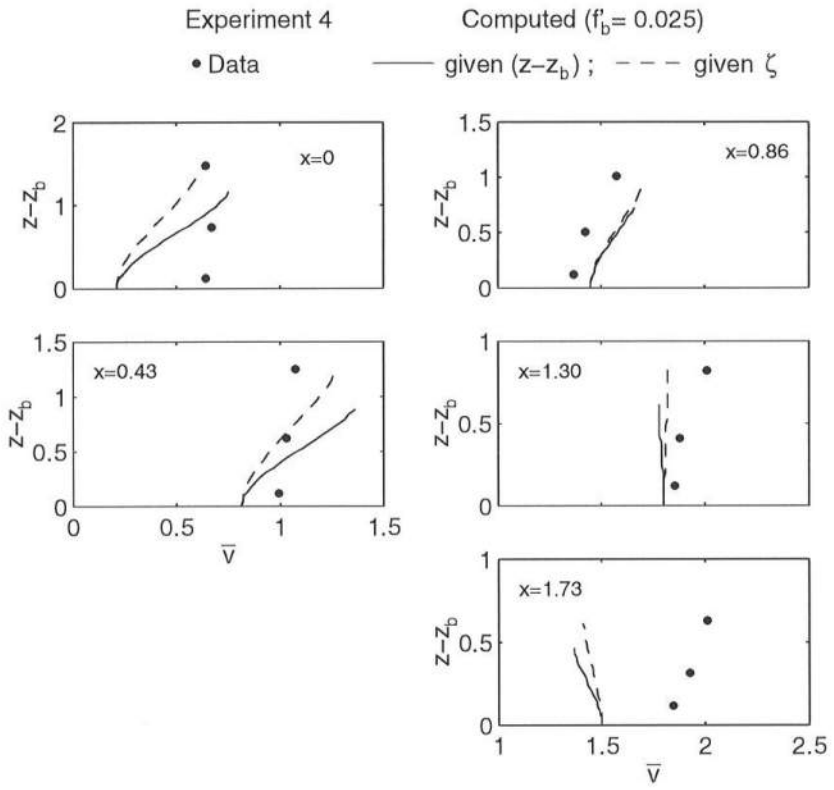

Figure 5.7: Measured and computed vertical variations for longshore current $\overline{v}$ for experiment 4 for 3D model.

As for the vertical variation of the instantaneous cross-shore velocity u, Johnson *et al.* (1996) compared the numerical model based on (3.46), (3.47) and (3.52) for normally incident waves with the velocity measurements below the trough level by Cox *et al.* (1994). The vertical variations of the measured and computed cross-shore velocities were relatively small below the trough level and above the bottom boundary layer. The computed vertical variation of u above the trough level could not be verified for lack of data.

5.1.3 Numerical Damping and Dissipation

According to Kobayashi and Johnson (1995), the value of numerical damping coefficient κ used for the 3D model in the smoothing procedure for breaking waves on the gently sloping beach is on the order of unity as discussed in Section 3.2. As a result, $\kappa = 1$ has been used unless stated otherwise. The computation using $\kappa = 1$ improves the prediction of the transition zone but underpredicts the maximum setup for experiments 4 and 5 in Figure 5.3. Figure 5.8 shows that the computed wave setup $\overline{\eta}$ using $\kappa = 0.3$ for the 3D model yields slightly better agreement for experiments 4 and 5. Table 5.1 and 5.2 compares the measured and computed maximum setup and runup for the four experiments using κ= 1 and 0.3 in the same way as in Table 4.2. It is noted that the measured values for experiment 4 are slightly different from those in Table 4.2 since the normalization is made using the different value of the wave height H' at the shallower seaward boundary location. On the other hand, Figures 5.9 and 5.10 show that the cross-shore variations of the wave height H and the depth-averaged longshore current $\overline{V}$ based on $\kappa = 0.3$ do not change much as compared to the computed results with $\kappa = 1$. In summary, the numerical damping coefficient κ in the range of κ =0.3–1 modifies the computed results slightly but does not change the essential features of the computed results using the 3D model.

Table 5.1: Measured and computed maximum setup $\overline{\eta}$ using different values of κ for 3D model.

Expt. No.	Maximum Setup						
	Computed ($\kappa = 1$)			Computed ($\kappa = 0.3$)			
	1mm	5mm	10mm	1mm	5mm	10mm	Meas.
2	0.29	0.25	0.22	0.37	0.32	0.29	0.29
3	0.28	0.24	0.21	0.36	0.32	0.29	0.31
4	0.14	0.12	0.11	0.19	0.18	0.17	0.19
5	0.18	0.15	0.13	0.25	0.21	0.19	0.27

Table 5.2: Measured and computed runup using different values of κ for 3D model.

Expt. No.	Runup						
	Computed ($\kappa = 1$)			Computed ($\kappa = 0.3$)			
	1mm	5mm	10mm	1mm	5mm	10mm	Meas.
2	0.32	0.30	0.29	0.40	0.38	0.36	0.43
3	0.31	0.30	0.29	0.40	0.38	0.35	0.47
4	0.15	0.15	0.16	0.21	0.21	0.21	0.23
5	0.20	0.20	0.20	0.29	0.27	0.27	0.34

The time-averaged energy quantities are shown in Figure 5.11. The numerical dissipation rate, $\overline{D}_{\text{numerical}}$, shown in the last panel and defined in (3.69) is the difference between the values of $\overline{D_B}$ computed using the time-averaged energy equation (3.63) and the physical dissipation rate $\overline{D_B}$ predicted using (3.68) for the 3D model. It is noted that the numerical dissipation rate is of the same order as the wave breaking dissipation rate computed using (3.68) explicitly in the 3D model. The values of $\kappa = 0.3$ and 1.0 have only minor effects on the time-averaged energy quantities. This suggests the shortcoming of the cubic velocity profile assumed in (3.60) to describe the wave energy dissipation due to breaking on the gentle slope. This probably arises from the fact that the wave front (roller) is not modeled specifically in the 3D model (Johnson *et al.* 1996).

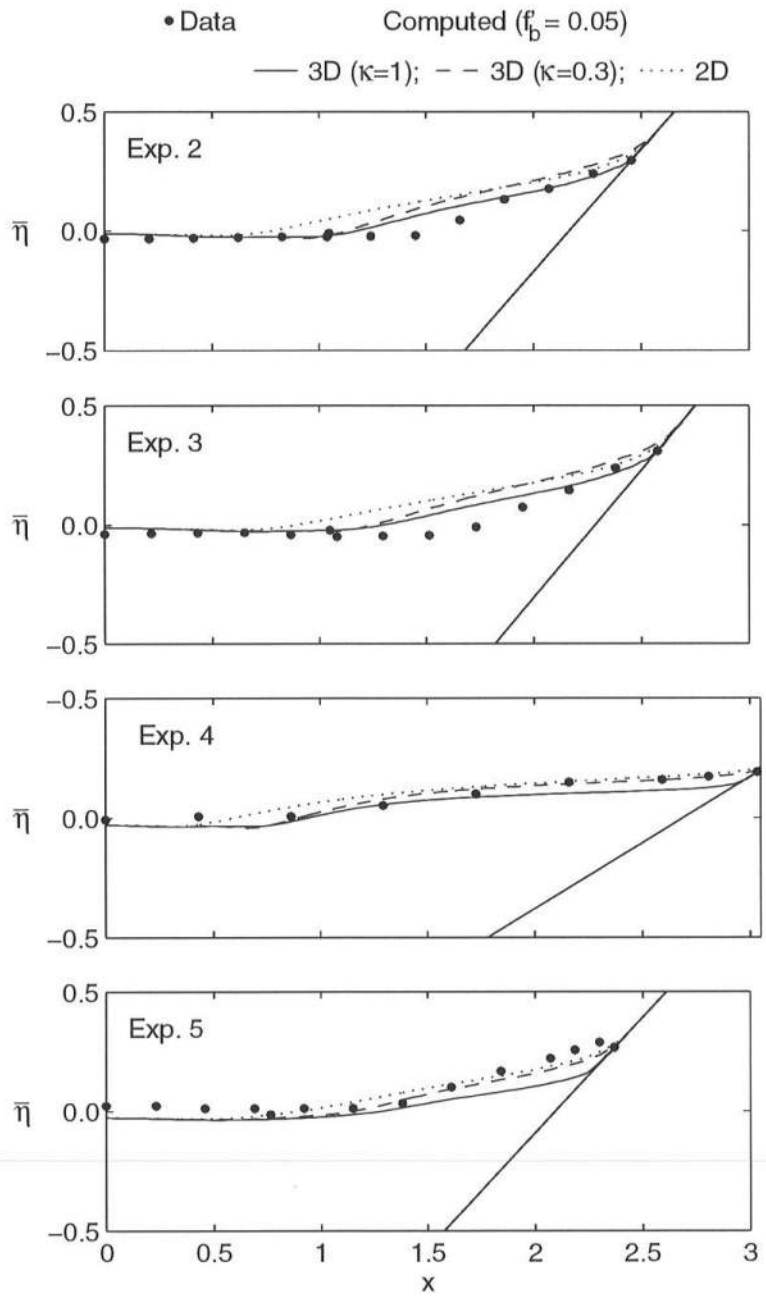

Figure 5.8: Measured and computed wave setup $\overline{\eta}$ for four experiments using different values of κ for 3D model.

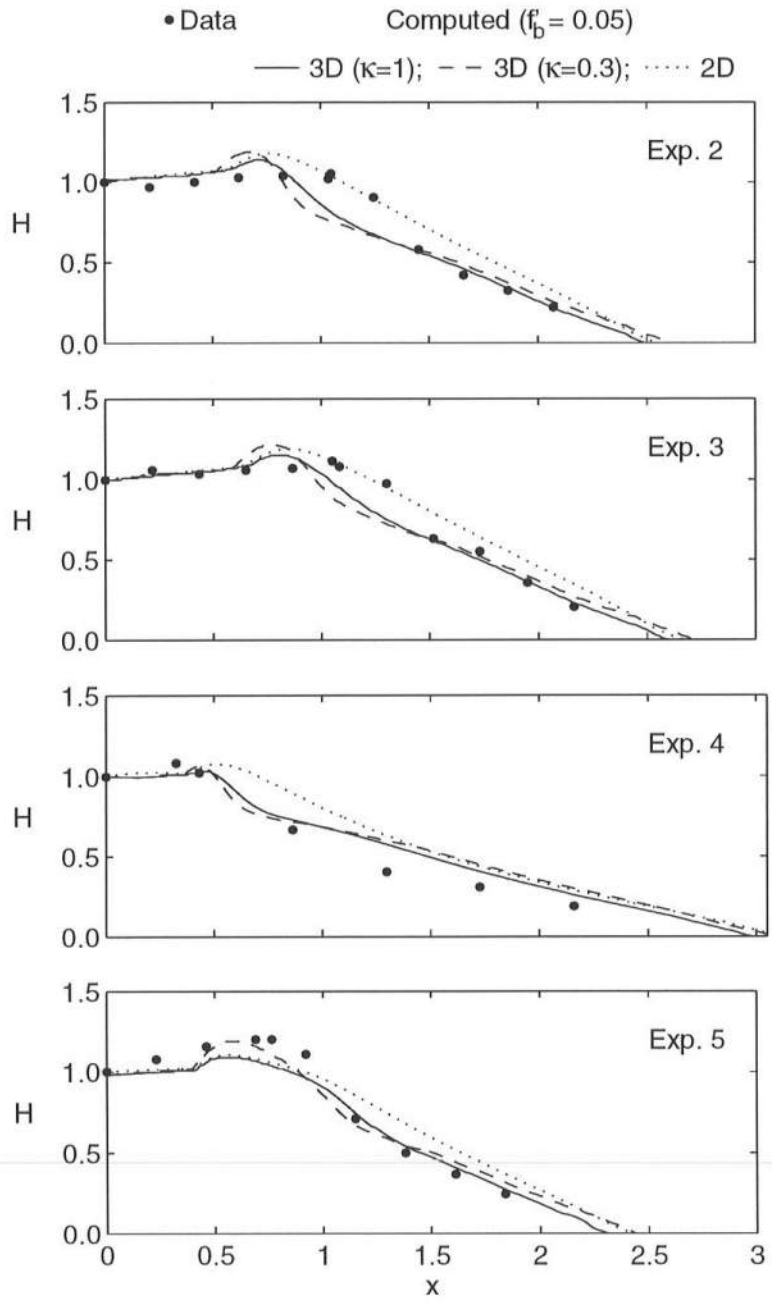

Figure 5.9: Measured and computed wave height H for four experiments using different values of κ for 3D model.

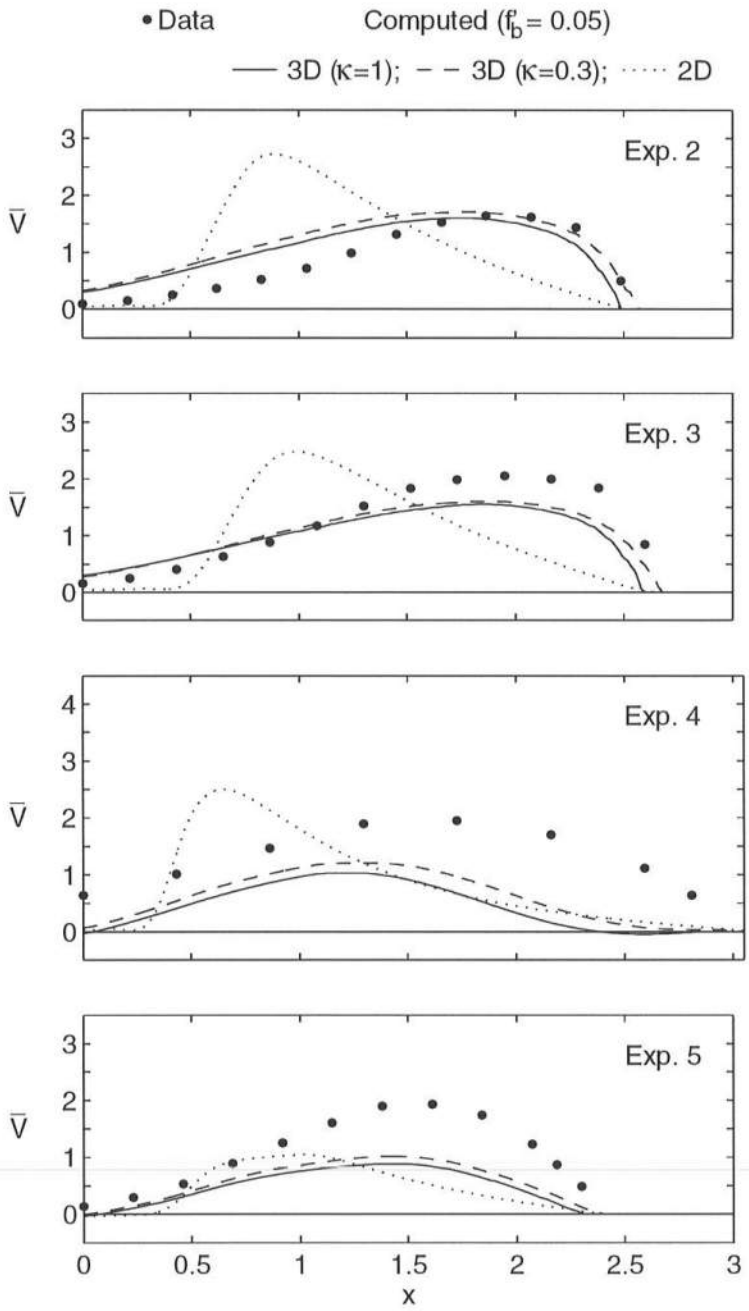

Figure 5.10: Measured and computed depth-averaged longshore current $\overline{V}$ for four experiments using different values of κ for 3D model.

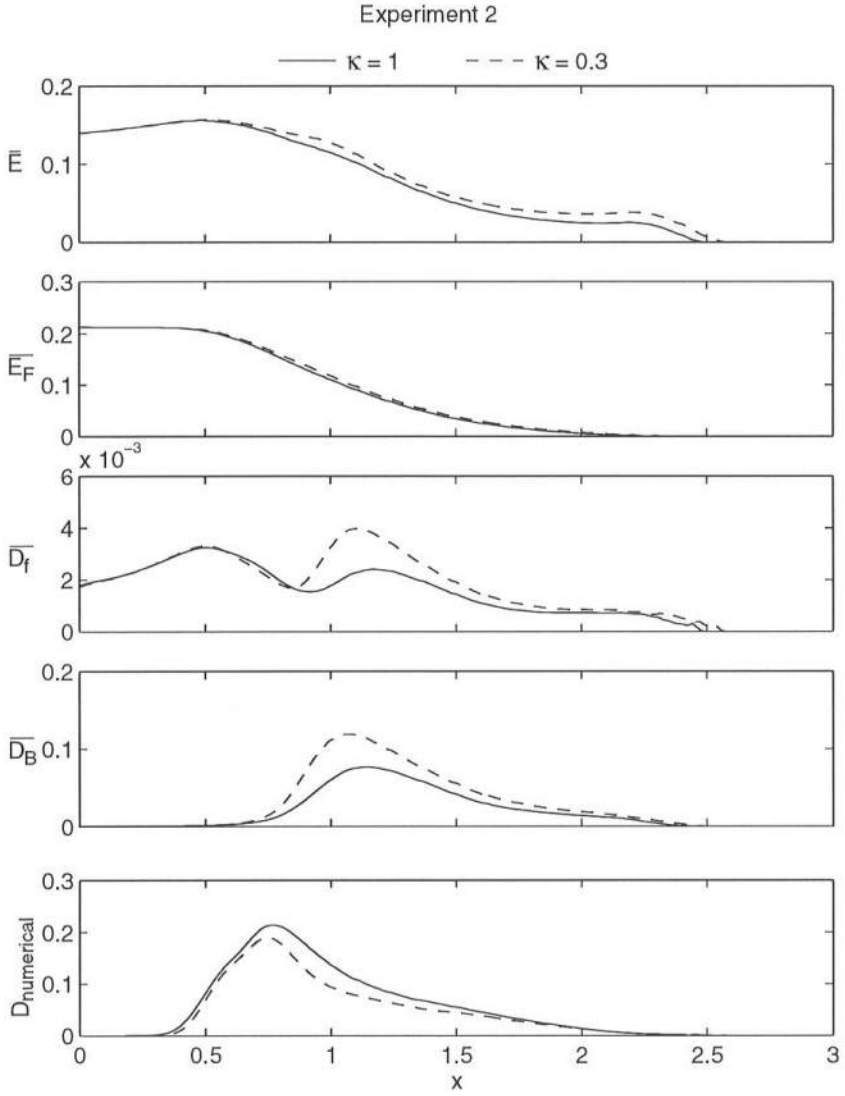

Figure 5.11: Computed cross-shore variations of time-averaged specific energy $\overline{E}$, energy flux $\overline{E_F}$, bottom frictional dissipation rate $\overline{D_f}$, breaking dissipation rate $\overline{D_B}$ predicted physically by 3D model, and numerical dissipation rate $\overline{D}_{\text{numerical}}$ estimated using time-averaged energy equation.

5.1.4 Computed Instantaneous Velocity Field

Figure 5.12 shows the computed cross-shore variations of the free surface η, the depth-averaged cross-shore velocity U, the near-bottom cross-shore velocity correction $\tilde{u}_b$, the depth-averaged alongshore velocity V, and the near-bottom alongshore velocity correction $\tilde{v}_b$ at five time levels throughout the final wave period for experiment 2. The computed cross-shore variations at $t = 299$ and $t = 300$ are identical due to periodicity. The saw tooth profile develops as the wave propagates shoreward. The near-bottom cross-shore velocity correction, $\tilde{u}_b$, is assumed to be out of phase with U in (3.54) to ensure that $|u_b| \leq |U|$ where $u_b = (U + \tilde{u}_b)$ is the near bottom cross-shore velocity. Consequently, the value of $\tilde{u}_b$ computed using (3.54) changes abruptly as U changes its sign. The magnitude of $\tilde{v}_b$ is small in comparison to the magnitude of V, suggesting that the deviation of the alongshore velocity v given by (3.58) from the depth-averaged velocity V is fairly small as is the case with the longshore current $\overline{v}$ shown in Figures 5.6 and 5.7.

5.2 Comparisons with Irregular Wave Data

The 3D computations for the Leadbetter beach data of Thornton and Guza on February 5 and 6 are made in the same way as the corresponding 2D computations in Section 4.3. The bottom friction factor is taken to be $f_b' = 0.015$ for the 2D and 3D computations. The 3D computations are also made using $f_b' = 0.01$.

Figure 5.13 compares the measured and computed cross-shore variations of the normalized root-mean-square wave height H_{rms} on February 5 and 6. The differences between the 2D and 3D computations are less than those shown in Figure 5.2 for the regular waves. The cross-shore variations of H_{rms} computed using $f_b' = 0.01$ are indistinguishable from those shown in Figure 5.13 for $f_b' = 0.015$.

Figure 5.14 shows the computed depth-averaged longshore currents $\overline{V}$ using $f_b' = 0.01$ and 0.015 in comparison with the longshore current measured at a distance

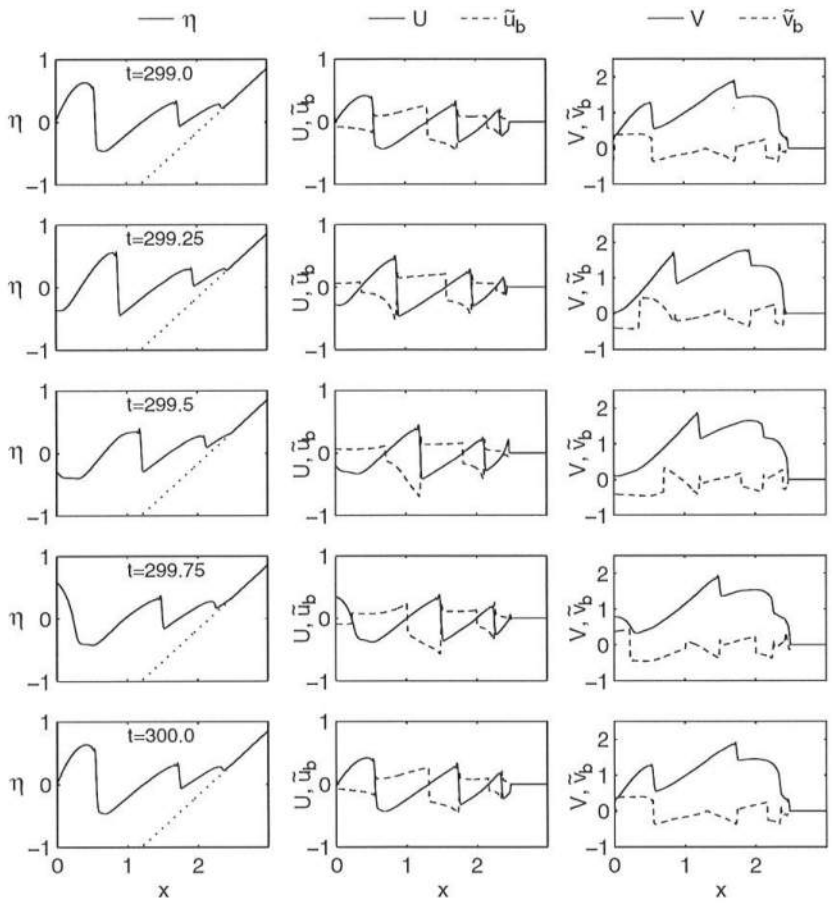

Figure 5.12: Computed cross-shore variations of $\eta, U, \tilde{u}_b, V$, and $\tilde{v}_b$ at 5 time levels, $t = 299.0$, 299.25, 299.5, 299.75, and 300.0 for experiment 2.

above the bottom. These comparisons are meaningful only if the longshore current $\overline{v}$ varies little vertically. Figure 5.15 shows the computed vertical variations of $\overline{v}$ based on $f_b' = 0.01$ at six cross-shore locations on February 5 where $x = 2.56$ and 2.81 are in the swash zone. It is noted that the time-averaged value of $\overline{v}$ at the given distance $(z - z_b)$ from the bottom is computed only if this elevation is wet always during $200 \leq t \leq 500$, whereas the time-averaged value $\overline{v}$ at the given normalized distance $\zeta = (z - z_b)/h$ is computed as long as $\overline{h} > 0$ and plotted at the mean elevation, $(z - z_b) = \zeta\overline{h}$, where $v = 0$ set during $h = 0$ is included in the time averaging. The computed vertical variations of $\overline{v}$ on February 6 are also small and the measured longshore currents may be assumed to represent the depth-averaged longshore currents. It is noted that the vertical variations of $\overline{v}$ for irregular waves in Figure 5.15 are smaller than those for regular waves in Figures 5.6 and 5.7.

Figure 5.14 shows that the dispersion effects included in the 3D model improve the agreement somewhat if the bottom friction factor f_b' is reduced to $f_b' = 0.01$ from $f_b' = 0.015$ used for the 2D model. Moreover, the dispersion effects on the longshore currents induced by breaking irregular waves are secondary in comparison to those shown in Figure 5.4 for regular waves. To confirm this conclusion, Figure 5.16 shows the computed cross-shore variations of dS_{xy}/dx and $d\overline{n}/dx$ on February 5 in the same way as Figure 5.5 for regular waves. The term $d\overline{n}/dx$ included in the 3D model is secondary in the alongshore momentum equation (5.1). Thornton and Guza (1986) already showed that the dispersion or lateral mixing was not important for their longshore current data where the lateral mixing term was based on the eddy viscosity formulation of Longuet-Higgins (1970).

Figure 5.17 shows the time-averaged energy quantities for February 5. Similar to Figure 5.11 for regular waves, the numerical dissipation rate in the 3D model is appreciable relative to the physical dissipation rates $\overline{D_f}$ and $\overline{D_B}$ for irregular waves as well.

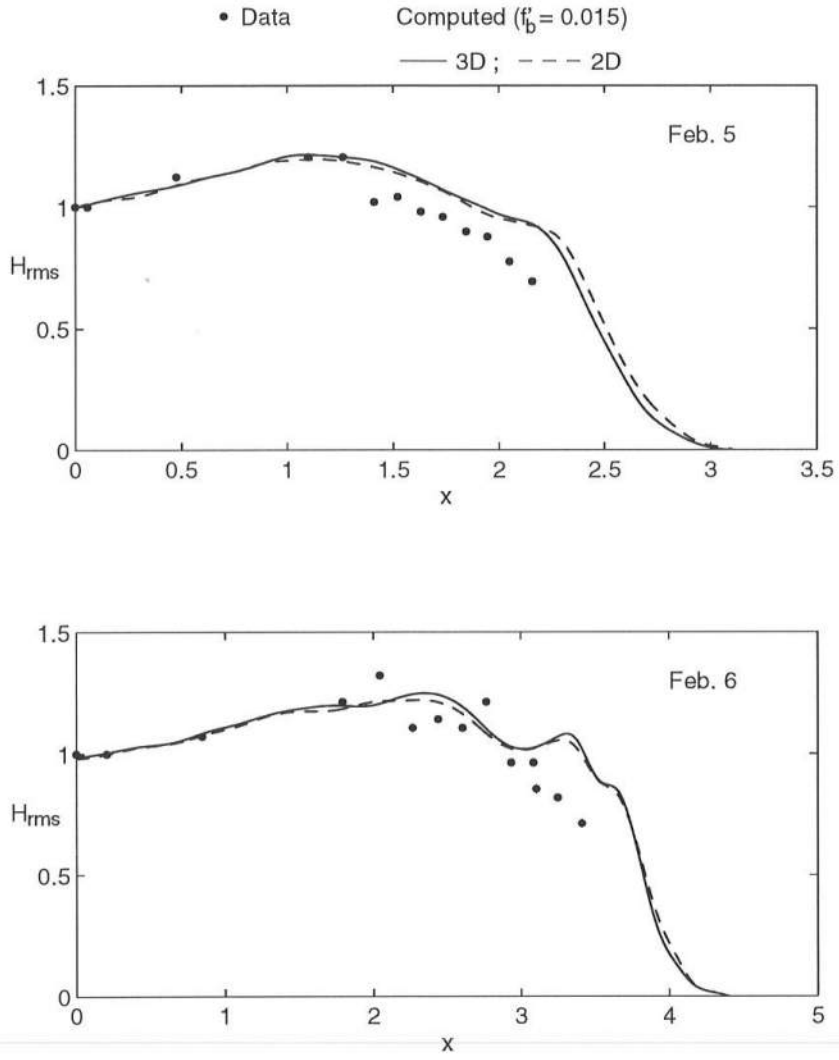

Figure 5.13: Measured and computed root-mean-square wave height H_{rms} on February 5 and 6 for comparison of 2D and 3D models.

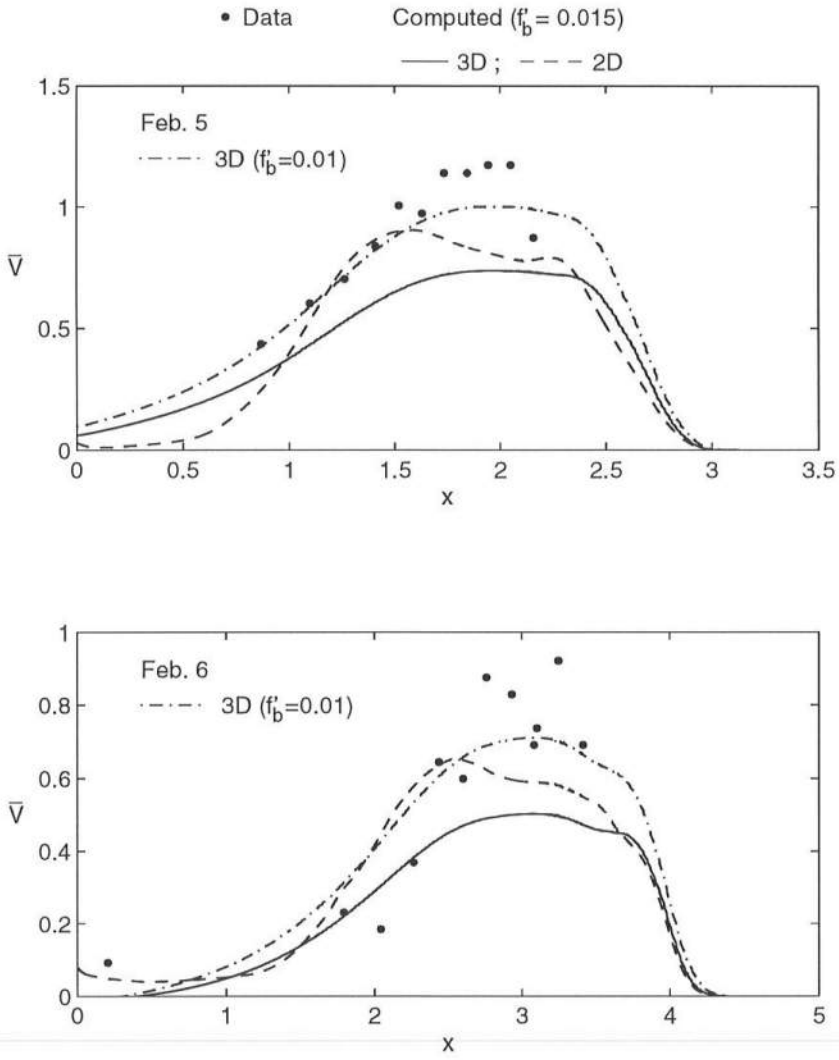

Figure 5.14: Measured and computed depth-averaged longshore current $\overline{V}$ on February 5 and 6 for comparison of 2D and 3D models.

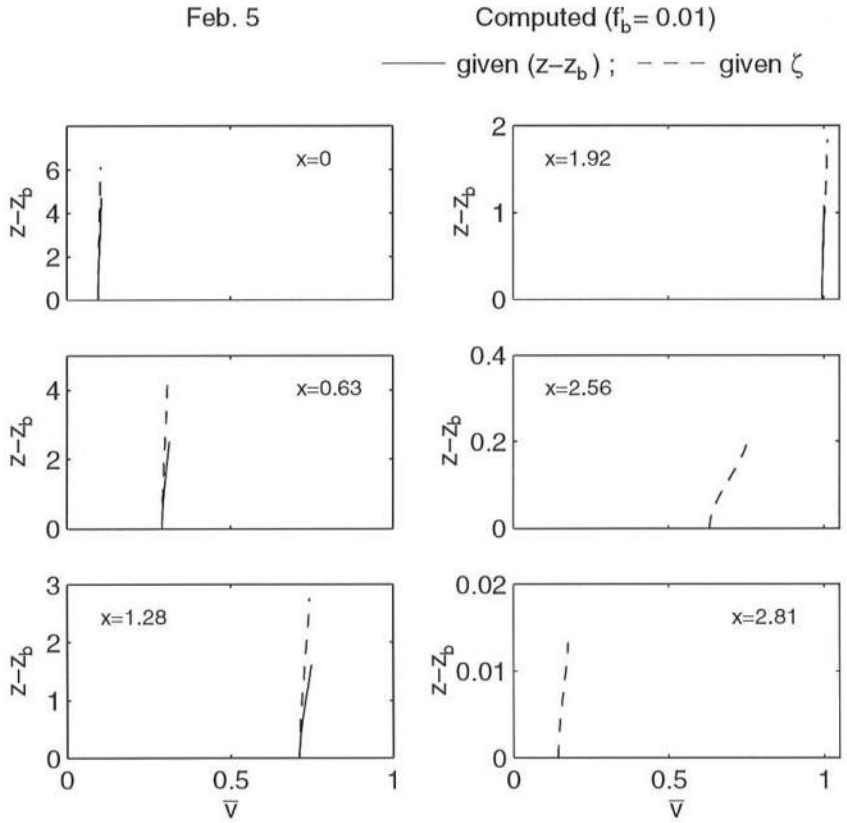

Figure 5.15: Measured and computed vertical variations of longshore current $\overline{v}$ on February 5 for 3D model.

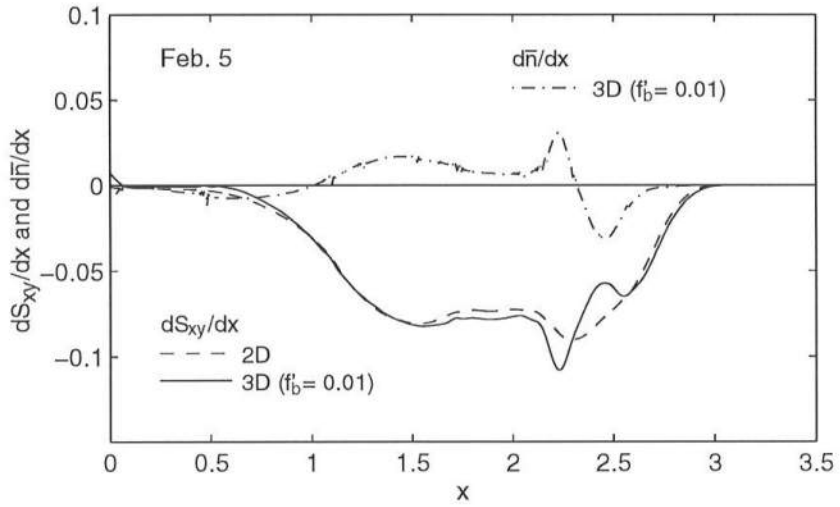

Figure 5.16: Computed cross-shore gradients of S_{xy} and $\overline{n}$ for February 5.

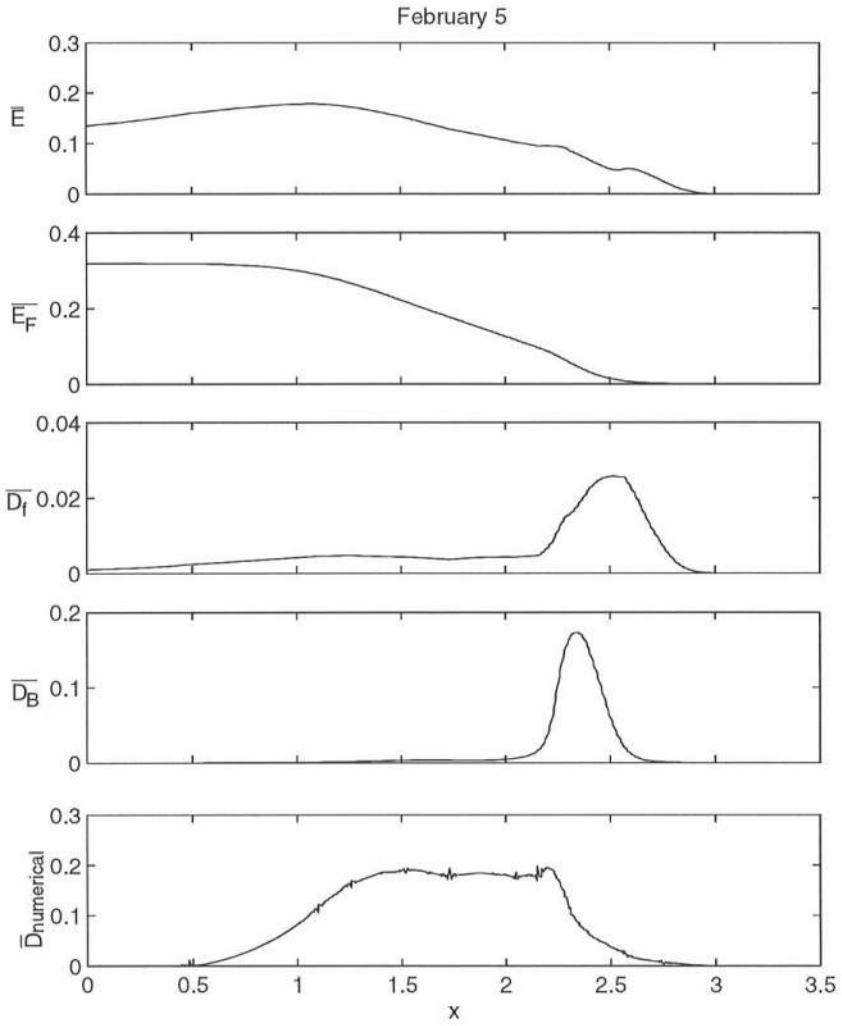

Figure 5.17: Computed cross-shore variations of time-averaged specific energy $\overline{E}$, energy flux $\overline{E_F}$, bottom frictional dissipation rate $\overline{D_f}$, wave breaking dissipation rate $\overline{D_B}$ predicted physically by 3D model, and numerical dissipation rate $\overline{D}_{\text{numerical}}$ estimated using time-averaged energy equation for February 5.

Chapter 6

COMPARISON OF THE 3D MODEL WITH BARRED BEACH DATA

The concept of alongshore radiation stress has been shown to satisfactorily describe the cross-shore distribution of longshore current on a planar beach (*e.g.*, Svendsen and Putrevu 1994). The peak is located near the breaking zone inside the surf zone where the cross-shore gradient of wave height is maximum. For regular waves, horizontal mixing is required for smoothing the current profile, whereas Thornton and Guza (1986) found that for irregular waves, horizontal mixing is not important as a result of the randomness of the breaker locations.

On a barred beach, conceptually, waves will break on the bar, reform and break again on the beach face producing two peaks in the longshore current distribution. Contrary to this concept, the measurements of longshore currents on the barred beach obtained during the Duck Experiment on Low-Frequency and Incident-Band Longshore and Across-shore Hydrodynamics (DELILAH) experiment (Smith *et al.* 1993) generally indicated a broad peak in the bar trough region. Existing time-averaged models for longshore currents, which couple four governing equations for the wave height, wave angle, mean water surface elevation, and longshore current, have not been able to predict these broad peak longshore current data (Smith *et al.* 1993).

Smith *et al.* (1993) developed a one-dimensional time-averaged numerical model for longshore current that included the effect of turbulence due to wave

breaking through a general transport equation for the mean turbulent kinetic energy. Their model improved the model proposed by Larson and Kraus (1991) but produced an unrealistic high peak on the beach face. Church and Thornton (1993) developed a model using a spatially varying bottom friction coefficient based on a one-dimensional turbulent kinetic energy equation associated with the breaking-wave induced turbulence. However, this model was unable to satisfactorily predict the broad peak of the longshore current distribution observed in the DELILAH experiment. Momentum fluxes associated with mass transport above the trough level of broken waves, which were ignored in the other models, were included in the model developed by Kuriyama (1994). His model with additional empirical coefficients was compared with the longshore currents measured at Hazaki Oceanographical Research Facility (HORF) in Japan. At present, there is no model available to predict the broad peak of the longshore current on a barred beach in a physically satisfactory manner.

To assess whether the time-dependent 3D numerical model including the dispersion effects in Section 3.2 is capable of predicting the longshore current on a barred beach, the 3D model is compared with the DELILAH field data of Smith *et al.* (1993). The comparison suggests that the broad peak of the longshore current in the bar trough region cannot be explained under the assumption of alongshore uniformity.

6.1 Estimation of Incident Irregular Waves

The 3D model is compared with the DELILAH data on October 14, 1990 at 1900 EST, which included the cross-shore variations of the measured root-mean-square wave height and longshore current. The frequency spectrum measured at the 8 m water depth was narrow banded in frequency with symmetric directional distributions about a mean oblique wave direction. The wave conditions at the 8 m depth

were: the root-mean-square wave height $H'_{\rm rms} = 0.83$ m; the spectral peak period $T'_p = 12.0$ sec; and the dominant incident wave direction $\theta_i = 18°$. The bathymetry was nearly uniform in the alongshore direction.

The seaward boundary of the numerical model based on the assumption of shallow water waves is taken at the water depth $d' = 3.64$ m below the still water level where the measured root-mean-square wave height $H'_{\rm rms}$ was 1.02 m. The measured frequency spectrum at $d' = 8$ m is used to estimate the assumed unidirectional frequency spectrum and the predominant incident wave direction at $d' = 3.64$ m using the computer program RESHOAL developed by Poff and Kobayashi (1993) as explained in the following.

RESHOAL assumes a straight shoreline with parallel bottom contours. For a given incident directional random wave spectrum at a deeper water depth, RESHOAL computes the directional random wave spectrum at a specified shallow water depth using linear finite-depth wave theory for directional random wave shoaling and refraction (LeMéhauté and Wang 1982). The incident directional random wave spectrum at the deeper water depth $d' = 8$ m is assumed to be given by the product of the TMA frequency spectrum (Bouws *et al.* 1985) and the Mitsuyasu-type directional spreading function (Goda 1985). The input parameters for RESHOAL at the deeper water depth $d' = 8$ m are: $H'_{\rm mo}$ = spectral estimate of significant wave height; T'_p = spectral peak period ($T'_p = 12$ s for this data); γ = spectral peak enhancement factor; θ_i = dominant incident wave direction ($\theta_i = 18°$); $s_{\rm max}$ = maximum value of the spreading parameter. RESHOAL computes the directional spectrum, frequency spectrum and directional spreading function at the shallower water depth $d' = 3.64$ m. The parameters $H'_{\rm mo}$, γ, and $s_{\rm max}$ need to be calibrated such that the root-mean-square of wave height at the 3.64 m depth is equal to the measured value of $H'_{\rm rms}$ =1.02 m and the assumed incident directional wave spectrum at the 8 m water depth is similar to the measured spectrum. The calibrated values are

$H'_{\rm mo}$ = 1.35 m; γ =5; and $s_{\rm max}$=120 at the 8 m water as shown in Figure 6.1. It is noted that the assumption of $H'_{\rm rms} = H'_{\rm mo}/\sqrt{2}$ yields $H'_{\rm rms}$ = 0.95 m for $H'_{\rm mo}$ = 1.35 m, which is slightly larger than the measured value $H'_{\rm rms}$ = 0.83 m.

Figures 6.1 shows the measured and fitted frequency and directional spectra at the 8 m water depth and the computed frequency and directional spectra at the seaward boundary d' = 3.64 m. The fitted directional spectrum at the 8 m depth is the TMA frequency spectrum with γ = 5 and $H'_{\rm mo}$ = 1.35 m with the Mitsuyasu-type directional spreading function with $s_{\rm max}$ = 120. The computed frequency spectrum with T'_p = 11.9 s at d' = 3.64 m is used to compute the incident wave trains at the seaward boundary using (4.3) required as the input to the 3D model. This incident frequency wave spectrum does not include low-frequency wave components as shown in Figure 6.1. The computed dominant incident wave direction is $\theta_i = 12°$ at d' = 3.64 m as may be seen from the computed directional spectrum at d' = 3.64 m in Figure 6.1 which suggests that the assumption of unidirectional random waves may be reasonable.

Similar to the computations made in Chapters 4 and 5, the normalized computation duration is taken as $t_{\rm max}$ = 500 corresponding to $t'_{\rm max} \simeq$ 99 min. The sampling rate $\Delta t'_s$ in (4.3) is taken to be the same as the sampling rate of the field data, $\Delta t'_s$ = 0.125 s. The bottom friction factor is assumed to be f'_b =0.015. The computed results presented in the following section are based on the normalization using the wave conditions at the seaward boundary of d' = 3.64 m, *i.e.*, the measured root-mean-square wave height $H' = H'_{\rm rms}$ = 1.02 m; the computed spectral peak period $T' = T'_p$=11.9 sec; and the computed dominant wave direction θ_i = 12°. Correspondingly, $\sigma = T'(g/H')^{\frac{1}{2}}$ = 37 and $\theta_c = \theta_i$ = 0.21 in radians. The assumptions of $\sigma^2 \gg 1$ and $\theta_c^2 \ll 1$ are satisfied for this data. The normalized grid spacings are taken as $\Delta x \simeq \Delta y$ = 0.0106 corresponding to the dimensional cross-shore and alongshore grid spacings of $\Delta x'$ = 0.40 m and $\Delta y'$ = 1.91 m, respectively.

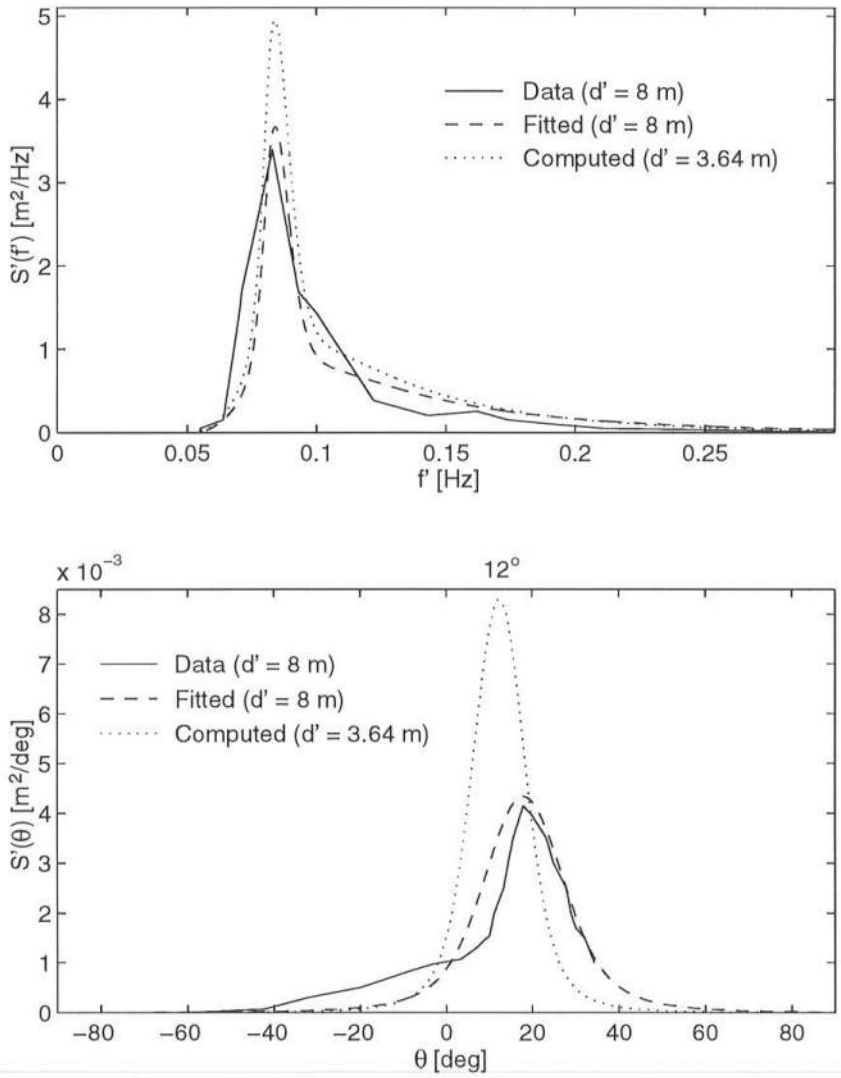

Figure 6.1: Measured and fitted frequency and directional spectra at the deeper depth $d' = 8$ m and the shoaled and refracted frequency and directional spectra at the shallower depth $d' = 3.64$ m.

6.2 Comparison with Measurements

Figure 6.2 shows the comparisons between the measured and computed cross-shore variations of the local root-mean-square wave height $H_{\rm rms}$ and the longshore current $\overline{V}$ together with the measured bottom profile. The computed temporal variation of η for $200 \leq t \leq 500$ is used to obtain $H_{\rm rms}$ based on the zero-up crossing method whereas the computed longshore current $\overline{V}$ is obtained by averaging the temporal variation of the depth-averaged alongshore velocity V for the duration $200 \leq t \leq 500$.

Figure 6.2 shows that the 3D model without the incident low-frequency wave components underpredicts the root-mean-square wave height in the bar trough region. Moreover, the model predicts a peak in the longshore current at the seaward edge of the bar crest in contrast to a broad peak in the bar trough region.

The computed cross-shore variations of the time-averaged energy quantities in (3.63) are shown in Figure 6.3. The dissipation due to bottom friction $\overline{D_f}$ has a peak near the shoreline where the oscillatory cross-shore velocity is large. The dissipation rate due to wave breaking, $\overline{D_B}$, shown in the fourth panel has peaks near the bar crest and on the beach face where the waves break. The numerical dissipation rate shown in the last panel is dominant over the physical dissipation rates computed explicitly in the 3D model and is the maximum at the seaward edge of the bar crest. This numerical dissipation rate appears to compensate for the underpredicted value of $\overline{D_B}$ at the bar crest.

Figure 6.4 shows the computed cross-shore variations of dS_{xy}/dx and $d\overline{n}/dx$ in the alongshore momentum equation (5.1). The dispersion term $d\overline{n}/dx$ is secondary in comparison to the cross-shore gradient of the alongshore radiation stress, dS_{xy}/dx. The driving force represented by dS_{xy}/dx is small in the bar trough region.

As an attempt to explain the broad peak in the longshore current distribution, the effects of incident low-frequency waves and alongshore non-uniformity of incident

wind waves on the cross-shore distribution of longshore current are examined in the subsequent sections.

6.3 Effects of Incident Low-Frequency Waves

The incident wave spectrum at the seaward boundary shown in Figure 6.1 does not include low-frequency components. The low-frequency components might modify wave breaking on the bar crest and improve the agreement of the longshore current profile. As a first approximation, uniform low-frequency components are added to the incident wave spectrum as shown in Figure 6.5. The additional energy of these low-frequency components is taken to be 4% and 20% of the energy of the wind wave frequency components to examine the sensitivity of the computed results to the amount of the low-frequency components. It is noted that the 20% low-frequency component at the 3.64 m depth are expected to be too large in reality.

The measured and computed cross-shore variations of the root-mean-square wave height and longshore current are compared in Figure 6.6. The agreement for the root-mean-square wave height is improved somewhat but the additional low-frequency components modify the longshore current profile little. Consequently, the broad peak of the longshore current in the bar trough cannot be explained by incident low-frequency waves.

6.4 Effects of Alongshore Non-Uniformity of Incident Wind Waves

Longshore currents have been primarily modeled assuming alongshore uniformity, although it has been known that alongshore non-uniformities affect longshore currents. Putrevu *et al.* (1995) derived a semi-analytical solution for longshore current that allows for weak alongshore variation in the bottom topography. Their calculation showed that the longshore current could deviate by up to 30% from the mean for a 10% deviation of the bottom topography. Symonds and Huntley (1980) showed that the alongshore gradient of wave setup can shift the peak of the long-

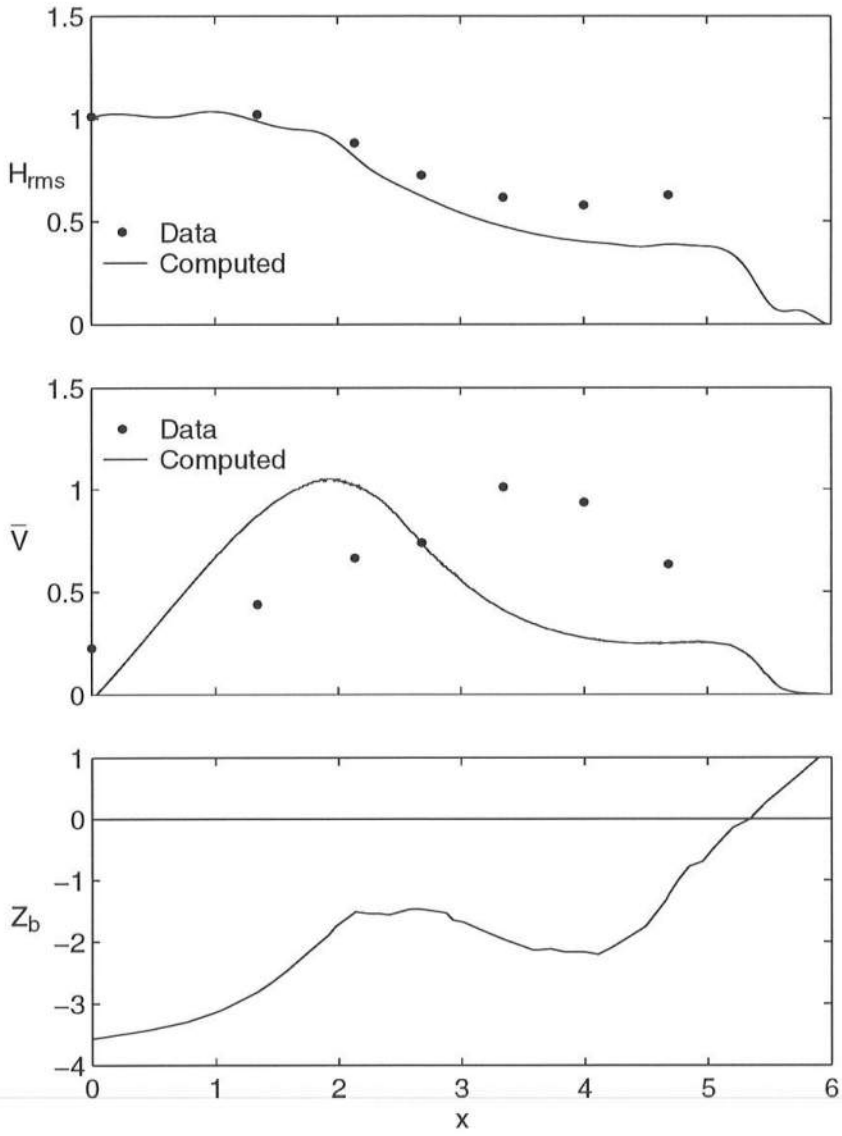

Figure 6.2: Measured and computed cross-shore variations of root-mean-square wave height H_{rms} and longshore current $\overline{V}$ together with normalized bottom profile for DELILAH experiment.

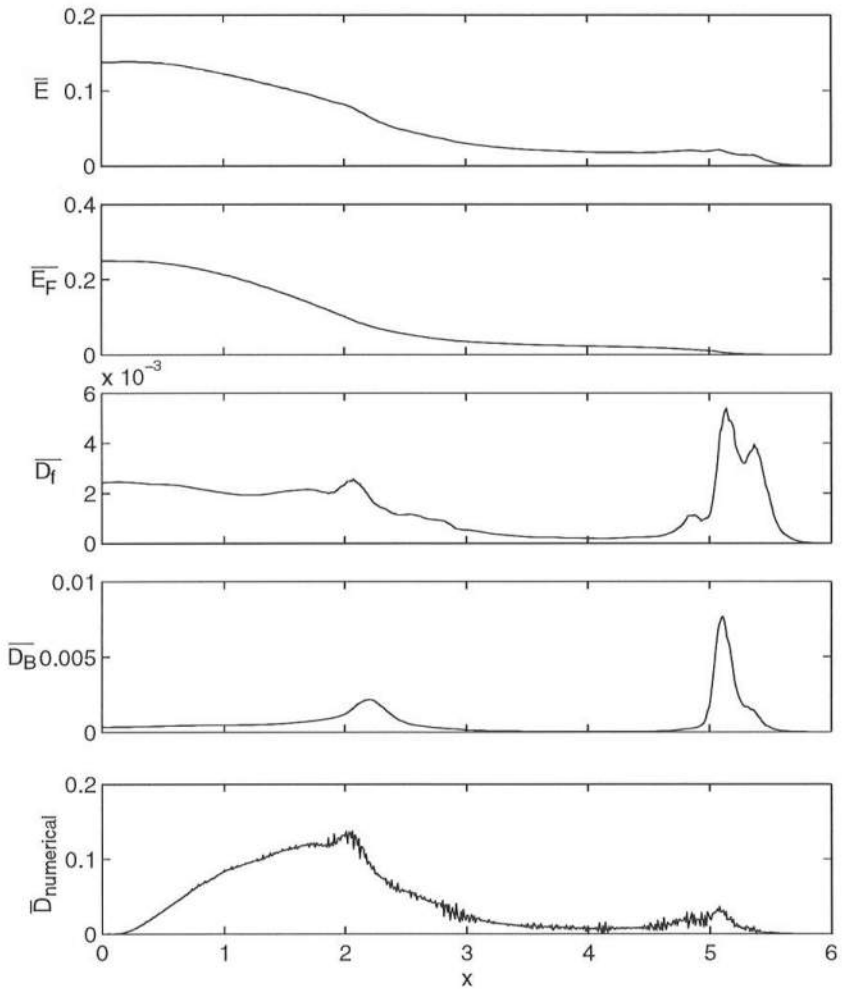

Figure 6.3: Computed cross-shore variations of time-averaged specific energy $\overline{E}$, energy flux $\overline{E_F}$, bottom frictional dissipation rate $\overline{D_f}$, wave breaking dissipation rate $\overline{D_B}$ predicted physically by 3D model, and numerical dissipation rate $\overline{D}_{\text{numerical}}$ estimated using time-averaged energy equation.

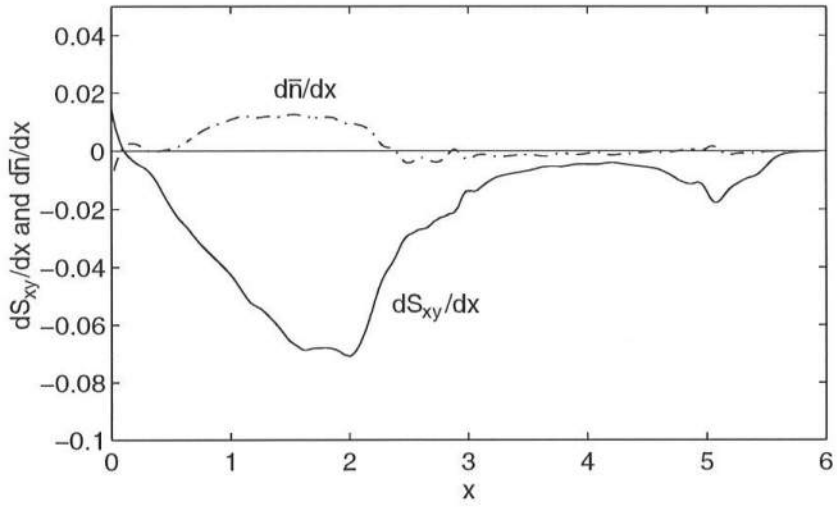

Figure 6.4: Computed cross-shore variations of dS_{xy}/dx and $d\overline{n}/dx$ for barred beach.

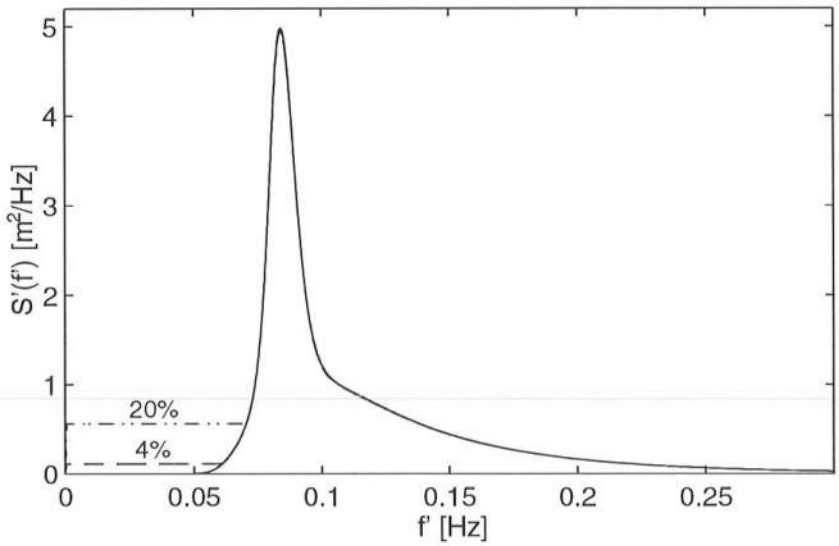

Figure 6.5: Incident wave frequency spectrum at the seaward boundary including the 4% and 20% low-frequency components.

shore current shoreward. Gourlay (1976), Keeley and Bowen (1977), and Wu *et al.* (1985) studied the effect of the alongshore variation of breaker height on the longshore current. Gourlay (1976) conducted experiments in a laboratory to study a non-uniform longshore current system generated by the alongshore gradient of breaker height behind an offshore breakwater. Keeley and Bowen (1977) measured the longshore currents in Martinique Beach, Canada at several alongshore locations and found that alongshore variation in the breaker height contributed about 10% to the overall current strength. Wu *et al.* (1985) compared their two-dimensional circulation model with the Nearshore Sediment Transport Study (NSTS) field measurements at Leadbetter Beach, California and demonstrated that the non-uniform wave field resulted in the formation of a non-uniform longshore current pattern.

To study the effect of the alongshore variation of incident wave conditions within the limitation of the 3D model based on three cross-shore lines shown in Figure 3.1, the incident wave trains η_i specified as new input to the model are modified as follows:

$$\begin{aligned} \text{Line 1:} \quad \text{new } (\eta_i)_1 &= \text{old } (\eta_i)_1 \\ \text{Line 2:} \quad \text{new } (\eta_i)_2 &= \text{old } (\eta_i)_2 \times (1 - \delta_\eta) \\ \text{Line 3:} \quad \text{new } (\eta_i)_3 &= \text{old } (\eta_i)_3 \times (1 - 2\,\delta_\eta) \end{aligned}$$

where the old time series $(\eta_i)_1, (\eta_i)_2$ and $(\eta_i)_3$ have been computed using (4.3) for incident unidirectional random waves of alongshore uniformity. The distance between two adjacent lines is $\Delta y' = 1.91$ m. The dimensionless parameter δ_η is taken to be much less than unity to satisfy the assumption of gradual alongshore variation. The incident wave intensity decreases or increases in the down-wave direction depending on $\delta_\eta > 0$ or $\delta_\eta < 0$, respectively.

The computed results using these new incident wave trains are shown in Figures 6.7 and 6.8 for the cases of $\delta_\eta = 0$, 0.0005 and 0.001 and for the cases of $\delta_\eta = 0$ and -0.001, respectively. The root-mean-square wave height changes very

little since the specified change in the incident wave train is very small. For the wave intensity decreasing in the down-wave direction, the longshore current profile increases almost uniformly across the shoaling region and over the bar crest. The increase in the longshore current is larger in the bar trough region, whereas the increase is smaller in the swash zone. The broad peak in the bar trough region is similar to the broad peak observed in the field. For the wave intensity increasing in the down-wave direction as shown in Figure 6.8 the longshore current in the bar trough region is decreased significantly and becomes negative.

To explain the computed results in Figures 6.7 and 6.8, the time-averaged alongshore momentum equation (3.61) is rewritten as

$$\frac{\partial}{\partial x}S_{xy} + \frac{\partial \overline{n}}{\partial x} + \overline{h}\frac{\partial \overline{\eta}}{\partial y} + \frac{1}{2}\frac{\partial}{\partial y}\overline{(\eta - \overline{\eta})^2} = \overline{\tau}_{by} \tag{6.1}$$

in which $S_{xy} = \overline{hUV}$ is the alongshore radiation stress based on the depth-averaged velocities U and V. Figure 6.9 shows the cross-shore variations of the driving forces on the left hand side of (6.1) for the cases of $\delta_\eta = 0.001$ and -0.001. The terms of $\partial\overline{n}/\partial x$ and $\frac{1}{2}\partial\overline{(\eta - \overline{\eta})^2}/\partial y$ are on the order of 0.005 or less in the bar trough region and secondary in comparison to the other two terms plotted in this figure. For both cases, the cross-shore gradient of the alongshore radiation stress, $\partial S_{xy}/\partial x$, driving the longshore current is very small in the bar trough region. The additional term $\overline{h}\partial\overline{\eta}/\partial y$ associated with the alongshore wave setup gradient modifies the driving force significantly in the bar trough region. The incident wave intensity and resulting wave setup decrease or increase in the down wave direction depending on $\delta_\eta > 0$ or $\delta_\eta < 0$, respectively.

Figures 6.10 and 6.11 show the computed vertical variations of the longshore current $\overline{v}$ for the alongshore uniform case ($\delta_\eta = 0$) and the non-uniform case ($\delta_\eta = 0.001$), respectively, computed in the same way as for the planar beach case discussed in Section 5.2. Similar to the computed results for irregular waves on the planar beach shown in Figure 5.15, the computed vertical variations of $\overline{v}$ are

very small. However, the longshore currents measured at the same barred beach by Haines and Sallenger (1994) showed marked vertical variations, which cannot be explained by the present 3D model.

To examine the effects of the alongshore non-uniformity on planar beaches, the modified incident wave trains for the cases of $\delta_\eta = 0.0005$ and 0.001 are also specified for the computations for the regular wave experiment 2 of Visser (1991) and the irregular wave data of Thornton and Guza (1986) on February 5. For the planar beach as shown in Figure 6.12, the longshore current increases almost uniformly in the shoaling and surf zones except in the swash zone. Contrary to the computed results for the barred beach shown in Figure 6.7, the longshore current profile shape on the planar beaches is not sensitive to the alongshore non-uniformity. To explain this difference, Figure 6.13 shows the cross-shore variations of the driving forces in the time-averaged momentum equation (6.1) for both regular and irregular waves on the planar beaches. The additional driving force terms $\overline{h}\partial\overline{\eta}/\partial y$ and $\frac{1}{2}\partial\overline{(\eta-\overline{\eta})^2}/\partial y$ due to the alongshore variations are small in comparison to the main driving force, $\partial S_{xy}/\partial x$, causing the almost uniform increase in the longshore current without changing its shape as shown in Figure 6.12. The computed results discussed above imply that the broad peak of the longshore current on a barred beach can be caused by the very small alongshore variation of wave height and setup. This may explain why existing longshore current models based on the assumption of alongshore uniformity were regarded to be adequate before their comparisons with the barred beach data. For planar beaches, the effect of alongshore non-uniformity, even if it exists, can be accounted for by adjusting the constant bottom friction factor that does not change the longshore current profile shape as shown in Figures 5.4 and 5.14. On the other hand, for barred beaches, the very small alongshore variation of wave height and setup modifies the longshore current profile shape that cannot be changed much by adjusting the constant bottom friction factor.

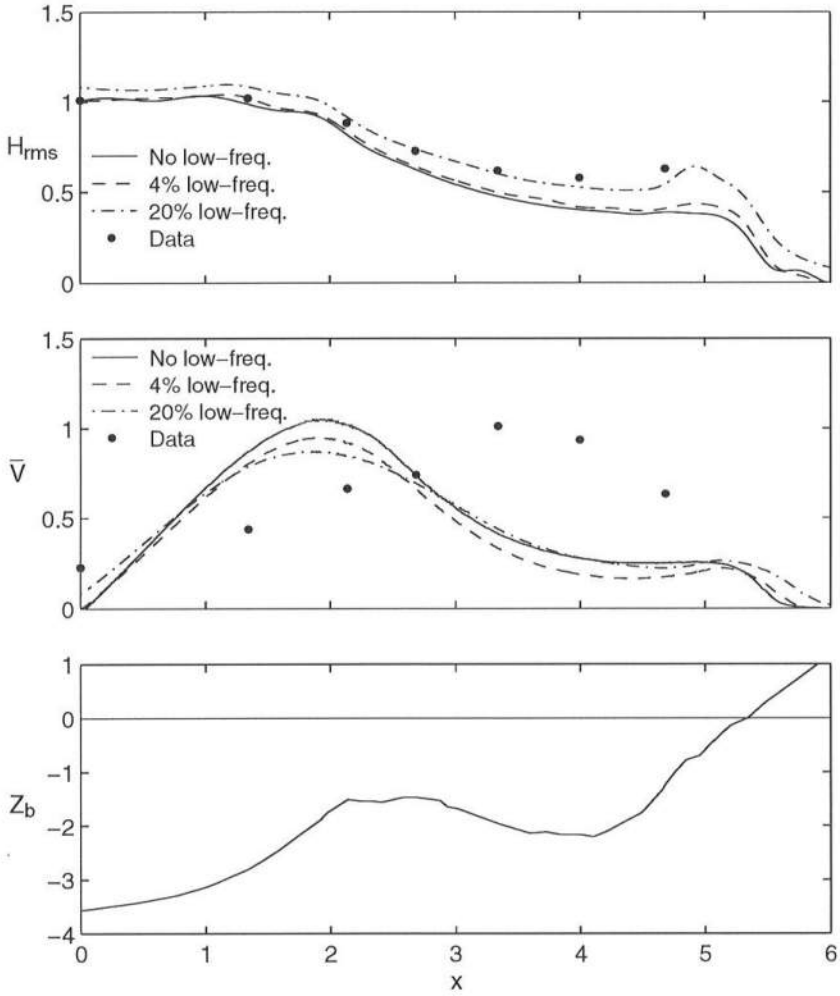

Figure 6.6: Effects of low-frequency wave components on the cross-shore variations of the root-mean-square wave height H_{rms} and longshore current $\overline{V}$ for barred beach.

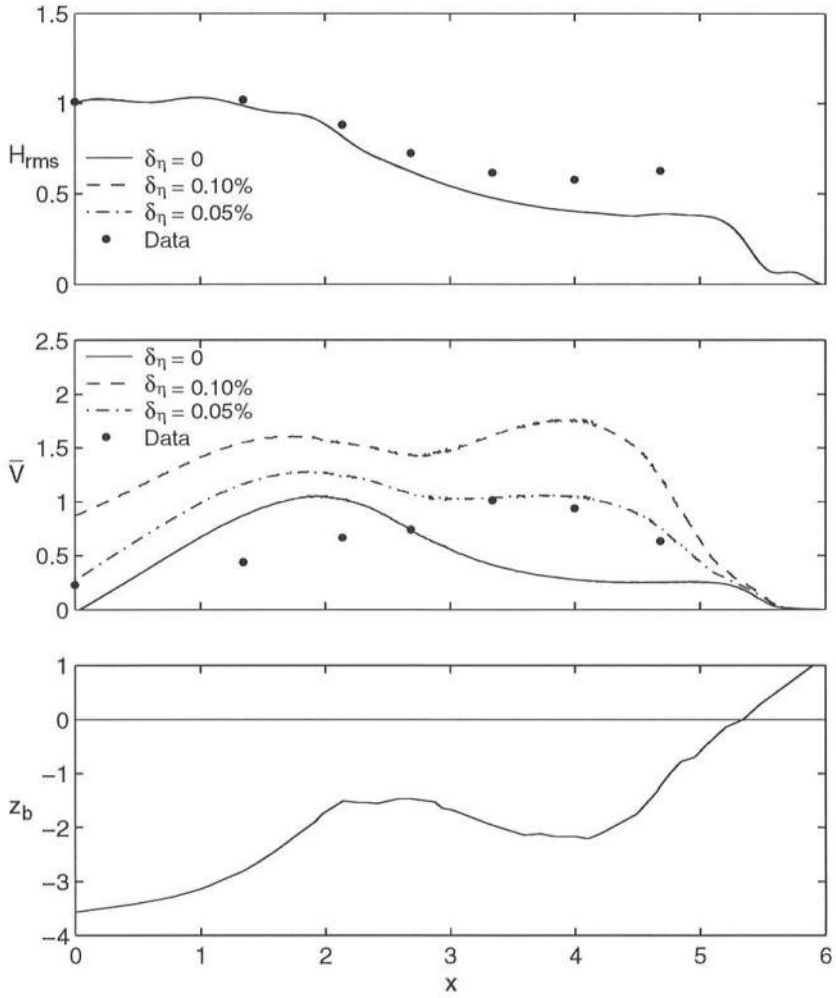

Figure 6.7: Effects of alongshore decrease of incident wave intensity on cross-shore variations of root-mean-square wave height $H_{\rm rms}$ and longshore current $\overline{V}$ for barred beach.

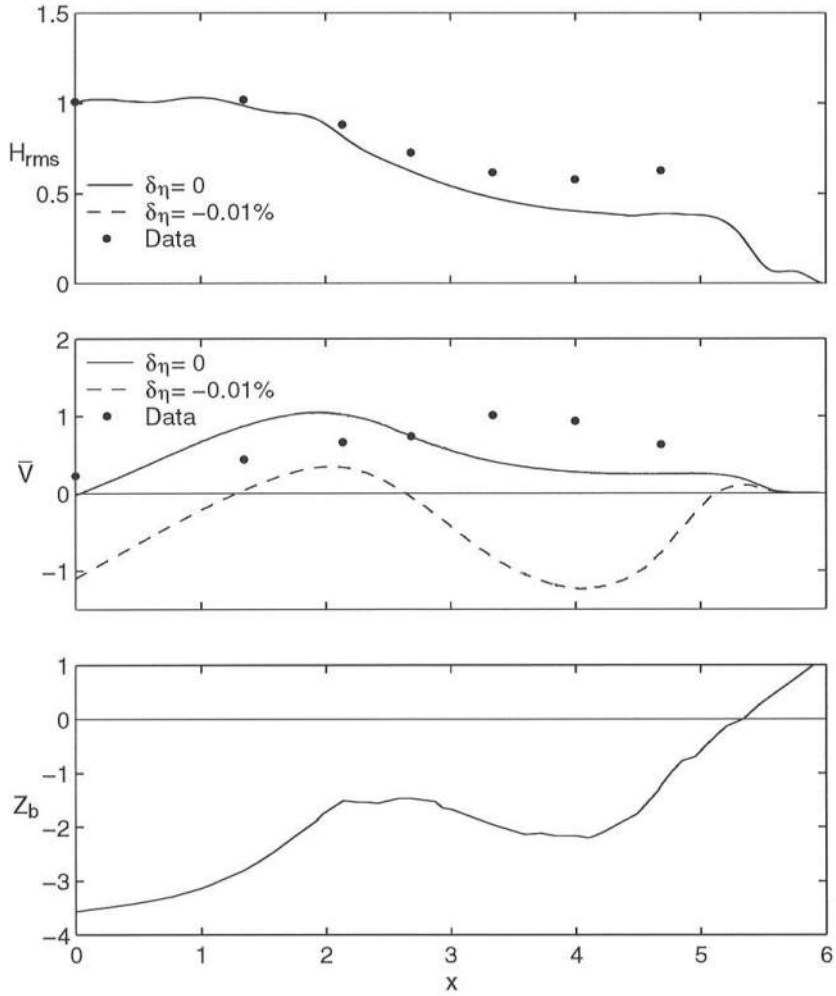

Figure 6.8: Effects of alongshore increase of incident wave intensity on cross-shore variations of root-mean-square wave height $H_{\rm rms}$ and longshore current $\overline{V}$ for barred beach.

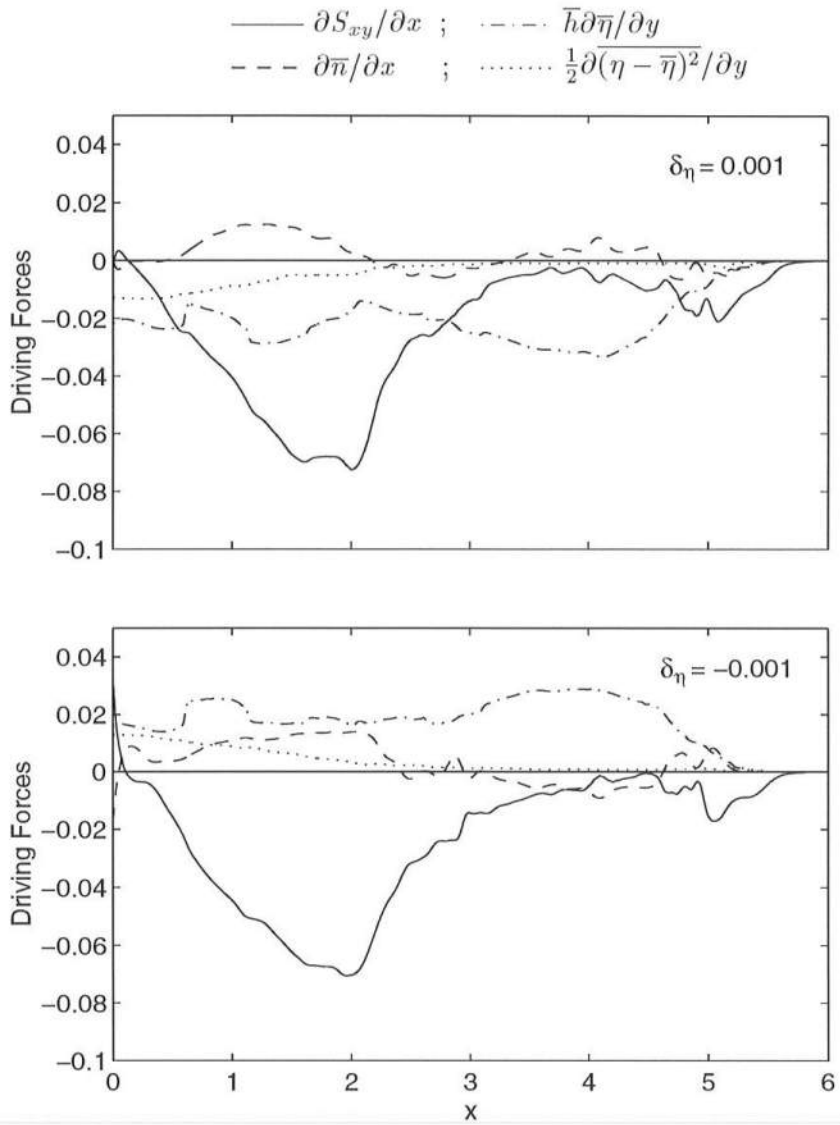

Figure 6.9: Computed cross-shore variations of driving forces in time-averaged alongshore momentum equation (6.1) for $\delta_\eta = 0.001$ with $\partial\overline{\eta}/\partial y < 0$ (wave setup decreasing in down-wave direction) and for δ_η=-0.001 with $\partial\overline{\eta}/\partial y > 0$.

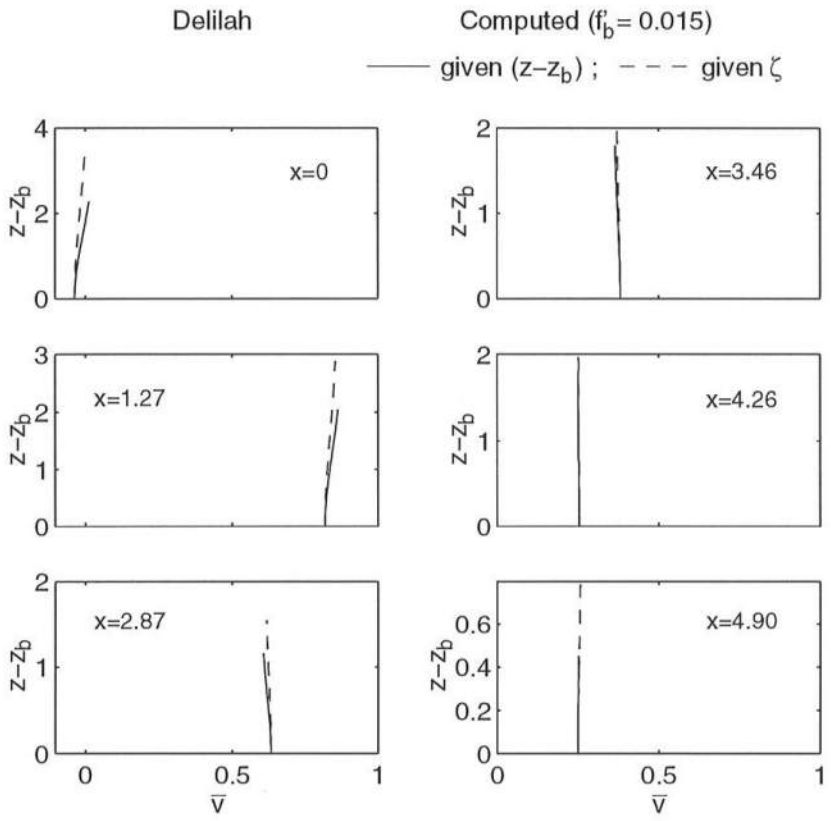

Figure 6.10: Computed vertical variations of longshore current $\overline{v}$ for alongshore uniform case ($\delta_\eta = 0$) for barred beach.

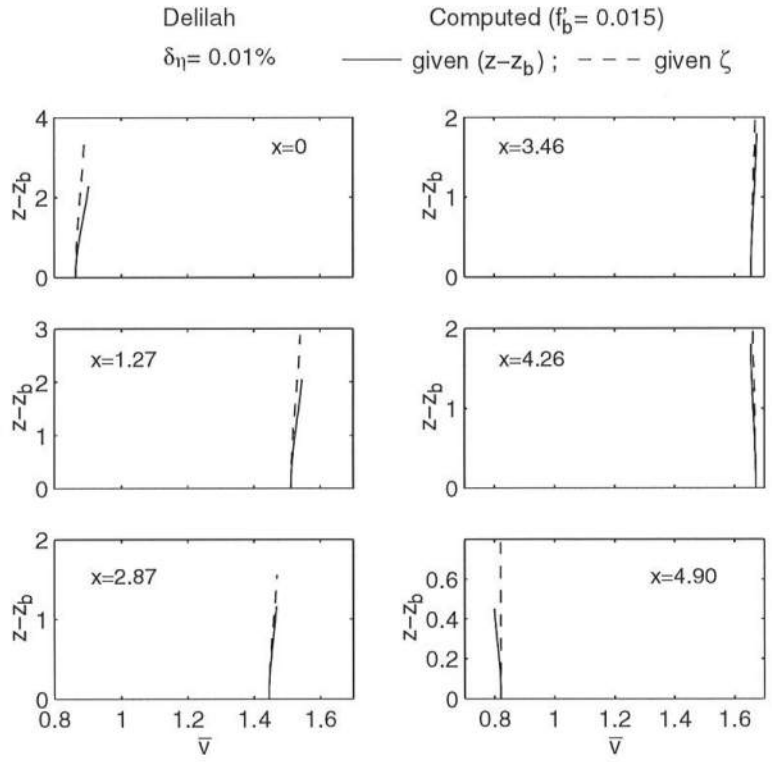

Figure 6.11: Computed vertical variations of longshore current $\overline{v}$ for alongshore non-uniform case ($\delta_\eta = 0.001$) for barred beach.

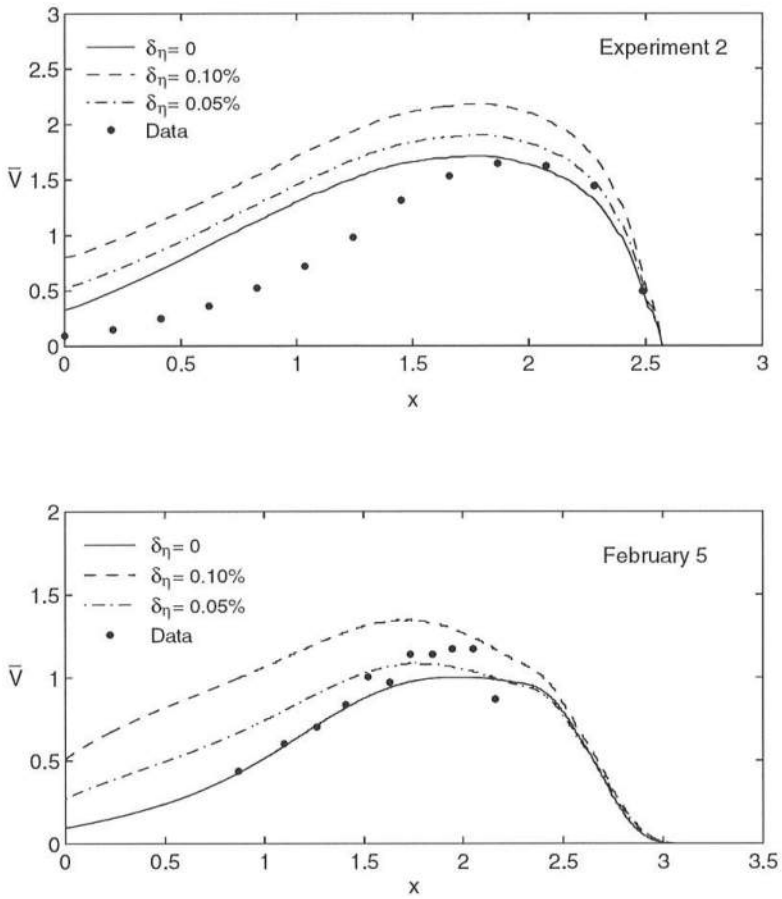

Figure 6.12: Effects of alongshore decrease of incident wave intensity on the longshore current profile for planar beaches.

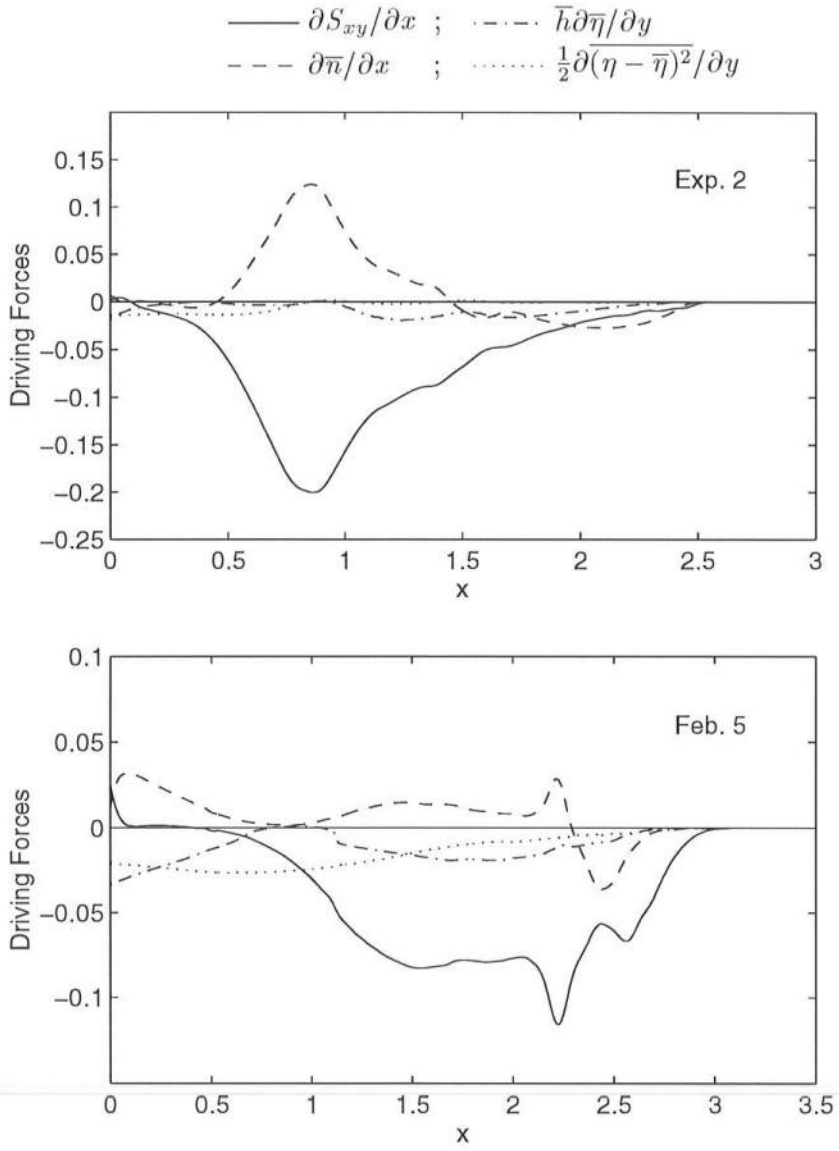

Figure 6.13: Computed cross-shore variations of driving forces in time-averaged alongshore momentum equation (6.1) for planar beaches.

Chapter 7

SUMMARY AND CONCLUSIONS

The finite-amplitude shallow-water equations under the assumption of small incident angles are solved numerically to predict the cross-shore and temporal variations of the free surface elevation and the cross-shore and alongshore velocities in the swash and surf zones. The use of the finite-amplitude shallow-water equations limits the computation domain within a short distance from the shoreline. The assumption of small incident angles reduces computational efforts considerably and avoids difficulties associated with lateral boundary conditions. This assumption may be too restrictive for field applications but allows us to compute the dominant cross-shore fluid motion along each cross-shore line using the one-dimensional continuity and cross-shore momentum equations for normally incident waves developed by Kobayashi *et al.* (1987, 1989).

The secondary alongshore velocity, which may vary slowly in the alongshore direction, is then computed using the alongshore momentum equation for the computed free surface elevation and cross-shore velocity along the cross-shore lines. The time-averaged alongshore momentum equation is used to check the accuracy of the numerical method as well as the seaward and landward boundary algorithms employed to solve the time-dependent alongshore momentum equation.

Two models are developed in this study. The 2D model neglects the vertical variations of the instantaneous horizontal velocities, whereas the quasi-3D model includes the dispersion effects due to the vertical variations of the horizontal veloci-

ties on the depth-integrated cross-shore and alongshore momentum equations (3.47) and (3.48). The dispersion terms m and n in these equations express the additional cross-shore and alongshore momentum fluxes, respectively. It is noted that for the 2D model, $m = 0$ and $n = 0$. Two additional equations for m and n are derived from the depth-dependent cross-shore and alongshore momentum equations. To close the problem, the deviations of the horizontal velocities from the depth-averaged velocities are assumed to be expressed by the cubic profile normalized by the near-bottom deviations and the instantaneous water depth. The equations for m and n are solved numerically together with the cross-shore and alongshore momentum equations to compute the temporal and cross-shore variations of the water depth and the cross-shore and alongshore depth-averaged and near bottom velocities.

The developed 2D and quasi-3D models are compared with the laboratory data for obliquely incident regular waves of Visser (1991), who ensured the alongshore uniformity of longshore currents using a pumping system, and with field data of Thornton and Guza (1986) for that the assumption of alongshore uniformity appeared reasonable. To assess the importance of the dispersion effects, both models are compared with the same data sets. Comparisons between the measured and computed cross-shore variations of the wave height and setup for regular waves and the root-mean-square wave height for irregular waves indicate that both models are capable of predicting these time-averaged quantities. The dispersion effects on the cross-shore variations of the wave height and setup are shown to be minor, indicating that the cross-shore dispersion term m may be neglected in the depth-integrated cross-shore momentum equation as anticipated by Kobayashi and Wurjanto (1992).

The computed oscillatory components of the cross-shore and alongshore depth-averaged velocities become the maximum near the still water shoreline for the field data of Thornton and Guza (1986), contrary to the conventional assumption of depth-limited linear breaking waves made in existing time-averaged models. The

causes of these large velocities are examined using the time-averaged wave energy equation and filtering the computed temporal variations in the high- and low-frequency bands. The computed energy dissipation rate indicates intense wave breaking immediately seaward of the still water shoreline that may partly explain the computed large velocities near the shoreline. The computed high- and low-frequency components of the alongshore velocity variance are of the same magnitude near the shoreline even in the absence of incident low frequency waves and edge waves. Kobayashi *et al.* (1997) derived simple relationships between the free surface and cross-shore velocity statistics using a linear progressive long-wave theory. The computed values of the normalized free surface standard deviation, $\eta_{\rm rms}/\overline{h}$, increase gradually and then rapidly near the shoreline as the mean water depth $\overline{h}$ approaches zero. The computed landward increases of the cross-shore velocity standard deviation and the undertow magnitude can be explained using these relationships with the computed cross-shore variation of $\eta_{\rm rms}/\overline{h}$.

For regular waves, the 2D model with the bottom friction factor calibrated previously for swash oscillations predicts the magnitude of the longshore current but cannot reproduce the longshore current profile. The quasi-3D model, which includes the dispersion effects, improves the prediction of the longshore current profile significantly. For irregular waves, both models using the bottom friction factor calibrated by Raubenheimer *et al.* (1995), predict the longshore current profile as accurately as the calibrated time-averaged model by Thornton and Guza (1986), which requires much less computational efforts. The advantage of the time-dependent models can not be confirmed for lack of swash velocity data. The 3D model computation is also made using different values of the bottom friction factor to improve the agreement of the longshore current. The bottom friction factor is important in determining the magnitude of the longshore current but modifies its profile little. In summary, the dispersion effects on the longshore current profile are

significant for regular waves but secondary for irregular waves, especially in view of the uncertainties associated with the bottom friction factor. Furthermore, the 3D model is shown to predict the vertical variations of the longshore current inside the surf zone but not outside the surf zone since the assumed cubic velocity profile may not be appropriate outside the surf zone.

The computed results using the 2D model are used to explain the very low-frequency component of the computed depth-averaged alongshore velocities V generated by irregular breaking waves. The oscillatory components of the computed alongshore velocity are analyzed using the nonlinear and linear alongshore momentum equations together with the computed alongshore gradient of the free surface elevation. The nonlinear terms associated with the alongshore momentum flux and bottom shear stress are shown to be negligible outside the surf zone and reduce the low-frequency components of the alongshore velocity in the breaker and inner surf zones. On the other hand, the alongshore free surface gradient is found to be negligible in driving the alongshore oscillatory fluid motion in the swash zone except for the very low-frequency range. The very slow oscillations of the computed alongshore velocity in the vicinity of the breaker zone are inferred to be caused by the very low-frequency component of the alongshore free surface gradient whose origin is uncertain and can be numerical.

Finally, the 3D model is also compared with the DELILAH field data for a barred beach (Smith *et al.* 1993). The frequency and directional spectra were measured at the 8 m depth. The seaward boundary of the numerical model, based on the assumption of shallow water waves, is taken at the 3.64 m depth. The shoaling and refraction of linear directional random waves is computed to estimate the frequency spectrum and dominant wave direction at the seaward boundary. The 3D model underpredicts the root-mean-square wave height somewhat in the bar trough region and predicts a peak in the longshore current at the seaward

edge of the bar crest. Under the assumption of alongshore uniformity, the model cannot explain the observed broad peak in the longshore current in the bar trough region. Small alongshore variations of the incident wave intensity and resulting wave setup are shown to modify the longshore current profile in the bar trough region significantly. The cross-shore gradient of the alongshore radiation stress driving the longshore current is very small in this bar trough region. The alongshore gradient of wave setup is shown to alter the force driving the longshore current significantly in this region and produces a broad peak in the longshore current. Contrary to the computed results for the barred beach, the longshore current profile on planar beaches is found to be insensitive to the alongshore variations of the incident wave intensity and resulting wave setup. As a result, the prediction of the longshore current profiles on barred beaches will require the knowledge of small alongshore variability that is very difficult to measure accurately.

REFERENCES

Anderson, D.A., Tannehill, J.C., and Pletcher, R.H., 1984. *Computational Fluid Mechanics and Heat Transfer.* Hemisphere, New York.

Battjes, J.A., 1974. "Surf similarity." *Proc. 14th Coastal Engineering Conference*, ASCE, **1**, 466–480.

Battjes, J.A., 1988. "Surf-zone dynamics." *Annual Review of Fluid Mechanics*, **20**, 257–293.

Bodge, K.R., and Dean, R.G., 1987. "Short-term impoundment of longshore transport." *Proc. Coastal Sediment'87*, ASCE, **1**, 468–483.

Bouws, E., Günther, H., Rosenthal, W., and Vincent, C.L., 1985. "Similarity of the wind wave spectrum in finite depth water, 1. Spectral Form. " *J. Geophysical Research*, **90**(C1), 975–986.

Bowen, A.J., and Guza, R.T., 1978. "Edge waves and surf beat." *J. Geophysical Research*, **83**(C4), 1913–1920.

Bowen, A.J., and Holman, R.A., 1989. "Shear instabilities of the mean longshore current, 1, Theory." *J. Geophysical Research*, **94**(C12), 18023–18030.

Bowen, A.J., and Inman, D.L., and Simmons, V.P., 1968. "Wave set-down and set-up." *J. Geophysical Research*, **73**(8), 2569–2577.

Brocchini, M., and Peregrine, D.H., 1996. "Integral flow proprties of the swash zone and averaging." *J. Fluid Mechanics*, **317**, 241–273.

Carrier, G.F., and Greenspan, H.P., 1958. "Water waves of finite amplitude on a sloping beach." *J. Fluid Mechanics*, **4**, 97–109.

Chaudhry, M.H., 1993. *Open-channel flow.* Prentice Hall, Englewood Cliffs, New Jersey.

Church, J.C., and Thornton, E.B., 1993. "Effects of breaking wave induced turbulence within a longshore current model." *Coastal Engineering*, **20**, 1–28.

Cox, D.T., Kobayashi, N., and Kriebel, D.L., 1994. "Numerical model verification using SUPERTANK data in surf and swash zone." *Proc. Coastal Dynamics'94*, ASCE, 248-262.

Cox, D.T., Kobayashi, N., and Okayasu, A., 1994. "Vertical variations of fluid velocities and shear stress in surf zones." *Proc. 23rd Coastal Engineering Conference*, ASCE, 98–112.

Cox, D.T., Kobayashi, N., and Okayasu, A., 1996. "Bottom shear stress in the surf zone." *J. Geophysical Research*, **101**(C6), 14337–14348.

Dalrymple, R.A., "Rip currents and their causes." *Proc. 16th Coastal Engineering Conference*, ASCE, 1414–1427.

Dean, R.G., and Dalrymple, R.A., 1984. *Water Wave Mechanics for Engineers and Scientists.* Prentice-Hall, Inc., Englewood Cliffs, New Jersey.

Elgar, S., and Guza, R.T., 1986. "Nonlinear model predictions of bispectra of shoaling gravity waves." *J. Fluid Mechanics*, **167**, 1-18.

Fennema, R.J., and Chaudhry, M.H., 1986. "Explicit numerical schemes for unsteady free-surface flows with shocks." *Water Resources Research*, **22**(13), 1923–1930.

Gharangik, A.M., and Chaudhry, M.H., 1991. "Numerical simulation of hydraulic jump." *J. Hydraulic Engineering*, ASCE, **117**(9), 1195–1211.

Goda, Y., 1985. *Random Seas and Design of Maritime Structures.* University of Tokyo Press, Tokyo, Japan.

Gourlay. M.R., 1976. "Non-uniform alongshore currents." *Proc. 15th Coastal Engineering Conference*, ASCE, 701–720.

Greenberg, M.D., 1988. *Advanced Engineering Mathematics.* Prentice Hall, Englewood Cliffs, New Jersey.

Guza, R.T., and Thornton, E.B., 1982. "Swash oscillations on a natural beach." *J. Geophysical Research*, **87**(C1), 483–491.

Guza, R.T., and Thornton, E.B., 1985. "Velocity moments in nearshore." *J. Waterway, Port, Coastal and Ocean Engineering*, ASCE, **111**(2), 235–256.

Haines, J.W., and Sallenger, Jr., A.H., 1994. "Vertical structure of mean cross-shore currents across a barred surf zone." *J. Geophysical Research*, **99**(C7), 14223–14242.

Holman, R.A., and Bowen, A.J., 1982. "Bars, bumps, and holes: Models for the generation of complex beach topography." *J. Geophysical Research*, **87**(C1), 457–468.

Holman, R.A., and Sallenger, Jr., A.H., 1985. "Setup and swash on a natural beach." *J. Geophysical Research*, **90**(C1), 945–953.

Huntley, D.A., Guza, R.T., and Thornton, E.B., 1981. "Field observations of surf beat, 1, Progressive edge waves." *J. Geophysical Research*, **86**(C7), 6451–6466.

Jameson, A., Schmidt, W., and Turkel, E., 1981. "Numerical solutions of the Euler equations by finite volume methods using Runge-Kutta time-stepping schemes." *Proc. AIAA 14th Fluid and Plasma Dynamics Conference*, American Institute of Aeronautics and Astronautics, 81–1259.

Johnson, B.D., Kobayashi, N., and Cox, D.T., 1996. "Formulation and validation of vertically two-dimensional shallow-water wave model." *Research Report No. CACR-96-05*, Center for Applied Coastal Research, University of Delaware, Newark, Delaware.

Jonsson, I.G., and Carlsen, N.A., 1976. "Experimental and theoretical investigations in an oscillatory turbulent boundary layer." *J. Hydraulics Research*, **14**, 45–60.

Kamphuis, J.W., 1991. "Alongshore sediment transport rate." *J. Waterway, Port, Coastal and Ocean Engineering*, ASCE, **117**(6), 624–640.

Karjadi, E.A., and Kobayashi, N., 1994. "Numerical modeling of solitary wave breaking, runup and reflection." *International Symposium on Waves - Physical and Numerical Modeling*, IAHR, **1**, 426–435.

Karjadi, E.A., and Kobayashi, N., 1996. "Time-dependent quasi-3D modeling of breaking waves on beaches." *Proc. 25th Coastal Engineering Conference*, ASCE (in press).

Keeley, J.R., and Bowen, A.J., 1977. "Longshore variations in the longshore current." *Canadian J. Earth Science*, **14**, 1897–1905.

Kobayashi, N., DeSilva, G.S., and Watson, K.D., 1989. "Wave transformation and swash oscillation on gentle and steep slopes." *J. Geophysical Research*, **94**(C1), 951–966.

Kobayashi, N., Herrman, M.N., Johnson, B.D., and Orzech, M.D., 1997. "Probability distribution of surface elevation in surf and swash zones." *J. Waterway, Port, Coastal and Ocean Engineering*, ASCE (submitted).

Kobayashi, N., and Johnson, B.D., 1995. "Numerical model VBREAK for vertically two-dimensional breaking waves on impermeable slopes." *Research Report No. CACR-95-06*, Center for Applied Coastal Research, University of Delaware, Newark, Delaware.

Kobayashi, N., and Karjadi, E.A., 1994a. "Surf-similarity parameter for breaking solitary-wave runup." *J. Waterway, Port, Coastal and Ocean Engineering*, ASCE, **120** (6), 645–650.

Kobayashi, N., and Karjadi, E.A., 1994b. "Swash dynamics under obliquely incident waves." *Proc. 24th Coastal Engineering Conference*, ASCE, 2155–2169.

Kobayashi, N., and Karjadi, E.A., 1996. "Obliquely incident irregular waves in surf and swash zones." *J. Geophysical Research*, **101**(C3), 6527–6542.

Kobayashi, N., and Karjadi, E.A., Johnson, B.D., 1997. "Dispersion effects on longshore current in surf zones." *J. Waterway, Port, Coastal and Ocean Engineering*, ASCE (in press).

Kobayashi, N., Otta, A.K., and Roy, I., 1987. "Wave reflection and run-up on rough slopes." *J. Waterway, Port, Coastal and Ocean Engineering*, ASCE, **113**(3), 282–298.

Kobayashi, N., and Raichle, A.W., 1994. "Irregular wave overtopping of revetments in surf zones." *J. Waterway, Port, Coastal and Ocean Engineering*, ASCE, **120**(1), 56–73.

Kobayashi, N., and Wurjanto, A., 1992. "Irregular wave setup and run-up on beaches." *J. Waterway, Port, Coastal and Ocean Engineering*, ASCE, **118**(4), 368–386.

Kuriyama, Y., 1994. "Numerical model for longshore current distribution on a bar-trough beach." *Proc. 24th Coastal Engineering Conference*, ASCE, 2237–2251.

Larson, M., and Kraus, N., 1991. "Numerical model of longshore current for bar and trough beaches." *J. Waterway, Port, Coastal and Ocean Engineering*, ASCE, **117**(4), 326–347.

LeMéhauté, B., and Wang, J.D., 1982. "Wave spectrum changes on a sloped beach." *J. Waterway, Port, Coastal and Ocean Engineering*, ASCE, **108**(1), 33–47.

Longuet-Higgins, M.S., 1970. "Longshore currents generated by obliquely incident sea waves, 1 and 2." *J. Geophysical Research*, **75**(C3), 6778–6801.

Longuet-Higgins, M.S., and Stewart, R.W., 1960. "Changes in the form of short gravity waves on long waves and tidal currents" *J. Fluid Mechanics*, **13**, 481–504.

MacCormack, R.W., 1969. "The effects of viscosity in hypervelocity impact cratering." *Paper 69-354*, American Institute of Aeronautics and Astronautics, New York.

Nairn, R.B., Roelvink, J.A., Southgate, H.N., 1990. "Transition zone width and implications for modelling surf zone hydrodynamics." *Proc. 22th Coastal Engineering Conference*, ASCE, **1**, 68–81.

Oltman-Shay, J., Howd, P.A., Birkemeier, W.A., 1989. "Shear instabilities of the mean longshore current, 2, Field observations." *J. Geophysical Research*, **94**(C12), 18031–18042.

Packwood, A.R., 1980. "Surf and run-up on beaches." *Ph.D. Dissertation*, School of Mathematics, University of Bristol, United Kingdom.

Poff, M.T., and Kobayashi, N., 1993. "Computer program for refraction of directional random waves." *Research Report No. CACR-93-04*, Center for Applied Coastal Research, University of Delaware, Newark, Delaware.

Putrevu, U., Oltman-Shay, J., and Svendsen, I.A., 1995. "Effect of alongshore nonuniformities on longshore current predictions." *J. Geophysical Research*, **100**(C8), 16119–16130.

Raubenheimer, B., Guza, R.T., Elgar, S., and Kobayashi, N., 1995. "Swash on a gently sloping beach." *J. Geophysical Research*, **100**(C5), 8751–8760.

Richtmyer, R.D., and Morton, K.W., 1967. *Difference Methods for Initial-Value Problems.* Wiley-Interscience, New York.

Rodi, W., 1980. *Turbulence Models and Their Application in Hydraulics.* International Association of Hydraulic Research, Delft, the Netherlands.

Ryrie, S.C., 1983. "Longshore motion generated on beaches by obliquely incident bores." *J. Fluid Mechanics*, **129**, 193–212.

Schäffer, H.A., Deigaard, R., and Madsen, P., 1992. "A two-dimensional surf zone model based on the Boussinesq equations." *Proc. 23rd Coastal Engineering Conference*, ASCE, **1**, 576–589.

Smith, J.M., Larson, M., and Kraus, N.C., 1993. "Longshore current on a barred beach: Field measurements and calculations." *J. Geophysical Research*, **98**(C12), 22717–22731.

Svendsen, I.A., and Madsen, P.A., 1984. "A turbulent bore on a beach." *J. Fluid Mechanics*, **148**, 73–96.

Svendsen, I.A., and Putrevu, U., 1994. "Nearshore mixing and dispersion" *Proc. Royal Society of London*, A(445), 561–576.

Symonds, G., and Huntley, D.A., 1980. "Waves and currents over nearshore bar systems." *Proc. Canadian Coastal Conference*, 64–78.

Thornton, E.B., and Abdelrahman, S., 1991. "Sediment transport in the swash due to obliquely incident wind-waves modulated by infragravity waves." *Proc. Coastal Sediments'91*, ASCE, **1**, 100–113.

Thornton, E.B., and Guza, R.T., 1982. "Energy saturation and phase speeds measured on a natural beach." *J. Geophysical Research*, **87**(C12), 9499–9508.

Thornton, E.B., and Guza, R.T., 1983. "Transformation of wave height distribution." *J. Geophysical Research*, **88**(C10), 5925–5938.

Thornton, E.B., and Guza, R.T., 1986. "Surf zone longshore currents and random waves: field data and models." *J. Physical Oceanography*, **16**, 1165–1178.

Thornton, E.B., and Guza, R.T., 1989. "Models for surfzone dynamics." *Nearshore Sediment Transport*, edited by R.J. Seymour, 337–369, Plenum, New York.

Visser, P.J., 1984. "Uniform longshore current measurements and calculations." *Proc. 19th Coastal Engineering Conference*, ASCE, **2**, 2192–2207.

Visser, P.J., 1991. "Laboratory measurements of uniform longshore currents." *Coastal Engineering*, **15**, 563–593.

Wu, C-S., Thornton, E.B., and Guza, R.T., 1985. "Waves and longshore currents: comparison of a numerical model with field data." *J. Geophysical Research*, **90**(C3), 4951–4958.

Zelt, J.A., 1991. "The run-up of nonbreaking and breaking solitary waves." *J. Coastal Engineering*, **15**, 205–246.